Mapping Epithermal alteration mineralogy with high spatial resolution hyperspectral imaging of rock samples.

ISABEL CECILIA CONTRERAS ACOSTA
FEBRUARY, 2017

SUPERVISORS:
Dr. Chris Hecker
Dr. Freek van der Meer

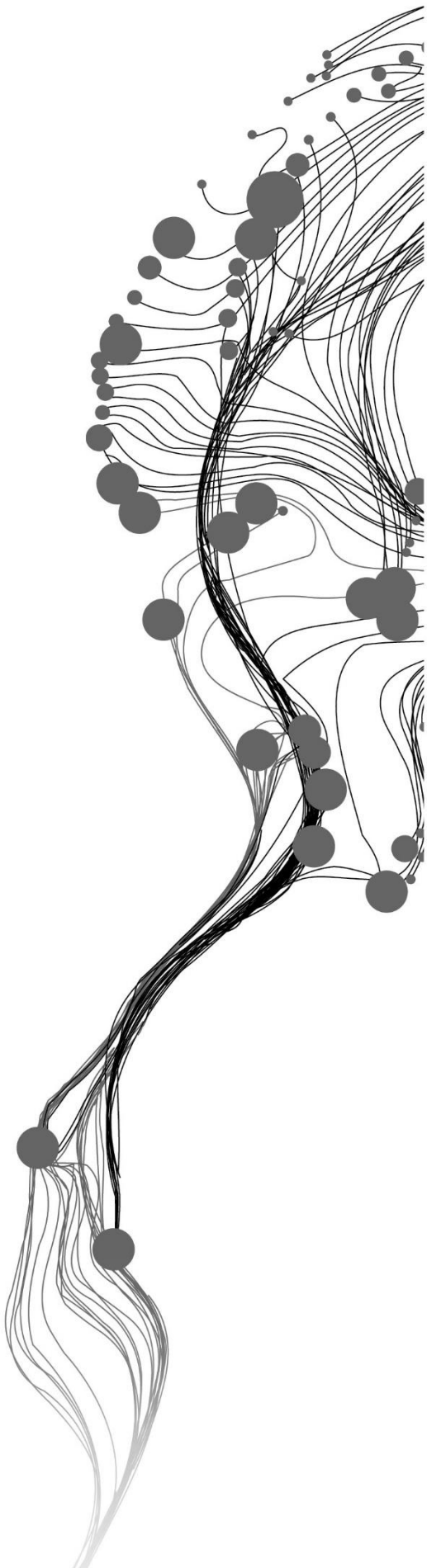

Mapping Epithermal alteration mineralogy with high spatial resolution hyperspectral imaging of rock samples.

ISABEL CECILIA CONTRERAS ACOSTA
Enschede, The Netherlands, February, 2017

Thesis submitted to the Faculty of Geo-Information Science and Earth Observation of the University of Twente in partial fulfilment of the requirements for the degree of Master of Science in Geo-Information Science and Earth Observation.
Specialization: Applied Earth Sciences in Natural Hazards, Risk and Engineering.

SUPERVISORS:
Dr. Chris Hecker
Dr. Freek van der Meer

THESIS ASSESSMENT BOARD:
Dr. M. van der Meijde (Chair)
Dr. M.Schodlok (External Examiner, Hannover)

ABSTRACT

Classifications of alterations zones have been done qualitatively, based on the minerals that exist or not in the alteration system. This results in a problem since minerals such as alunite and kaolinite can be formed by either hypogene or supergene processes. Thus, accumulations of these hypogene and supergene minerals cause overprinting patterns that overlay each other in the alteration system. For mineral exploration purposes, these two groups should be mapped separate from each other, if hypogene accumulations are prospective for important ore accumulations and supergene are not. In this way differentiation and quantification of hypogene and supergene minerals is needed. This research uses the high-sulfidation epithermal system in the Rodalquilar Caldera Complex where hypogene alteration is associated with gold accumulations, and supergene overprinting patterns occur. A total of 22 images of 20 rock samples were acquired with a high spatial resolution, hyperspectral SWIR camera, allowing not only to quantify mineral concentrations in a more representative way but also to evaluate the spatial distribution of the minerals in the samples. After the images were pre-processed for calibration issues, the Wavelength Mapping algorithm was used for the selection of the endmembers. Once the endmembers were collected, the determination of the spectral and chemical differences of the alunite and the degree of crystallinity in the kaolinites was done. As a validation of the alunite study, Inductively Coupled Plasma/Optical Emission Spectrometry and Thermogravimetric analyses were carried out. Then, the processes of formation, either by hypogene or supergene processes, of the endmember minerals were determined from literature. Subsequently, the Spectral Angle Mapper (SAM) was used to classify and quantify the images based on the most dominant mineral per pixel. In the same way, the Iterative Spectral Mixture Analysis (ISMA) algorithm was used to unmix the spectra to obtain the pixel fraction abundance. This lead to a more realistic quantification of the concentration of the minerals. Finally, the quantification of the aggregated partial fractions of the minerals per pixel was done to classify the rock samples. Spectral differences were found in alunites from the Rodalquilar. For the hypogene and supergene alunite, chemical differences were encountered in the composition and structure between the two minerals. Based on geochemical analysis concentrations of Y and Sr are high, while in supergene alunite are low. K rich alunite is confirmed to have the 1480 feature at short wavelengths. Mineral abundances per sample of normalized ISMA results are presented in radial plots.

ACKNOWLEDGEMENTS

This research would not have been possible without my supervisors Chris Hecker and Freek van der Meer. I would like to thank them for their guidance, support, and encouragement in every moment. Thanks to Chris for his advice, and Freek for his challenges.

Many thanks to Boudewijn de Smeth for coming out of retirement to help locate the samples.

I am grateful to Harald van der Werff for his help in the earlier stages of the research and acquiring the data. Thanks to Wim Bakker for his contribution with HyPpy codes.

I am also very grateful with Caroline Lievens for her assistance with the TGA and ICP-OES analyses and for her collaboration with the interpretation.

My gratitude is also to the UTS/ITC scholarship for making my studies possible. Also to the staff members of Applied Earth Sciences for their support since the beginning, especially to Bart Krol and Frank van Ruitenbeek for their contributions.

Finally, my greatest thanks to God and my family: mommy, daddy, Hector, Carla, Fiore, Jaime, Enrique, and Miguel, for keeping me on track, loving me and being with me always. Nothing would have been possible without you.

TABLE OF CONTENTS

LIST OF FIGURES

LIST OF TABLES

LIST OF APPENDICES

LIST OF ABBREVIATIONS

ASD	Analytical Spectral Devices
DTG	Derivative thermogravimetric
EM	Endmember
ICP-OES	Inductively Coupled Plasma Optical Emission Spectroscopy
ISMA	Iterative implementation of Spectral Mixture Analysis
nm	nanometres
PIMA	Portable Infrared Mineral Analyser
SAM	Spectral Angle Mapper
SWIR	Short Wave Infrared
TGA	Thermogravimetric analysis or Thermal Gravimetric Analysis
TSA	The Spectral Assistant
TSG	The Spectral Geologist
XRD	X-ray diffraction

1. INTRODUCTION

1.1. Problem definition

Formation of minerals in alteration systems develop patterns that overlay each other. These aggregations can be either from hypogene minerals which are primary alteration minerals that occur below the earth's surface from aqueous solutions; or from supergene minerals. Supergene minerals, or secondary minerals, occur at low temperatures near the surface by oxidizing meteoric waters (Rakovan, 2003). Since hypogene alteration minerals are associated with prospective gold accumulations of interest to the industry, classifying these alterations is an important task.

Classifications of these mineral aggregations are made into alterations zones, such as a vuggy silica, advanced argillic, intermediate argillic, amongst others. These classifications have been previously done qualitatively, by looking at the presence or absence of characteristic minerals. Thus, a list of minerals in order of abundances, or general descriptive terms, name, describe and classify these alteration zones (Hedenquist, Arribas R, & Gonzalez-Urien, 2000; Pirajno, 2015; Rosenberg, Bignall, & Rae, 2009). Some of these indicator minerals, such as alunite or kaolinite, can be the result of either hypogene or supergene processes that overlay each other. Hence, the discrimination between the prospective (hypogene) accumulations and the supergene accumulations can be confusing. Consequently, a distinction and quantification of hypogene and supergene minerals must be done.

Differentiation between the hypogene and the supergene versions of minerals is possible in different ways, either by looking at the composition or structural order. In the case of alunite minerals, small differences in mineral chemistry (composition) between the hypogene and supergene minerals exist. (Arribas et al., 1995; Ercan, Ece, Schroeder, & Karacik, 2016). For kaolinite minerals, a differentiation is possible based on crystallinity characteristics (structural order), which is a proxy for relative temperature conditions of formation of the minerals (Dill, Bosse, Henning, Fricke, & Ahrendt, 1997; Garcia, 2013). Besides, hypogene mineral associations are different from the supergene assemblages, and the spatial patterns that both create may also be different.

Mineral alteration patterns have been widely studied using petrographic and geochemical techniques, as well as laboratory, ground and airborne infrared spectroscopy (Bedini, van der Meer, & van Ruitenbeek, 2009; Cruz, 1989; Fagbohun, 2015; Yang, Huntington, Boardman, & Mason, 1999). The present research, however, will use high spatial resolution hyperspectral shortwave infrared (SWIR) images on rock samples. These datasets provide high spatial resolution images to recognize spectra of individual minerals present in rock samples than is the case in spectra of point measurements of e.g. ASD spectra. Hence, the minerals' compositional and crystallinity characteristics will be better determined. Consequently, differentiations between hypogene and supergene minerals will be targeted, and, based on the hypogene minerals, a quantitative classification of the alteration zones, in which the rock samples were formed, will be established.

This research uses data from the Rodalquilar caldera complex in south-eastern Spain. It is a high-sulfidation epithermal Au deposit which contains mineral patterns of hypogene alterations with supergene overprint, where the hypogene minerals are associated with accumulations of gold. The system and the alteration zones have been qualitatively proposed and mapped (Arribas et al., 1995) and the presence of supergene and hypogene alunite and kaolinite are known. Crystallinity studies in the Rodalquilar system have been done

for the smectite-illite and kaolin group which are indicators of the degree of alteration (Garcia, 2013). However, the quantification of these alteration minerals and the spectral behavior of the supergene and hypogene varieties of alunite is not known yet.

1.2. Research objectives

Main objectives

To quantitatively study hypogene mineral assemblages to classify the alteration zones of an epithermal alteration system by using high spatial resolution hyperspectral images on rock samples.

Specific objectives

1. To characterize the spectral and chemical differences between the hypogene and supergene alunite.
2. To spectrally estimate the crystallinity variations in kaolinites.
3. To evaluate overprinting relations by looking at the spatial distribution of the minerals.
4. To quantify the hypogene minerals in rock samples.
5. To classify the alteration zones in the rock samples based on mineral quantities and temperature conditions.

1.3. Research questions

1. What are the spectral and chemical differences between the hypogene and supergene versions of the alunite? Which minerals are spatially associated with each of the alunites?
2. Which kaolinites can be spectrally recognized based on their differences in crystallinity? Are these kaolinites the product of weathering or hydrothermal processes?
3. What is the spatial relation between the minerals that are overprinting each other? How can these overprinting relations help with the classification of the alteration zones?
4. In overall, which of the recognized minerals are hypogene and which ones are supergene? What is the concentration for each of them in the rock samples?
5. In which alteration zones are the rock samples formed based on the mineral quantities and the relative temperature conditions of formation?

1.4. Hypotheses

- The minerals that are expected to be found are those typical for alterations in a high sulfidation epithermal system. These are alunite, minerals from the kaolin group, sericite, illite, diaspore, hydrothermal quartz, pyrite, amongst others.
- Changes in the spectral absorption features around 1400nm and 2160nm – 2180nm will allow the differentiation amongst hypogene and supergene alunites, and kaolinites with differences in crystallinity, respectively.

1.5. Thesis structure

The thesis has been organized into six chapters. **Chapter 1**, Introduction, defines the research problem leading to the research objectives, research questions, and hypotheses. **Chapter 2**, Research Background, puts the research in context explaining the study area selected and the spectroscopy knowledge needed for the execution of the research. **Chapter 3**, Methods and data, explains the methodology followed to carry out the research, from the selection of the samples, followed to the pre-processing techniques and algorithms used for the image analysis, to the quantification of the samples. **Chapter 4**, Results, presents the results of all the steps followed. **Chapter 5**, Discussion, discusses the result and development of the methodology. Finally, **chapter 7** presents the conclusions and recommendations.

2. RESEARCH BACKGROUND

Before starting with the description of the research, different topics must be considered. Firstly, it is presented the study area, the alteration system and the mineralization patterns that are developed in there. Followed by a summary of the SWIR mineral spectroscopy in the system and its most important characteristics.

2.1. Rodalquilar caldera complex

2.1.1. Location and geological structure

The Rodalquilar epithermal Au alunite deposit occurs within the Rodalquilar caldera complex in the Miocene Cabo de Gata volcanic field, Betics mountain range, Almeria Province, south-eastern of Spain. The complex is composed of two nested calderas, The outer Rodalquilar caldera, and the inner Lomilla caldera. They are located 8 Km towards the north of the older Los Frailes caldera (see Figure 1(B))((Rytuba et al., 1990).

The Rodalquilar caldera is an oval collapse structure. It has a maximum diameter of 8 km in an east-west direction and a minimum diameter of 4 km in a north-south direction. It is characterized by an extensive east-west-trending zone of hydrothermally altered rocks (25 km^2) (Arribas et al., 1995). The northern structural margin of the caldera is defined by a single, nearly vertical fault that is perfectly defined for 2 km. The south wall of the caldera is well preserved and is defined for a strike of about 5 km (see figure 1(A)) (Rytuba et al., 1990).

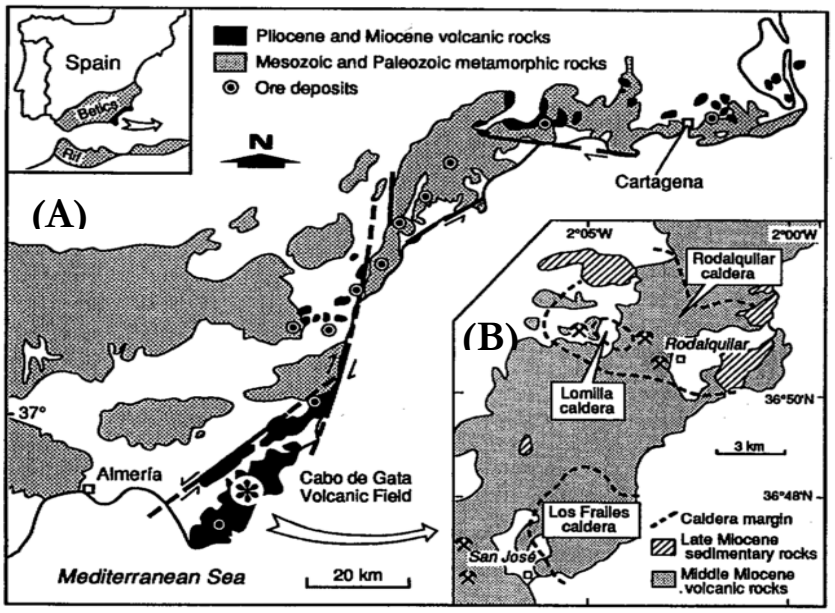

Figure 1. (A) Location of the Rodalquilar Au deposit, Cabo de Gata volcanic field, south-eastern Spain. (B) The Central part of the Cabo de Gata volcanic field showing the location of the calderas (Arribas et al., 1995).

The formation of the caldera started around 11.2 Ma with an eruption of the rhyolitic Cinto ash-flow tuff. This resulted in the emplacement of larger ring domes, the Lazaras ash-flow tuff eruption and the development of the Lomilla caldera. Later, the emplacement of hornblende andesitic intrusions at shallow depths contributes to the early stage of hypogene acidic alteration. Following this, a hydrothermal system

was developed spatially related with the previous emplacement of the intrusions. It was at around 10.4 Ma and resulted in a high-sulfidation hypogene mineralization deposit. Finally, around 3 and 4 Ma, a supergene acid sulfate alteration occurred due to the exposure of the ore to weathering. The hypogene and supergene deposits are overlapping each other (Arribas et al., 1995; Lopez-Ruiz & Rodriguez-Badiola, 1980).

2.1.2. Rodalquilar epithermal system and mineralization

Epithermal systems are a particular type of hydrothermal systems developed at shallow depths, around 1 – 2 Km below the Earth's surface with temperatures that varies between 50 - 200 ºC (Segalst, 1997). Pods and lenses of massive sulfide replacement, crosscutting veins, stockworks, and breccias are common (Panteleyev, 2005). Deposits in epithermal systems are controlled by permeability, temperature, pressure, the geometry of the host rock and nature of circulation fluids. Although it is known that epithermal systems are created by meteoric water fluids (Corbett, 2012), scientists believe that epithermal deposits might be affected by magmatic activity as well (Morishita & Nakano, 2008). Depending on the acidity of the hydrothermal fluid epithermal deposits are classified into two different systems, high-sulfidation and low-sulfidation deposits (Gonzalez P, 2009). The mineralization in these deposits varies depending on the sulfide composition which is affected by the redox conditions of the hydrothermal fluid and the reactivity (pH) (White & Hedenquist, 1995).

Mineralizations in the Rodalquilar caldera complex consists of high-sulfidation Au-(Cu-Te-Sn) ores and low-sulfidation Pb-Zn-(Cu-Ag-Au) quartz veins (Arribas et al., 1995). However, high-sulfidation epithermal systems highly contribute to the gold production of the world (Morishita & Nakano, 2008). Hence, the high-sulfidation epithermal deposit in the Rodalquilar is economically more important than the low-sulfidation deposit due to the concentration of Au. The gold concentration in the Rodalquilar caldera is located in the north-south structures and caldera margin structures (Cunningam, Arribas Jr., Rytuba, & Arribas, 1990).

Depending on the chemical composition of the minerals, exsolution and decomposition at lower temperatures can alter the primary mineralization creating overprinted patterns of supergene minerals (Armstrong, 1995). Primary mineralization by circulating hydrothermal fluids are called hypogene alterations and they deposit minerals called hypogene minerals (Segalst, 1997). Examples of these are quartz, alunite, kaolinite, illite-smectite, feldspars, chlorite, hematite, pyrite, pyrophyllite, diaspore, amongst others (Arribas et al., 1995; Thompson & Thompson, 1996). Regarding secondary minerals or supergene minerals, they are the result oxidizing meteoric waters causing dissolution, transport, and re-deposition of new minerals stable in these new conditions. In other words, they are the result of weathering or low-temperature hydrothermal alterations (White & Hedenquist, 1995). Minerals such as cuprite, gypsum, jarosite, poorly crystalline kaolinite, alunite, halloysite amongst others, are examples of supergene minerals (Arribas et al., 1995; Rakovan, 2003).

It is considered that in high-sulfidation systems hypogene and supergene minerals are not only overlapping each other but also their mineralogies are similar (White & Hedenquist, 1995). However, differences between hypogene and supergene minerals can be seen in the crystallinity structure, the composition of the minerals and the distribution along the systems.

Alunite minerals in the Rodalquilar can be the result of either advanced argillic alterations or intense acid sulfates alterations. The difference between the two minerals lies in the composition (Wasserman, Rye, Bethke, & Arribas, 1992). Hypogene alunite has pinkish colours and tabular crystals. It intergrows with pyrite in clusters and with pyrite and zunyite in the matrix of breccias. In hypogene alunite, the Na/K ratio is characteristically high, up to 0.4 (Arribas et al., 1995). Supergene alunite appears as a white, fine-grained powder filling fractures and open spaces, with corroded sulfides. As opposed to hypogene alunite, supergene alunite is always K rich ($Na/K < 0.05$) and it is not related to pyrite, zunyite or diaspore. Moreover, based

on Arribas et. al. (1995), supergene alunites seem to have a major content of Y and lower content of Zr than hypogene alunites. These concentrations can be seen in Table 1, adapted from Arribas et. al. (1995).

Table 1. Chemical composition of Alunite from the Rodalquilar caldera based on Arribas et. al (1995).

	Hypogene			Supergene		
Sample No. (ppm)	**SRT133**	**87A237**	**88A06**	**87A97**	**87A373**	**87A380**
Na	0.28	0.07	0.26	0.04	0.04	0.03
K	0.68	0.95	0.75	0.92	0.95	0.95
Sr	1500	446	2150	48	176	1150
Fe	0.02	0	0.04	0.09	0.03	0.11
Y	<10	12	20	86	60	102
Zr	60	166	156	16	16	52
Na/K	0.41	0.07	0.34	0.04	0.04	0.04

Regarding the variations in crystallinity, kaolinite minerals in the Rodalquilar can be the result of hypogene or supergene processes. Crystallinity means the degree of structural order (Oluwadebi, 2015), in other words, the level of organization of the atoms in the crystal structure (Plancon, Giese, & Snyder, 1988). When kaolinite results from argillic alterations it is highly crystalline and this indicates a higher temperature range. In the case of weathering or weak hydrothermal processes, kaolinite crystallinity is poor and the temperature range of formation is also low (Garcia, 2013; Pontual, Merry, & Gamson, 1997b).

Besides crystallinity variations of kaolinite minerals, kaolin group minerals are also indicators of relative temperature conditions and formation processes: Dickite results from high-temperature hydrothermal alterations as well as nacrite and highly crystalline kaolinite, while poorly crystalline kaolinite and halloysite hydrated might be products of low-temperature hydrothermal alterations or supergene processes (Cruz, 1989; Garcia, 2013). Halloysite has been interpreted as a low-temperature polymorph of kaolinite and the polymorphs are distinguished by two interlayered H_2O molecules, which are present within the halloysite but not in the kaolinite (Kyne, Hollings, Jansen, & Cooke, 2013).

Concerning the mineralization distribution in high-sulfidation systems, the ore is found in the zone of most acidic alteration which is surrounded by less acidic conditions indicated by their respective mineral assemblages (White & Hedenquist, 1995). To illustrate, figure 2 shows that kaolinite and alunite are either overlying or overprinting ores in high sulfidation deposits (Pontual, Merry, & Gamson, 1997a).

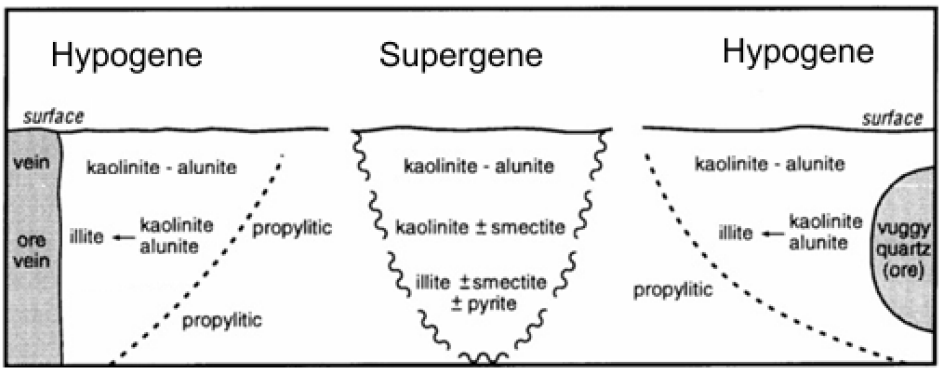

Figure 2. Hypogene and supergene alterations modified from White & Hedenquist (1995).

2.1.3. Alterations zones in the Rodalquilar

The formation of the alteration zones depends on different parameters such as temperature, pressure, fluid composition and initial composition of the rock. Even these factor are independent, the effect of one or more at the same time will result in a different type of alteration zone since different minerals are developed (Lagat, 2007). So far the study of the alteration zones has been done following different approaches. Researchers have focused they classification based on the most important minerals, the mineral assemblages or the chemical changes that produced the alteration (Gifkins, Herrman, & Large, 2005).

The hypogene alteration assemblages recognized in the Rodalquilar caldera are typical for a high-sulfidation deposit. The wall rock was altered by acidic hydrothermal fluids in the form of H_2SO_4 and HCL (Rytuba et al., 1990). These alteration zones are briefly described below starting from the most extreme leaching (Arribas et al., 1995):

Silicic zone characterized by the presence of vuggy residual silica and massive silicified rock within halos of advanced argillically altered rocks. Vuggy silica is more abundant and it is found in veins, hydrothermal breccias, and narrow fractures selvages. The main minerals are quartz with lesser amounts of rutile or anatase and Zircon as accessory mineral. Also, some alunite, kaolinite, zunyite and aluminum sulfate-phosphates are also presented. Hematite and jarosite are found as the result of the oxidation of primary pyrite which is the most abundant sulfide mineral. Elements that enrich this zone are As, Se, Sb, and Sr.

Advanced argillic zone is subdivided into two subzones. The first one content quartz + alunite ± kaolinite and is adjacent to the silicic zone. The second one starts gradually from the former one and consist of quartz + kaolinite, and illite. Illite-smectite are increasingly abundant. Other minerals such as dickite, pyrite, and pyrophyllite are also presented. The colours of the rocks are white to pink depending on the content of kaolinite or alunite. Main accessory minerals are diaspore, rutile or anatase, aluminum sulfate-phosphates, crandallite, florencite, zunyite. Chemically this zone is intermediate between the highly altered vuggy silica zone and the less intense argillic and propylitic zones as can be seen in Figure 3.

Intermediate argillic zone consists of quartz, kaolinite, illite, illite-smectite, K feldspar, hematite, goethite, pyrite and minor alunite, pyrophyllite, and diaspore. There are supergene overprinted zones. The chemical composition of the intermediate argillically altered rocks varies depending on the proximity to the rest of the zones. Closer to the advanced argillic zone kaolinite is more abundant and alunite is less. Closer to the propylitic halo illite-smectite is dominant, kaolinite is less and chlorite is rare. Finally, closer to the sericitic zone, illite and kaolinite are dominant and pyrite is less.

Sericitic zone is characterized by illite, quartz, and pyrite with less amount of rutile. Kaolinite, diaspore, and alunite are rare. Chlorite is sparse in the upper part of the zone, but it increases with depth. K mica with quartz and pyrite fill veins. Depletion of CaO, MgO, and Na_2O are characteristics. This zone is in fill tuffs at depths > 300 m (Figure 3).

Propylitic zone is argillically altered rocks that progressively grade to this zone. It consists of quartz, chlorite, K feldspar, vermiculite, illite, smectite, hematite, goethite, primary plagioclase and less calcite. The chemical composition of the rocks in this zone is almost unchanged compared with the unaltered rock.

Supergene acid sulfate alteration is characterized by supergene alunite. Thin cryptocrystalline veinlets of alunite overprint all previous hypogene altered zones. Supergene alunite is related to quartz, kaolinite, jarosite, hematite and hydrated amorphous silica. It occurs mainly superimposed or surrounding the core of

the advanced argillic alteration at shallow areas (figure 3). Minerals of unequivocal supergene origin are gypsum and jarosite (Kyne et al., 2013).

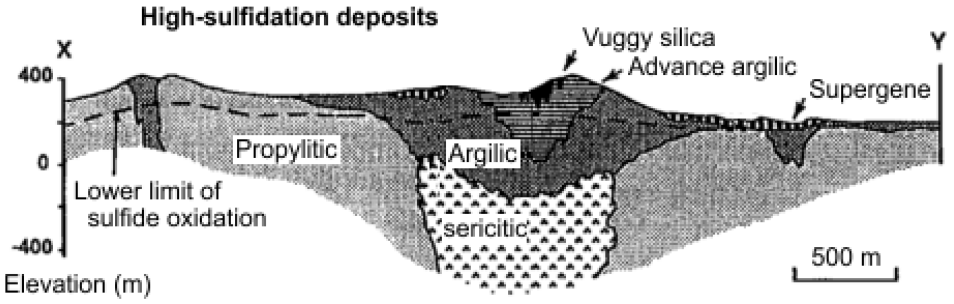

Figure 3. Cross section of the Rodalquilar caldera showing the distribution of the alteration zones.

2.2. SWIR mineral spectroscopy in epithermal systems

Minerals have characteristic spectral responses due to the bond between their atoms, as well as their electron orbitals (vibrational and electronic absorption processes). Absorption processes generate a spectral response in different parts of the spectrum, electronic processes in the visible-near infrared (VNIR) between 300 – 1000 nm and vibrational processes in the short-wave infrared (SWIR), between 1000 – 2500 nm. As a result, detailed surface composition characteristics (mineralogy, abundance, crystallinity amongst others) can be evaluated (G. L. Prost, 2013) with spectral data by looking at different positions and depth of the absorption features (van der Meer, 2004).

Identification of hydrothermal minerals, that include water and/or hydroxyl in their structures has been commonly done with SWIR (1000 – 2500 nm) spectral data (Calvin & Pace, 2016; Yang, Huntington, Browne, & Ma, 2000). They generate a response due to the vibrations of the cation O-H bonding. Important diagnostic features in this range are the ones near 1400 nm, due to hydroxyl (OH) and water, and at 1900 nm, due to water. Other diagnostic spectral absorption features related to the bending and stretching of the bonds between AlOH, FeOH and MgOH occur around 2200 nm, 2250 nm, and 2330 nm, respectively (Pontual, Merry, & Gamson, 1997d). In addition, spectral variations such as shifts in the wavelength position, and amplitude and narrowness of the absorption features show the sensibility of the SWIR range to changes in the chemical composition and crystallinity of hydrothermal minerals (Hunt & Ashley, 1979; Pontual et al., 1997d). All the parameters that define and describe SWIR active minerals have been described by Pontual et al. (1997d) as it is summarized below:

Kaolin group

It is formed by kaolinite *($Al_4[Si_4O_{10}](OH)_8$),* halloysite *($Al_4Si_4(OH)_8O_{10}{\cdot}8H_2O$),* dickite *($Al_4[Si_4O_{10}](OH)_8$)* and nacrite *($Al_4[Si_4O_{10}](OH)_8$).*

Absorptions are controlled by the hydroxyl bond near 1400 nm and 2200 nm. Changes in its vibration energy produce doublets in the spectral signature for the hydroxyl features. They are weaker in kaolinite and halloysite than in nacrite or dickite. The absorption features in halloysite are slightly shifted to shorter wavelengths and are slightly broader. They are around 1390-1410 nm and 2160-2207 nm, while in kaolinite they are around 1395-1415 nm and 2163-2209 nm (see Figure 4 (A)). Regarding dickite and nacrite, absorption features in the doublets of nacrite are closer to each other than in dickite (nacrite: 1386-1417 nm and 2179-2202 nm, dickite: 1384-1418 nm) (Pontual et al., 1997d). Molecular water presence in the structure of halloysite and poorly crystalline kaolinite is reflected on the 1900 nm feature. (Brindley, Kao, Harrison, Lipsicas, & Raythatha, 1986; Hauff, Kruse, & Thiry, 1990).

Variations in crystallinity for the kaolin group minerals are shown as variations in the shape of the diagnostic absorption features. The absorption near 1400 nm shifts to shorter wavelengths and becomes weaker when crystallinity decreases (Brindley et al., 1986). Similarly, the absorption feature around 2160 nm shifts to longer wavelengths and becomes weaker with decreasing crystallinity, being this absorption the most characteristic for the study of crystallinity variations in kaolinite minerals. (Pontual, Merry, & Gamson, 1997c). Moreover, the absorption feature at 1830 is present in highly crystalline kaolinites (Pontual et al., 1997d). As an illustration, Figure 4 (B) shows continuum removed spectra of kaolinite minerals with different crystallinities. At the top of the plot, highly crystalline kaolinites (HX) with the absorption feature at 2160 nm, then crystallinity degree starts decreasing and finally, at the bottom of the plot there is a poorly crystalline kaolinite (PX) with the absorption feature at 2180 nm.

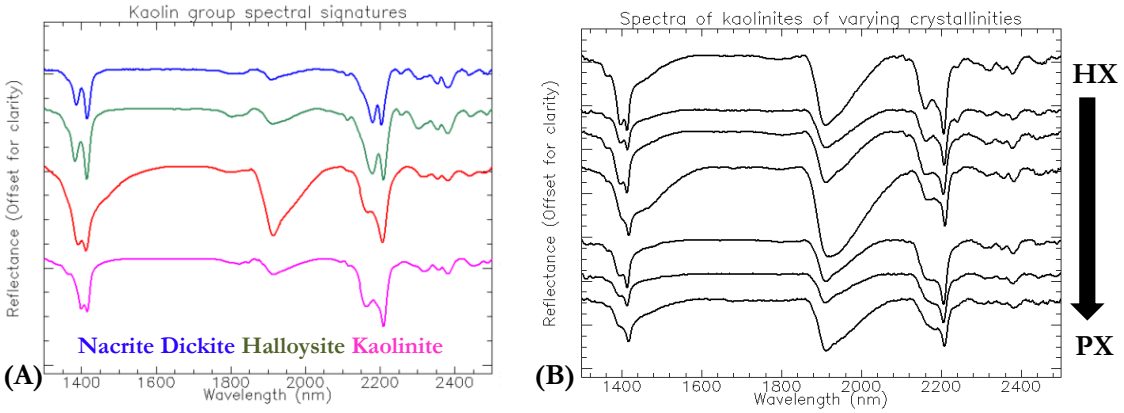

Figure 4. (A) Continuum-removed spectra of minerals from the kaolin group (Pontual et al., 1997d). (B). Continuum-removed spectra of kaolinites of varying crystallinity (Pontual et al., 1997c).

Pyrophyllite

$(Al_4[Si_8O_{20}](OH)_4)$

Diagnostic and single sharp absorption features of pyrophyllite in the SWIR are located at 1396 nm due to Oh and H_2O, and around 2166 nm due to AlOH. Less sharp absorptions that persist in mixtures are localized at 2066-2078 nm and around 2319 nm (see figure 5, red spectrum) (Pontual et al., 1997d). Moreover, content of H_2O is also showed in the 1945 nm absorption feature, as can be seen in figure 5, blue spectrum (Clark et al., 2007).

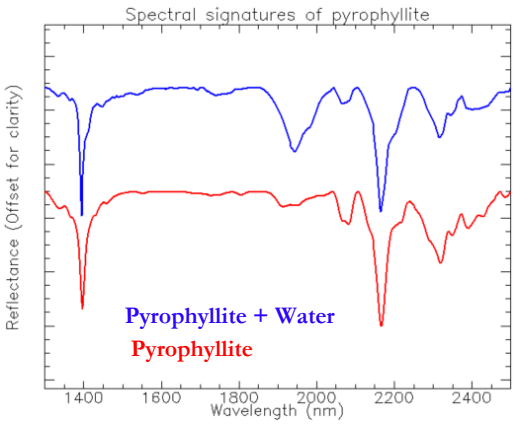

Figure 5. Continuum-removed spectra of pyrophyllite (Clark et al., 2007; Pontual et al., 1997d).

Illite-smectite groups

It is formed by illite/sericite $((Ca_{0.05}Na_{0.03}K_{0.061})(Al_{1.53}Fe^{+3}_{0.03}Mg_{0.28})(Si_{3.4}Al_{0.6})O_{10}(OH)_2)$, muscovite/sericite $(K_2AL_4[Si_6Al_2O_{20}](OH,F)_4)$ and montmorillonite $((1/2Ca,Na)_{0.7}(Al,Mg,Fe)_4[(Si,Al)_8O_{20}](OH)_4 \cdot nH_2O)$.

In this groups what is distinctive is the depth of the water absorption features, at 1400 nm and 1900 nm, indicative of the molecular water presents in the mineral structure. In this context, montmorillonite that has high content of water shows deeper and broader features than illite and muscovite. However, illite has an absorption feature at 1900 nm. Regarding the features related to the OH-cation, ion substitutions of Mg, Fe, and Al, modify these features. The deepest are around 2200 nm due to Al substitutions. For illite and muscovite, the sharp and diagnostic absorption feature is around 2180 - 2228 nm depending on the composition. On the contrary, montmorillonite has it broader than illite or muscovite, but not very deep. It is also shifting to longer wavelengths, around 2205-2212 nm. Finally, the doublet features related with Fe and Mg substitutions are located at 2347 nm and 2440 nm for illite and for muscovite are shifted to shorter wavelengths at 2342 nm and 2435 nm. This double is absent in montmorillonite (see figure 6) (Clark, King, Klejwa, Swayze, & Vergo, 1990; Hauff et al., 1990; Pontual et al., 1997d).

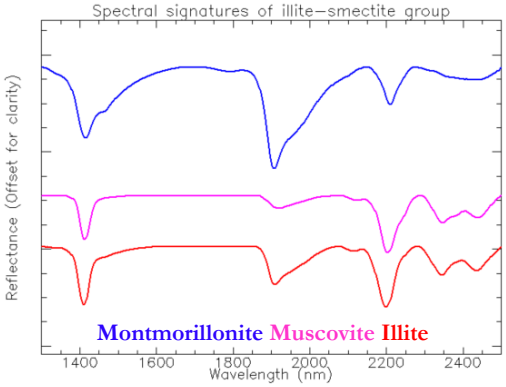

Figure 6. Continuum-removed spectra of the illite-smectite group (Pontual et al., 1997d).

Sulfate group

It is composed of alunite $((K, Na)\ Al_3\ (SO_4)_2 \cdot (OH)_6)$, gypsum $(CaSO_4 \cdot 2H_2O)$ and jarosite $(KFe_3\ (SO_4)_2\ (OH)_6)$.

It is common for all the sulfate minerals to have diagnostic absorption features around 1400 nm due to water and OH vibrations. However, the features are different for each of the minerals. For alunite a doublet at 1430-1440 nm and 1474-1490 nm, that varies with composition. At shorter wavelengths when it is K rich (see in Figure 7, magenta spectrum) and at longer wavelength when it is Na rich as can be seen in Figure 7, spectrum green. Regarding gypsum, it has a triplet at 1449 nm, 1490 nm, and 1535 nm and for jarosite two features at 1468 - 1477 nm and 1512 - 1544 nm. Another single feature characteristic for sulfates is related to OH and varies around 1750 nm and 1855 nm. For the rest of the spectrum in the SWIR, the absorption feature for sulfates varies depending on the mineral. For alunite, a broad feature is located around 2160 – 2170 nm and it has a small feature around 2200 nm. In addition, a single feature around 2324 nm that can be modified in mixtures with pyrophyllite, kaolinite, and dickite. These features are related with OH and AlOH. For jarosite, two features: a small one at 2206 nm and a feature that usually persist in mixtures at longer wavelengths (2262-2277 nm). They are related to the FeOH bond. Moreover, other jarosite spectra show an absorption feature around 1900 nm (see figure 7, maroon line) (Clark et al., 2007). In the case of gypsum, not diagnostic features are present at these wavelengths, only a small one at 2215 nm that may not persist in mixtures (Pontual et al., 1997d).

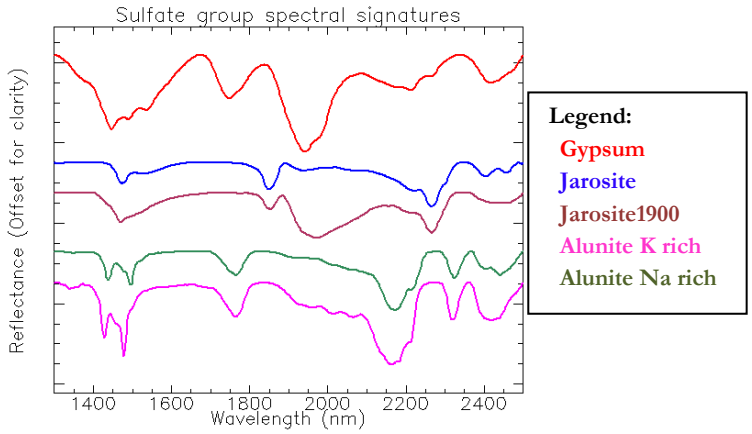

Figure 7. Continuum-removed spectra of sulfate group (Clark et al., 2007; Pontual et al., 1997d)

2.2.1. Previous spectral studies for mineral mapping

Mineralogical alterations, thus alteration facies or zones, have been widely studied using petrographic and geochemical techniques (Armstrong, 1995; Arribas et al., 1995) However, hyperspectral remote sensors such as airborne data (Bedini et al., 2009; Yang et al., 2000), spaceborne data has (Yang et al., 1999) and portable spectroradiometer (Calvin & Pace, 2016; Garcia, 2013; Prost, Dameme, Huard, Driard, & Leydecker, 1989) are also being used.

Regarding the study of hypogene and supergene minerals, not many studies have been done using spectral data. However, halloysite from a porphyry-epithermal deposit was evaluated to investigate if it can also be the result of hypogene processes since it has been always identified as a low-temperature polymorph of kaolinite and as an indicator of supergene processes in these environments. This was done with a TerraSpec spectrometer (Kyne et al., 2013).

3. METHODS AND DATA

For this research, non-imaging spectroscopy was used to select the most suitable samples. Then laboratory imaging spectroscopy with high spatial and spectral resolution was applied. The images were pre-processed and cleaned of data errors. After that, images were processed to visualize the main absorption wavelengths, to determine the spectral endmembers (for explanation see below) and to classify and unmix the images into the endmember fractions. The following sections will explain these steps in more detail.

3.1. Datasets

The data consists of 265 rock samples that have been collected by ITC Faculty members in different research campaigns in the Rodalquilar Caldera Complex in south-eastern Spain. From those samples, a spectral library of 217 samples is available from earlier research. They were measured by Garcia (2013) and Chororoka (2012) with the Analytical Spectral Device (ASD) FieldSpec spectrometer and the Portable Infrared Mineral Analyser (PIMA) II. Two or three measurements were taken for all the samples. In addition, as part of their research theses, X-ray Diffraction (XRD) analyses of 20 samples, as well as Thermal Gravimetric Analyses (TGA) of 11 samples were available. For this research, the existing ASD spectra of the 217 samples was used and extended with own ASD measurements of the 48 samples that had not been measured earlier.

3.2. Non-imaging spectroscopy

From the 48 samples that did not have spectral measurements yet, three measurements were taken to aim for the collection of the majority of the minerals present in the rock samples. During the measurements with the contact probe in the ASD FieldSpec spectrometer, the dark current and the white reference measurements were taken every two samples to ensure a reliable calibration of the equipment. An external Spectralon calibration standard was used as a white reference. After completion of the measurements, the raw data was initially processed using the ViewSpec software. A splice correction and a conversion of the ASD format into ASCII format were done with the intention of further use of the data in different software.

An initial mineralogical interpretation of the entire spectral library was done with The Spectral Assistant (TSA) in The Spectral Geologist (TSG) software to obtain a first idea of the mineral content of the rock samples. This is an algorithm built into the TSG that runs automatically and matches input spectrums against the most similar single mineral or mixture of two minerals spectrum, giving details of different parameters about the spectral signatures. The parameters considered for this research were the first and second most abundant minerals and the family group of the minerals which they are part of. This automatic interpretation was used to make a first pre-selection of samples containing alunite and/or kaolin group minerals (dickite, nacrite, kaolinite and halloysite), which were used for further processing. All the minerals from the kaolin group were considered to avoid the omission of data due to spectral similarities amongst the mineral members of the group.

3.3. Laboratory imaging spectroscopy

3.3.1. Sample selection

From the large sample set (217+48), a characteristic subset had to be selected to be used for the laboratory imaging. The goal was to included samples with variable alunite absorption wavelengths (as a proxy for composition) as well as different types of kaolin group members and kaolinite crystallinity. Firstly, for all ASD spectra with alunite and/or minerals from the kaolin group the interpolated depths, and interpolated wavelengths parameters were extracted. The extraction and evaluation of these parameters were done using

the Hyperspectral Python (HypPy) software using the Wavelength of Minimum algorithm. This algorithm determines the value of the wavelength for the deepest absorption feature. It was directly done for different wavelength ranges in the Math Expression on Spectrum S of the Spectral Library Viewer by using the equation 1, where *A* and *B* are the wavelength values of the selected wavelength interval (Bakker, 2012).

$$S[A:B].minwav(1) \quad (1)$$

It returns the interpolated wavelength position and interpolated depth of the deepest absorption feature in the specified wavelength range. This is calculated, as shown in figure 8, in a continuum removed spectra by fitting a parabola through three consecutive bands in the smallest local minimum, the band with the lowest reflectance (Van Ruitenbeek et al., 2014). The continuum removed spectra were calculated automatically by dividing the spectra by the hull quotient (Bakker, 2012).

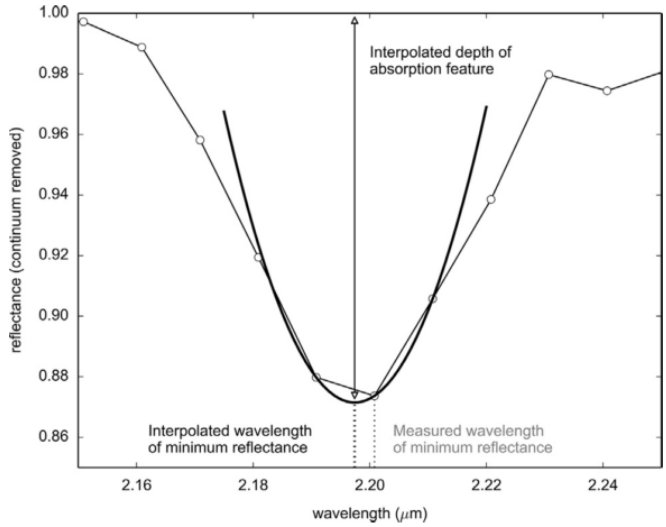

Figure 8. Interpolation method followed in the Wavelength of Minimum algorithm. A parabola is fitted through three consecutive measurements (Van Ruitenbeek et al., 2014).

The representation of the parameters extracted from the spectral libraries of alunite and kaolin group minerals were condensed into two scatter plots (see subchapter 4.2.1) representing interpolated depth versus interpolated wavelength since these two parameters show the wavelength position of the deepest point of the absorption features in the selected range. Hence, extreme characteristics of the minerals are visible. The samples that were selected for the research were chosen following different criteria explained below.

Alunite samples

The range used in the Wavelength of Minimum algorithm to extract the parameter was 1450 - 1550 nm, since differences in K and Na composition in alunite minerals are spectrally recognizable by the shift of the 1480 nm diagnostic absorption feature (Arribas et al., 1995; Clark et al., 2007; Pontual et al., 1997d).

Samples with extremely different characteristics were interesting. This means samples with deep absorption features at shorter and longer wavelength, being K rich alunites at shorter wavelengths and Na rich alunites at longer wavelengths, as can be seen in Figure 7. For the selection of the alunites samples, not only the position of the 1480 nm absorption feature in the plot (at short or long wavelengths) but also the content based on the TSA interpretation (e.g. alunite with pyrophyllite) were taken into account, as overlapping features can shift or deepen the diagnostic 1480 feature.

Kaolin group samples

Crystallinity variations in kaolinite minerals show changes in the absorption feature at 2160 - 2180 nm. The 2160 nm feature shifts to longer wavelengths and becomes weaker when crystallinity decrease (Pontual et al., 1997d). For that reason, the wavelength range used in the Wavelength of Minimum was 2100 – 2195nm.

In this group, the selection of the samples was focused mainly on the ones at shorter wavelengths with deep absorption features (highly crystalline) and at longer wavelengths with shallow absorption features (poorly crystalline) to select the samples with the most different crystallinity degrees. Moreover, samples with minerals from the rest of the kaolin group were also chosen to complement the research, since minerals such as dickite, nacrite, and halloysite dehydrated, which as highly crystalline kaolinite are indicators of hypogene processes and hydrated halloysite as poorly crystalline kaolinite are indicators of supergene processes.

3.3.2. Sample preparation

Once the samples to be used in the research were selected from the previous scatter plot. They needed to be prepared for the acquisition of the images, this was done in three steps. Firstly, the rocks were cut with a rock saw through the more heterogeneous areas to ensure the presence of different, unweathered minerals and to avoid shadows in the images due to irregular surfaces. The Lortone Slab Saw at the Geo-Science Laboratory of the ITC Faculty laboratory was used. Second, because the saw needs to be used with water while cutting the samples, they were dried for one night in the oven at 50 ºC. Finally, after cooling down the samples at ambient temperature, they were blown with compressed air to remove dust or remaining particles.

3.3.3. Image data acquisition

The samples were imaged with the Specim SWIR (1000 – 2500 nm) Hyperspectral camera located in the Geo-Science Laboratory in the ITC Faculty building, University of Twente, Enschede, The Netherlands.288 bands and 384 columns were recorded in each image. Samples were imaged in two batches. In the first batch 17 samples were imaged, and later 3 more samples were imaged in the second batch. One SWIR image was recorded for each sample except for the sample *sample260,* for which two sides were imaged since both presented interesting patterns. Moreover, the *sample094* was also imaged twice in different sides. The pixel size is 0.4 mm. After all the samples were imaged, they were processed to reflectance using the dark current and white reference measurements, using the ITC standard processing workflow.

3.3.4. Image pre-processing

After all the images of the samples were obtained and corrected, they were pre-processed to remove the noisy bands and correct for data errors and pixels with calibration issues. In addition, the image part not covering the samples was masked out. The steps are presented in the flowchart in figure 9 and explained below:

The steps are:

1. A spectral subset was done using the software ENVI. From 288 bands, that were initially recorded, starting in 907.16nm until 2523.43nm,17 bands were extracted to remove noisy bands

2. Destriping filter of HypPy3 software package (Bakker, 2012) was used with default values for the thresholds (*Max mean differences: 1000.00* and *Max standard deviation of differences: 500.0*) and **without** applying the offset and/or replacing bad pixels to detect pixels without values (Not a Number (NaN)) or values substantially different from their neighbour 9 pixels.

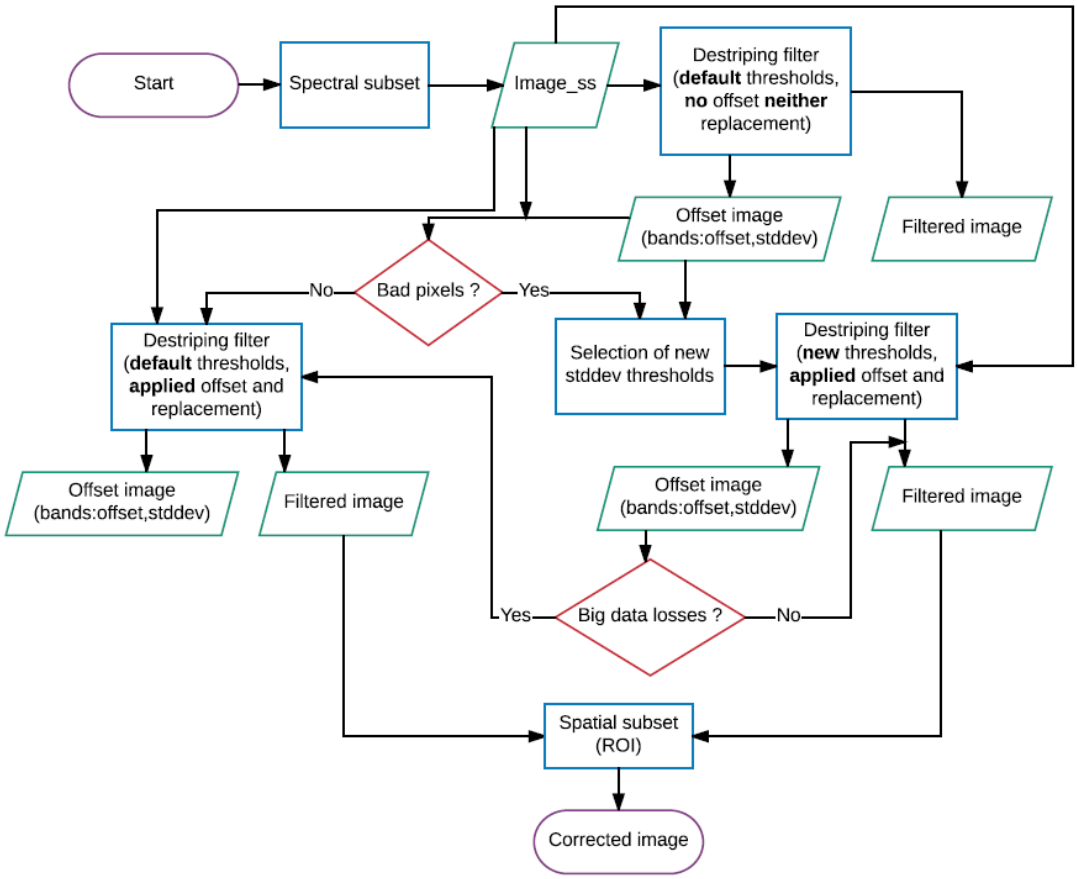

Figure 9. Flowchart summarizing the pre-processing steps followed for the correction of noisy bands and calibration issues in the images. Information must be supported by the explanation in the text.

3. The standard deviation band (stddev) of the output offset image was used to see the detected bad pixels (they were showed as extremely bright or dark pixels) and then in the input image, the detected bad pixels were evaluated to see if they certainly correspond to calibration issues that lead to blurry bands in the input image.

4. If they were not bad pixels (pixels with calibration issues), the destriping filter was applied again (in the original input image) with the default thresholds, this time the options of Apply offset and Replace bad pixels were ticked. Values of the detected bad pixels were replaced by new averaged values determined based on the 9 neighbouring pixels. (The output in this step was the final corrected image of the process)

5. If they were bad pixels (pixels with calibration issues), a new threshold for the standard deviation was selected that better corrected the bad pixels. Thresholds were selected considering the values of the bad pixels in the standard deviation band of the offset image. (Standards deviations with the same or higher values of the bad pixels wanted to be avoided)

6. After selecting the new threshold (step 5) the destriping filter was run again (in the original input image) with the new threshold and Apply offset and Replace bad pixels' options were used. Resultant standard deviation band was checked to evaluate **data losses;** it means parts of the image that are flagged with NaN values.

7. If there were big data losses (several pixels flagged as Not a Number (NaN)), the destriping filter was applied again with the default thresholds but this time the options of Apply offset and Replace bad pixels were ticked. Values of the detected bad pixels were replaced by new averaged values. These new values are determined based on the 9 neighbouring pixels. (The output in this step was the final corrected image of the pre-processing)

8. If there were not big data losses in step 6 (several pixels flagged as Not a Number (NaN)), the corrected image was the final output of the process.

9. After the pixels with calibration issues were corrected, a spatial subset was done by masking the image part not covering the sample using a Region of Interest (ROI) in ENVI software.

After the images were corrected and pre-processed different analyses were applied to process the images. This was done with the purpose of visualizing the main absorption wavelengths, collecting the endmembers and quantifying the minerals by classifying and unmixing the spectra in images. These processes are explained in the further sections.

3.3.5. Wavelength Mapping

Wavelengths maps were created to get a first overview of the dominating minerals in each pixel and the mineral patterns in each sample since they highlight the deepest absorption features of the spectra.

Wavelength maps are colour composites in which the information of the wavelength position and the depth of the deepest absorption features are combined and represented by different hues and brightness intensities, respectively, in the map (Van Ruitenbeek, Cudahy, van der Meer, & Hale, 2012). To obtain the information of the wavelengths position and depth of the absorption features Wavelength of Minimum maps are needed. They determine the wavelength of the smallest value of the spectrum as was explained in subchapter 3.3. For these minimum wavelength maps, the removal of the convex hull was done by subtraction since it is stated that this is the best option when the spectra are true reflectance spectra (all the values are between 0 and 1) (Bakker, 2016).

Moreover, the interpolated depth values of the absorption features can be stretched to increase the saturation and show patterns clearly. The stretch values can be determined automatically or iterative based on the resultant map. For this reason, when wavelength maps were used for the selection of the deepest features (endmember collection) less saturated maps were used, as the one of the *sample247* shown in figure 10 (A). On the contrary, when wavelength maps were used for the analysis of patterns more saturated maps were used as the one seeing in figure 10 (B).

A colour table is given as part of the output to help with the interpretation of the images. To illustrate, maps in Figure 10 show in magenta colour, wavelengths positions at 2214 nm, were spectra of dickite have their deepest absorption feature (black line figure 10 (C)). In yellow colours, wavelengths positions at 1900 nm, are showing mixtures of these dickite spectra with deep water absorption features (red line in figure 10 (C)). Small areas with cyan colours correspond to wavelengths positions of deep absorption features at 1413 nm (blue line in figure 10(C)).

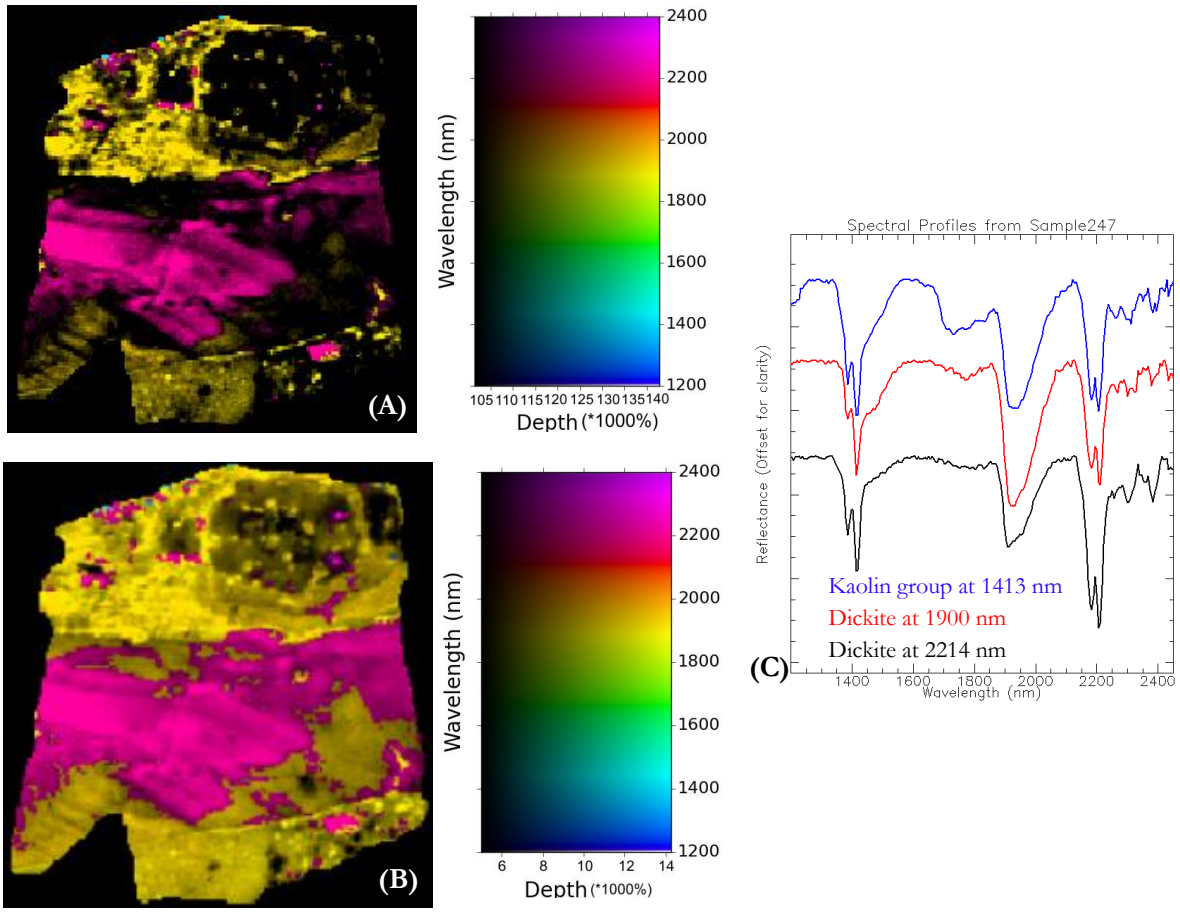

Figure 10. Wavelength maps in the range between 1200 - 2400 nm of sample247 and colour table for interpretation of the colours in the maps. (A) An automatic depth stretching value was used, stretching between 1014 - 1428%. (B) The interval of 500 - 1428 % was used to stretch depth values. (C) Continuum-removed spectra of main minerals recognized in *sample247*.

Wavelengths maps in different ranges were made depending on the minerals that were part of the samples, a summary of all the ranges used for the wavelengths maps can be found in appendix 2. Main ranges used in the alunite and kaolin group samples are explained below:

Alunite samples

In figure 11, main wavelength intervals that were used for the wavelength maps in the alunite samples are shown. Range 1, between 1200 – 2400 nm, was used to obtain an overview of all SWIR active minerals that are present in the samples and of overprinting patterns between them. Range 2, between 1460 – 1495 nm, was created to study the changes in the composition of alunite minerals. Range 3, interval between 2100 – 2250 nm, was used to differentiate mixtures of alunite. For some samples, wavelength maps were stretched to highlight differences amongst minerals. It means that for the wavelength of minimum maps needed as an input for the wavelength maps, the range 2100 – 2250 nm was used. Hence, deepest absorption features were found in this range. Then, in the wavelength maps the range used was 2150 – 2225 nm. Thus, deepest absorption features present just between 2150 – 2225 nm are coloured in the wavelength map.

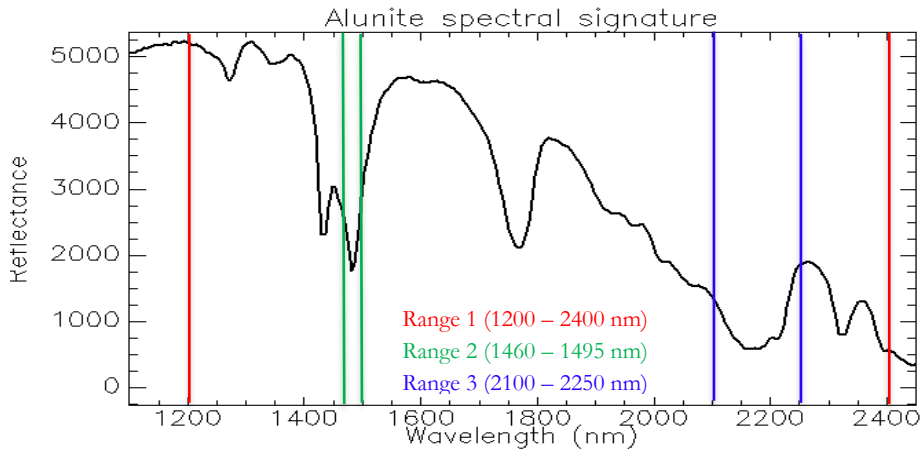

Figure 11. Representation of the main wavelength ranges used in the wavelength maps for processing the alunite samples.

Kaolin group samples

Figure 12 shows the main wavelength ranges used for the wavelength maps in the kaolin group samples. Range 1, between 1200 – 2400nm for the general overview of all SWIR active minerals that are present in the samples and of overprinting patterns between them. Range 2 (2100 – 2195 nm) was made for variations in the first absorption feature of the second doublet that shifts to longer wavelengths with variations in crystallinity. Finally, range 3 (1380 – 1409 nm) was made to evaluate the changes in the first absorption feature of the first doublet amongst the kaolin group minerals which varies in amongst the kaolin group minerals.

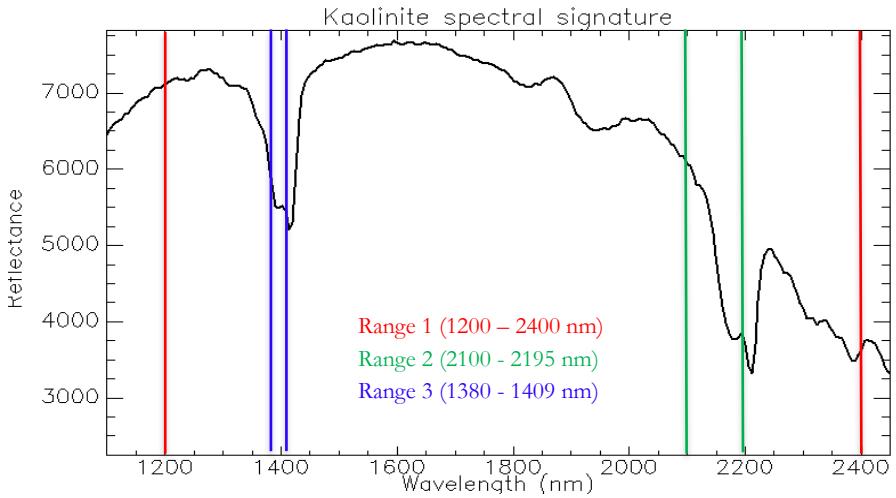

Figure 12. Representation of the main wavelength ranges used in the wavelength for processing the kaolin group samples.

3.3.6. Endmember collection

Different SWIR active minerals were found with the wavelength maps represented by different hues and purest minerals are represented by the brightest pixels (deep features) since they have the deepest absorption features. Nonetheless, purest minerals have their known spectra without showing mixtures in them (pure spectra). Therefore, an analysis of these spectra was required to build the endmember collection. This was done following the visual approach proposed in the Spectral Interpretation Field Manual (Pontual et al., 1997d). For each wavelength position recognized in the wavelength maps (hue) the deepest feature was identified and compared with reference spectra to check if there were different minerals that had similar

absorption wavelengths but different rest of spectra and the most typical were selected (dickite, alunite, pyrophyllite, kaolinite, halloysite, nacrite, gypsum, jarosite, illite, montmorillonite, and silicification). For the reference spectra, the USGS Spectral Library (Clark et al., 2007) and/or GMEX Spectral Library (Pontual et al., 1997d) were used.

For minerals, such as jarosite, and halloysite, not only the most typical spectra were selected to be part of the endmember collection but also spectra with slightly changes that also are present in the spectral libraries used as a reference. This was done to select spectra with the most typical and common characteristics of the minerals. The same case was for minerals frequently encountered with water content, such as pyrophyllite, two endmembers were selected. Regarding silicification, an endmember was selected even if it does not display any diagnostic absorption feature in the SWIR, since absorptions with non-diagnostic secondary components, such as water bands associated with fluid inclusions, give a subtle response (Pontual et al., 1997d).

For alunite minerals, spectra having the 1480 nm diagnostic feature at short wavelengths, at long wavelengths, at wavelengths in between and with different slopes in the spectra were encountered. In this case, a visual comparison was done to select the most extreme endmembers (1480nm feature at shortest, at longest and in wavelengths in between) since they are indicators of changes in the chemical composition (Figure 7).

For kaolinite minerals, an exhaustive visual comparison of the purest spectra found was carried out with the idea of selecting kaolinites with all the degrees of crystallization present in the samples because kaolinite crystallinity is related to the processes and conditions of formation of these minerals. The comparison was made with the reference spectra of kaolinite crystallinity presented in Figure 4(B) (Pontual et al., 1997c). Moreover, minerals from the kaolin group in general (dickite, nacrite, kaolinite and halloysite) help with the estimation of the relative temperature conditions of formation of the rock. Therefore, this estimation was made for the kaolin group minerals.

When the selection of the endmember collection was complete (20 endmembers), all the minerals were separated as either supergene or hypogene based on the literature present in section 2.1.3. Moreover, from the endmember collection, 8 minerals were selected and aggregated with their similar (if they have it) to represent results of the analysis of the images. To illustrated, pyrophyllite endmember was aggregated with the endmember of pyrophyllite with water content.

3.3.7. Spectral Angle Mapper

Spectral angle mapper is a hard classification method for automatic comparisons between spectra (EXELIS, 2013). Image spectra are matched with known spectra, in this case coming from the endmember collection. Most dominant minerals are recognized in each pixel. Thresholds must be used to control the match. In this research, the threshold assigned for the maximum angle amongst the spectra was 0.1 rad to guarantee that certainly similar pixels were classified. Statistics of the classified images were used to obtain the abundance of the most dominant minerals per pixel.

3.3.8. Spectral unmixing

A spectral unmixing was carried out to determine the optimal fraction abundances of all the minerals present in each pixel since real mixtures comprise not only dominant minerals but also less abundant minerals. The algorithm used was the Iterative implementation of Spectral Mixture Analysis (ISMA). It selects the optimal endmember set for each pixel by evaluating the change in the root-mean-square (RMS) error through all the iterations and finding the critical iteration. The critical iteration is the iteration were the optimal endmember set was found (Iordache, Bioucas-Dias, & Plaza, 2011). This is done by removing in each iteration the

mineral with the lowest fraction abundance until only one endmember is left with the albedo endmember. The albedo or shadow endmember is a multiplicative factor to account for albedo conditions that ISMA adds automatically with uniform reflectance. (Rogge, Rivard, Jinkai, & Jilu, 2006). The ISMA algorithm was chosen because it is effective in obtaining abundance fractions that are physically realistic since it considers that predicted abundances are more accurate when only the needed endmembers are used (Tobergte & Curtis, 2013).

To implement the ISMA, the original approach proposed by Rogge et al. (2006) was carried out because this is the more efficient option when ISMA is used in hyperspectral data. This approach states that only thresholds for the critical iteration and the number of iterations are chosen. In this research, the threshold for the critical iteration (*cthr)* was 0.5, which means that the differences in the RMS error (Δ*rmse)* must be more than 50% of the RMS value ($rmse_{it}$) of the last iteration to be identified as critical iteration. Figure 13 illustrates this procedure. Regarding the number of iterations, the default value (2 iterations) was used since it is advised to use 2 when hyperspectral images are being processed (Tobergte & Curtis, 2013).

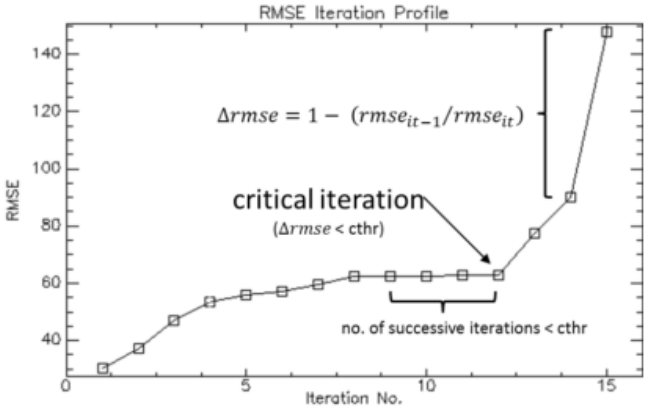

Figure 13. Example of an RMS error profile for 15 iterations in which 16 endmembers were used in the ISMA (including albedo) on a hyperspectral image (Tobergte & Curtis, 2013).

Statistics of the ISMA were obtained for the quantification of the partial abundance of each of the endmembers. However, ISMA percentages were normalized since the albedo endmember is not part of the real mineral mixtures. Hence, it was removed from the quantification.

3.4. Geochemical analysis

As a validation of the spectral behaviors observed in the supergene and hypogene versions of alunite minerals, the chemical analyses explained below were carried out by using the instruments from the Geo-Science Laboratory (GSL) of the ITC Faculty, University of Twente. The analyses were done on two alunite rich samples, that were selected due to:

- *Sample243* is assumed to be the result of supergene processes as it appears in pure, late stage alunite veins that cut across other altered lithologies.
- *Sample260* where alunite was formed by hypogene processes being pinkish in colour and filling vugs in the same way as described in Arribas et al. (1995).

3.4.1. Inductively Coupled Plasma analysis

Inductively Coupled Plasma Optical Emission Spectroscopy (ICP-OES) was executed with the PerkinElmer 8300dv ICP-OES. It is a technique used for the detection of elemental concentrations in samples, in this research especially Na, K, Y, Zr, amongst others. Na and K are interesting because of the different compositions of alunite minerals and Y and Zr are interesting to differentiate hypogene from supergene alunite in the Rodalquilar caldera, according to Arribas et al. (1995).

Samples must be in a liquid state to be injected into the instrument. Therefore, solid samples require acid digestion. The liquid is then vaporized and its atoms collide with a plasma that imparts additional energy. As a result, photons are emitted with a characteristic energy level that depends on the structure of the atoms (Hou Xiandeng, 2000). This electromagnetic radiation is emitted at typical wavelengths that depend on the elements. Afterward, this radiation is collected and converted into electronic signals that are further changed into concentration values of the elements (Life & Sciences, 2004).

For the vuggy quartz sample (*sample260)* alunite was carefully scratched out of the vugs with a tungsten steal-tipped instrument, taking care not to harvest any of the other minerals. *Sample243* is almost entirely composed of alunite but care was taken not to include any of the accessory jarosite. The material was ground and sieved through a screen having about 80 meshes per linear inch (80 μm). Around 50 mg of the resultant powder was then mixed in beakers with sulfuric acid at 98%. The mixtures were heated for 50 hours at a temperature around 85ºC. Watch glasses were used on top of the beakers. At the end of this time, the watch glasses were removed and the mixtures were left for 24 hours cooling down. The acid residues were further diluted with ultrapure water (18 MΩ.cm) to ~12 ml (exact volume was determined via balance). Finally, the diluted samples were placed in tubes after being filtered with a 0.45 μm Watchmann filter.
For quality control *Sample260* was measured in triplet and *sample243* was measured in duplo, two procedural blanks were also measured.

3.4.2. Thermogravimetric analysis

Thermogravimetric analysis (TGA) allows the identification of mass changes in minerals when they are being controlled heated in a furnace with a controlled atmosphere. Depending on the composition of the minerals, the weight losses and decomposition reactions occur at different temperatures. The samples were ground and placed in a pan that is in a furnace supported by a precision balance.

The instrument used is a PerkinElmer TGA 8000. A flowing nitrogen atmosphere was selected to control the environment and about 10mg of each sample was used in duplo. The heating rate was 5ºC min^{-1}, from 30 to 900ºC. The isothermal temperature of the furnace was regulated to a period of 10min to provide a uniform rate of decomposition. The settings were taken from a previous thermogravimetric analysis conducted in potassium rich alunite minerals by Frost and Wain (2008).

4. RESULTS

The present chapter introduces the results of all the steps that were taken to develop this research. From the ASD FieldSpec measurements through the sample selection, pre-processing and image analysis which includes results from the Wavelength mapping, Spectral Angle Mapper, and Iterative Spectral Unmixing Analysis. Finalizing with the results of the aggregated mineral abundances.

4.1. Non-imaging spectroscopy

The combined dataset of historic ASD measurements and those measured in this work resulted in a dataset of 265 rock samples with a total of 779 spectra measured (2-3 spectra per sample. Based on the differentiation amongst samples containing either alunite or minerals from the kaolin group as first or second mineral, two different spectral libraries were created.

In figure 14, first and second minerals are shown in the columns called TSA_S Mineral1 and TSA_S Mineral2, while TSA_S Group1 and TSA_S Group2 refers to the family group of the minerals. Figure 15 shows examples of ASD spectra of alunite minerals coming from the point measurements in *sample260*. They cover the wavelength range from 350 to 2500 nm. Summary of the complete spectral library and the TSA interpretation can be found in appendix 1.

Index	TSA_S Mineral1	TSA_S Group1	TSA_S Mineral2	TSA_S Group2
30:Rod00511.asd.sco.txt	Kaolinite	Kaolin	Pyrophyllite	Al(OH)-2
31:Rod00510.asd.sco.txt	Kaolinite	Kaolin	Pyrophyllite	Al(OH)-2
32:Rod00509.asd.sco.txt	Kaolinite	Kaolin	Pyrophyllite	Al(OH)-2
33:Rod00852.asd.sco.txt	Kaolinite	Kaolin	K_Alunite	Sulfate
34:Rod00185.asd.sco.txt	Kaolinite	Kaolin	Na_Alunite	Sulfate
35:Rod00290.asd.sco.txt	Kaolinite	Kaolin	Gypsum	Sulfate
36:Rod00293.asd.sco.txt	Kaolinite	Kaolin	Gypsum	Sulfate
37:Rod00292.asd.sco.txt	Kaolinite	Kaolin	Gypsum	Sulfate
38:Rod00850.asd.sco.txt	Kaolinite	Kaolin	Gypsum	Sulfate
39:Rod00009.asd.sco.txt	Dickite	Kaolin	NULL	NULL
40:Rod00369.asd.sco.txt	Dickite	Kaolin	Halloysite	Kaolin
41:Rod00153.asd.sco.txt	Dickite	Kaolin	Halloysite	Kaolin
42:Rod00054.asd.sco.txt	Dickite	Kaolin	Halloysite	Kaolin
43:Rod00297.asd.sco.txt	Dickite	Kaolin	Halloysite	Kaolin
44:Rod00295.asd.sco.txt	Dickite	Kaolin	Halloysite	Kaolin
45:Rod00296.asd.sco.txt	Dickite	Kaolin	Halloysite	Kaolin

Figure 14. Automatic interpretation of spectral signatures in The Spectral Geologist using the algorithm The Spectral Assistant, showing files interpreted with kaolinite and dickite as the first mineral and pyrophyllite, K rich alunite, Na alunite, gypsum.

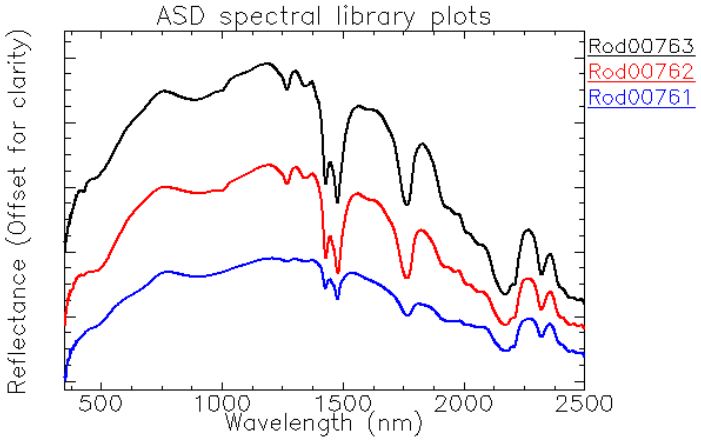

Figure 15. Three ASD spectra from *sample260* showing the signature of alunite minerals. They correspond to the spectra called Rod00761, Rod00762, and Rod00763 in the spectral library.

4.2. Laboratory Imaging spectroscopy

4.2.1. Sample selection

Interpolated depth and interpolated wavelength parameters were extracted from the ASD spectral library of alunite minerals and kaolin minerals. Parameters results were condensate in the scatters plots that can be seen in figure 16 and figure 18. Each dot represents the spectral signature of a point measurement in the corresponding wavelength range. Filled circles mark spectra of the selected samples. Open circles are the spectra of the rest of the samples that were measured. Red lines connect spectra of the same (selected) sample. In total 20 samples, from the alunite and kaolin group samples, were selected to carry out the research. In the next paragraphs selected alunite and selected kaolin group samples are shown:

Alunite

Eleven samples with alunite content were selected to carry out the spectral and chemical evaluation of the alunite minerals and the study of overprinting patters. They were selected based on the scatter plots in figure 16 following the criteria explained below:

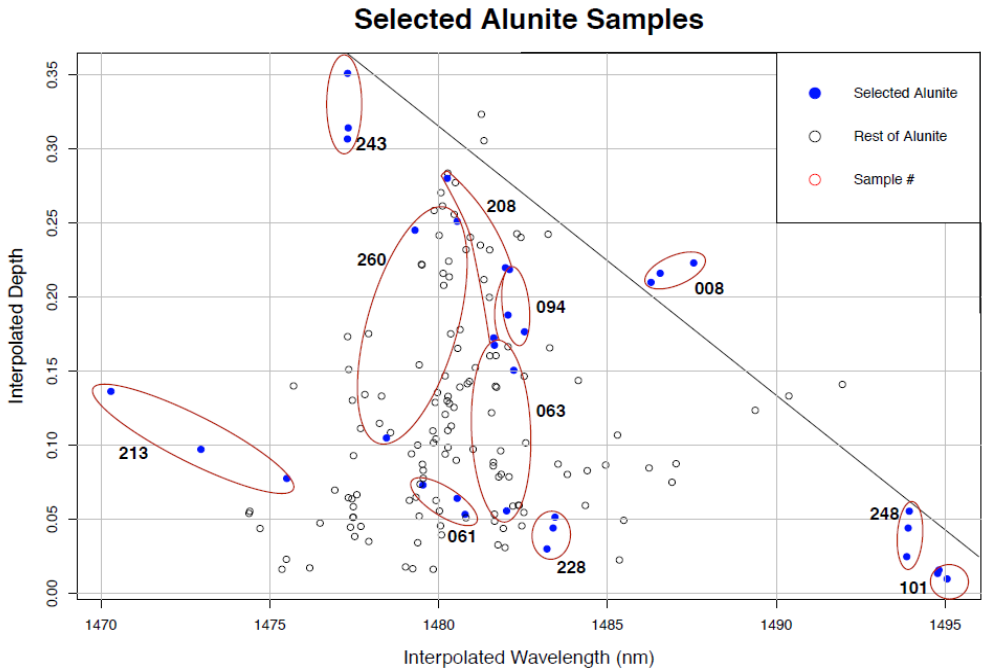

Figure 16. Variation of the absorption features of the samples with alunite minerals with the variation in composition. These parameters (Interpolated depth Vs. Interpolated wavelength) are derived from ASD spectral data. The black line indicates a trend explained in the text.

Firstly, a relevant characteristic to highlight from the scatter plot of alunite samples (Figure 16) is a tendency of the samples observed from deep absorption features at shorter wavelengths to shallow absorption features at longer wavelengths. This allows drawing a trend line that alunites follow in this graph, from K rich alunites at the top left to Na rich alunites at the bottom right. Secondly, the selected samples at short wavelengths were *sample213* and *sample243* with shallow and deep absorption features, respectively. The first sample contains jarosite, which can shift the position of the alunite absorption features to shorter wavelengths. *Sample243* was collected from a late stage alunite vein and it is assumed to be the result of supergene processes. Selected samples at very long wavelengths were *sample248* and *sample101* since they represent the Na rich extreme. Moreover, *sample008* in the middle of the trend line that defines the behavior of the alunites was also selected to complete the study along this line. Finally, samples in the middle of the plot were chosen considering that they are the average and most common. That is the case of *sample061* and *sample228* at shallow depths, and *sample260*, *sample063, sample094* and *sample208* from the middle of the graph

with deeper absorption features. Samples in the middle of the graph correspond to samples with features in the water absorption bands (*sample063* and *sample094),* mixtures (*sample061, sample228)* and pure alunites (*sample208* and *sample260).*

Selected alunite samples are shown in the map of figure 17 where they are plotted on top an alteration map proposed by Arribas (1995). *Sample243, sample094,* and *sample063* are located in the supergene alteration zone where poorly crystalline kaolinite, jarosite, gypsum and K rich alunite are found. *Sample228* and *sample208* are in the vuggy silica zone which is generally dominated by quartz, alunite, kaolinite amongst others *Sample260* and *sample101* are in the advanced argillic alteration zone dominated by either quartz, alunite and kaolinite or quartz, kaolinite, and illite-smectite. Moreover, pyrophyllite, dickite, and pyrite are also found here. *Sample213, sample061,* and *sample248* are located in the intermediate argillic alteration zone that in general is dominated by quartz, kaolinite, illite, alunite. Finally, the *sample008* is located out of the delimitation of the alteration zones proposed by Arribas et. al. (1995). A summary of the selected alunite samples can be found in appendix 3.

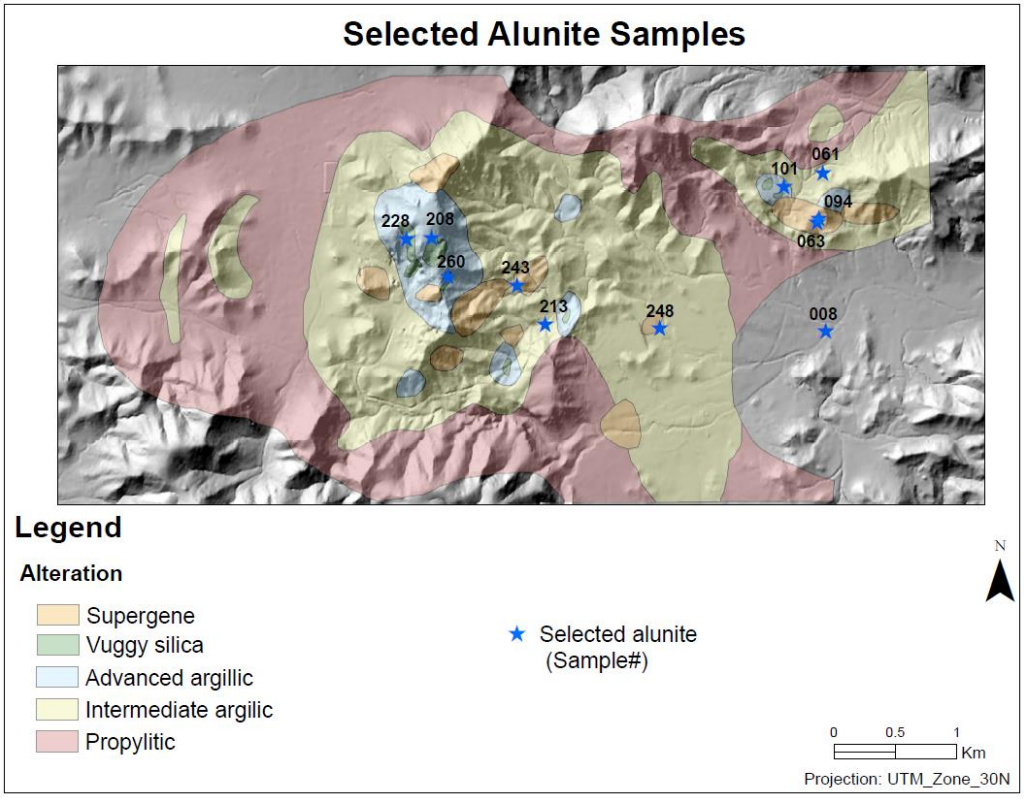

Figure 17. Location of selected alunite-bearing samples. Background map shows the alteration zones according to Arribas et. al. (1995) on top of a hillshade of a 5 m Digital Elevation Model (DEM).

Kaolin group

Nine samples with minerals from the kaolin group were selected for the determination of the crystallinity degree in kaolinites and the study of overprinting patterns. Based on the scatter plot in figure 18, samples with the most extreme characteristics are *sample133* at shorter wavelengths with deep absorption features and *sample219* at long wavelengths. In addition, *sample257* at long wavelengths with shallow absorption features. These three samples (*sample133, sample219,* and *sample257*) represent the most extreme characteristics for crystallinity variables. *Sample176* was selected based on very deep absorption features due to the mixture with pyrophyllite that enhances the depth of the kaolinite absorption features.

Moreover, samples from the middle of the scatter plot were also selected, such as *sample169* and *sample103* to complement the selection at short wavelength. Finally, *sample127, sample247,* and *sample129* were chosen firstly due to its absorption features at very long wavelengths because of the content of jarosite and gypsum. Secondly, due to the possibility to study overprinting patterns. Because TSA interpretation showed a high content of dickite (high temperature and highly crystalline mineral) with jarosite and gypsum, being dickite a hypogene mineral and, jarosite and gypsum a supergene mineral. This mixture can be seen in the plot as the spacing between the three measurements of the sample since jarosite and gypsum have shallower features in this wavelength range than dickite.

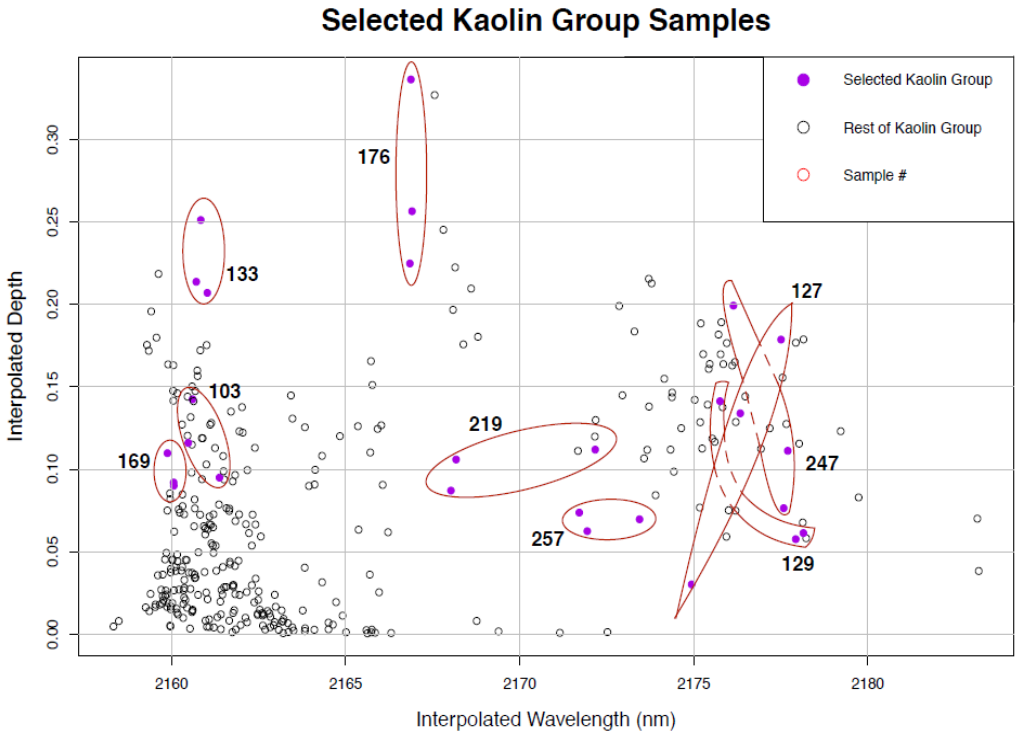

Figure 18. Variation of the absorption features of the samples with minerals from the kaolin group related with the variation in the crystallinity. These parameters (Interpolated depth Vs. Interpolated wavelength) are derived from ASD spectral data.

Selected kaolin group samples are shown in the map of figure 19. *Sample257* is located in the area dominated by a supergene alteration. *Sample247* is in the vuggy silica alteration zone and *sample176, sample127,* and *sample103* are in the advanced argillic alteration zone. *Sample129, sample169,* and *sample219* are in the intermediate argillic zone. Finally, *sample133* is located out of the alteration zone maps proposed by Arribas et. al. (1995). A summary of the selected kaolin group samples can be found in appendix 3.

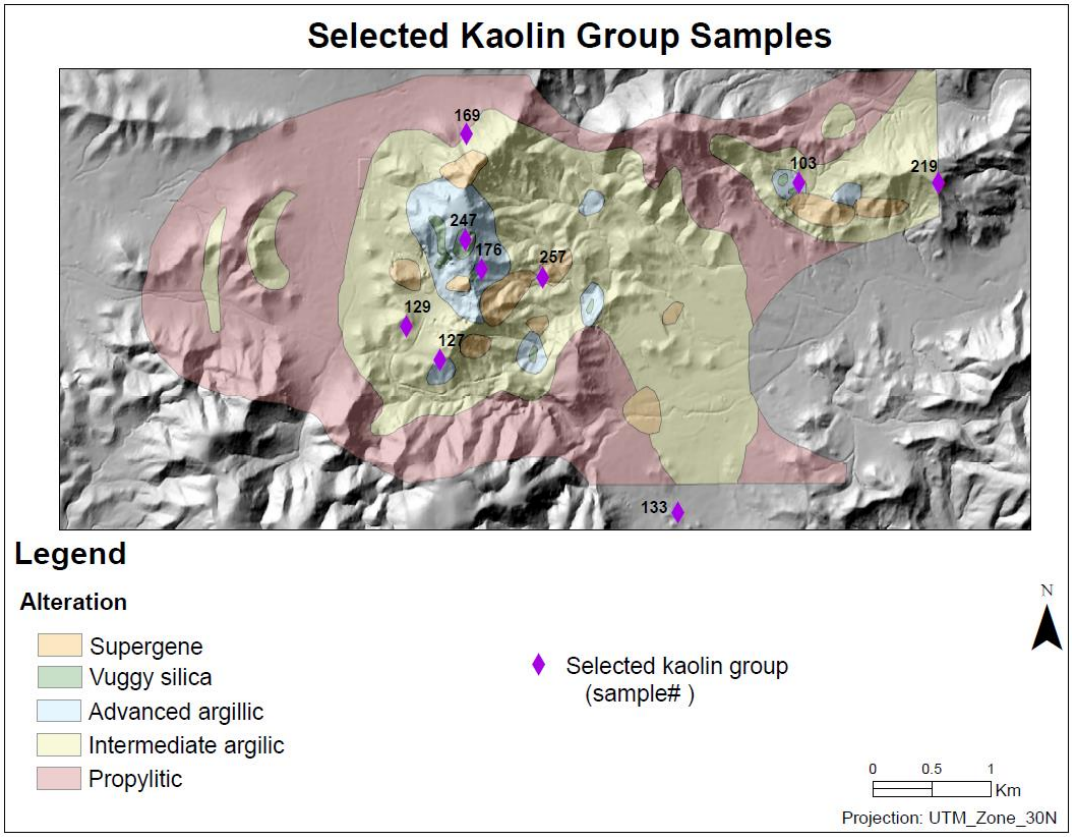

Figure 19. Location of selected kaolin group-bearing samples. Background map shows the alteration zones according to Arribas et. al. (1995) on top of a hillshade of a 5 m Digital Elevation Model (DEM).

4.2.2. Image pre-processing

From the 20 samples selected 22 images were acquired (20 samples; one image each of the samples and two images of *sample260* and *sample094*). Below are the results after the various pre-processing steps:

Figure 20 (A) shows a spectrum from *sample260-sideA* before the spectral subsetting and pre-processing procedure was done. The spectral range goes from 907.16nm until 2523.43nm. Figure 20 (B) shows the same spectrum from *sample260-sideA* after the spectral subsetting and pre-processing. The resultant 271 bands cover the wavelength range from 1004.62 nm to 2523.43 nm.

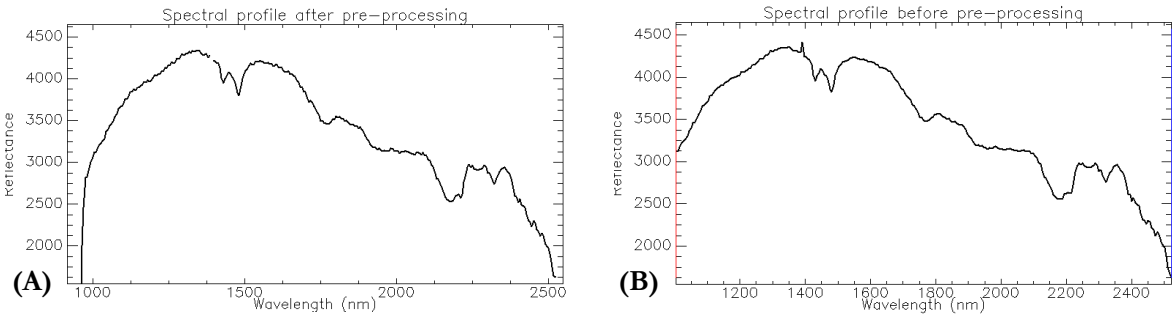

Figure 20. Spectra of pixel 229,264 from *sample260* before (A) and after (B) the spectral subset was applied.

Subsequently, figure 21 shows two colour composite (RGB: 1390 nm, 2233 nm, 2289 nm) of *sample260-sideA* before (A) and after (B) the destriping filter and the mask were applied. The destriping filter and the

application of a mask, made with a region of interest of each sample, provided images without bad bands and the background that could have affected the analyses in the images. Background values were assigned to NaN (Not a Number) to avoid its influence in the statistics of the images.

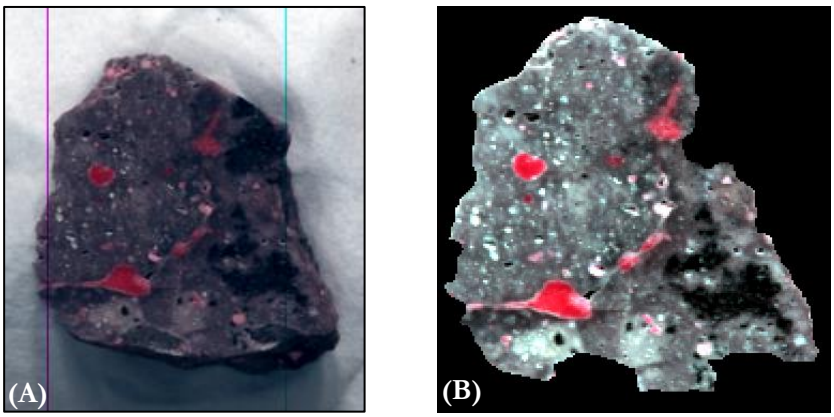

Figure 21. Colour composite of a SWIR (RGB= 1390 nm, 2233 nm, 2289 nm) image of *sample260-sideA* before (A) and after (B) the spectral subset, destriping filter, and mask corrections were applied.

Once the 22 images were pre-processed, the image analysis was carried out. Results of this started with the outcome of the Wavelength Mapping algorithm, followed with the spectral differences between hypogene and supergene alunite and the crystallinity differences amongst kaolinites. Then, the endmember collection created based on the wavelength maps, the Spectral Angle Mapper and the Iterative Spectral Mixture Analysis results were obtained.

4.2.3. Wavelengths Mapping

Results of the wavelength maps show, from the chosen wavelength range, the wavelength of the deepest absorption features in different hues, and the depth of these feature in increasing brightness. Results are illustrated with *sample260-sideA* from the selected alunite samples and *sample219* from the kaolin group samples.

Alunite samples

Results of the first and widest range used (1200 - 2400 nm) for the wavelength maps of the alunite samples shows the most representative minerals with the deepest absorption features. As an illustration, the wavelength map of *sample260-sideA,* which is an alunite sample, can be seen in figure 22. Cyan colours (wavelengths at 1481 nm) show pixels with alunite (spectrum in figure 23 (B)) and pixels with mixtures of alunite and pyrophyllite (spectrum in figure 24 (A)) which cannot be differentiated in this image. Magenta colours (wavelengths around 2170 nm) shows also pixels with alunite minerals due to a small tilt of the spectrum that makes this feature the deepest. Additionally, other areas with this magenta colour are pyrophyllite (figure 24 (B)) the same as the yellow pixels (wavelengths around 1925 nm). Finally, the sample is strongly silicified (brownish hues; spectrum in figure 23 (A)).

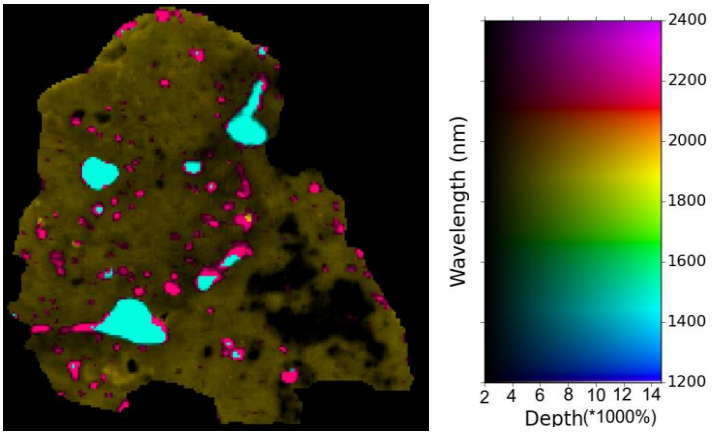

Figure 22. Wavelength map for the wavelength range between 1200 - 2400 nm of the alunite *sample260-sideA*. For the interpretation of the colours, the reader is referred to the text above.

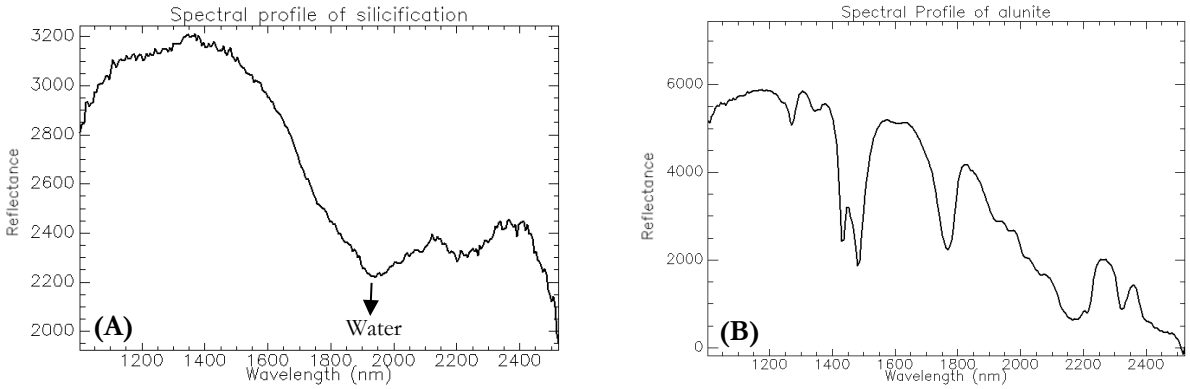

Figure 23. Spectra from *sample260-sideA* showing the signature of (A) silicification with broad water bands as secondary component and (B) alunite with the second absorption feature of the doublet at 1481 nm.

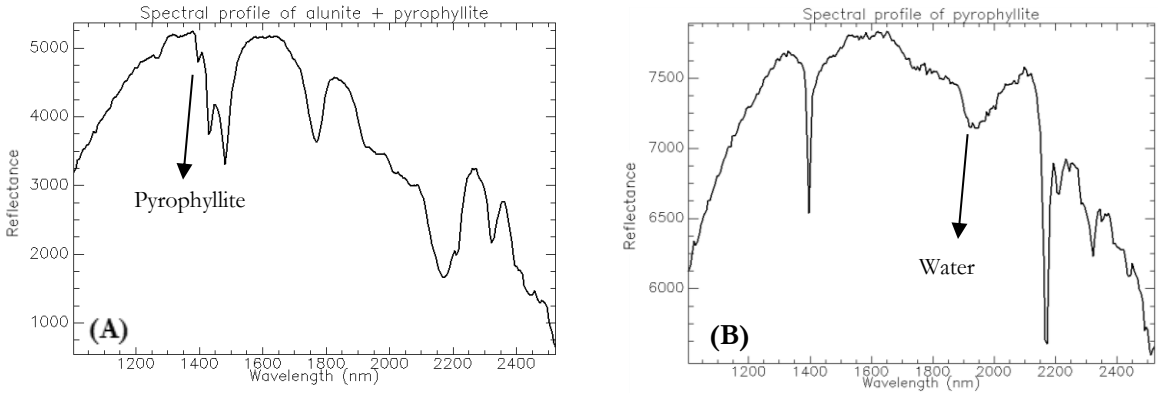

Figure 24. Spectra from *sample260-sideA* showing the signature of (A) an alunite with some content of pyrophyllite and (B) a spectrum of pyrophyllite with water content.

Results of the second wavelength map covering the range between 1460 – 1495 nm, should illustrate shifts in the alunite feature. As an example, *sample260-sideA* is used, which contains alunite in the vugs (Figure 25Figure 25). Through the image, no compositional shifts in the alunites can be seen. Pixels are all yellowish (wavelength 1481 nm). However, when jarosite is present in the samples, as in *sample213* and *sample208,* differences between alunite and jarosite are seeing in this maps since jarosite has a diagnostic absorption feature around 1468 – 1477 nm.

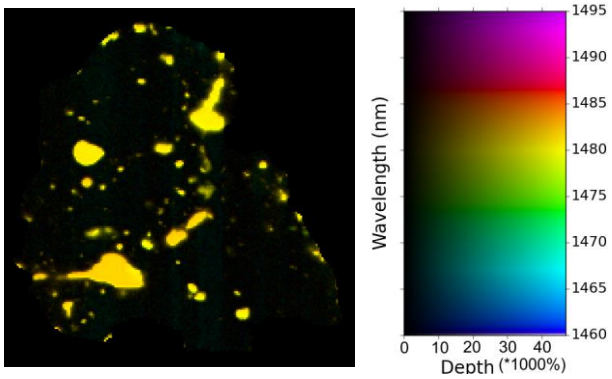

Figure 25. Wavelength map for the wavelength range between 1460 - 1495 nm of the *sample260-sideA* showing alunite minerals. For the interpretation of the colours, the reader is referred to the text above.

The third range of the wavelength maps is between the 2100 – 2250 nm. However, in the case of *sample260-sideA*, wavelength maps of the third range were stretched to the range between 2150 – 2225 nm (figure 26), this helps with the differentiation amongst pixels with pyrophyllite content and alunite and shows content of nacrite. Pixels with reddish colours (wavelength 2221 nm) are minerals from the kaolin group, mainly nacrite (figure 27 (A)). Moreover, mixtures of nacrite with alunite are also in reddish colours (wavelength 2221 nm) (figure 27 (B)). Green colours (wavelengths around 2177 nm) corresponds to alunite. Pixels in cyan (wavelengths around 2166 nm) are mixtures of pyrophyllite with alunite, however, the differences amongst pixels with pure pyrophyllite and mixtures of pyrophyllite and alunite are not shown.

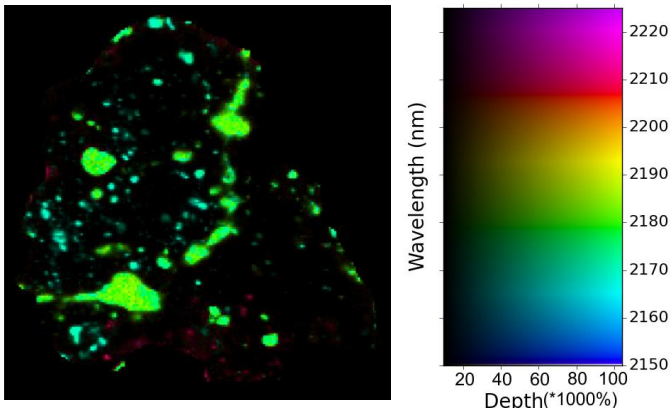

Figure 26. Wavelength map for the wavelength range between 2150 – 2225 nm of the alunite *sample260-sideA*. For the interpretation of the colours, the reader is referred to the text above.

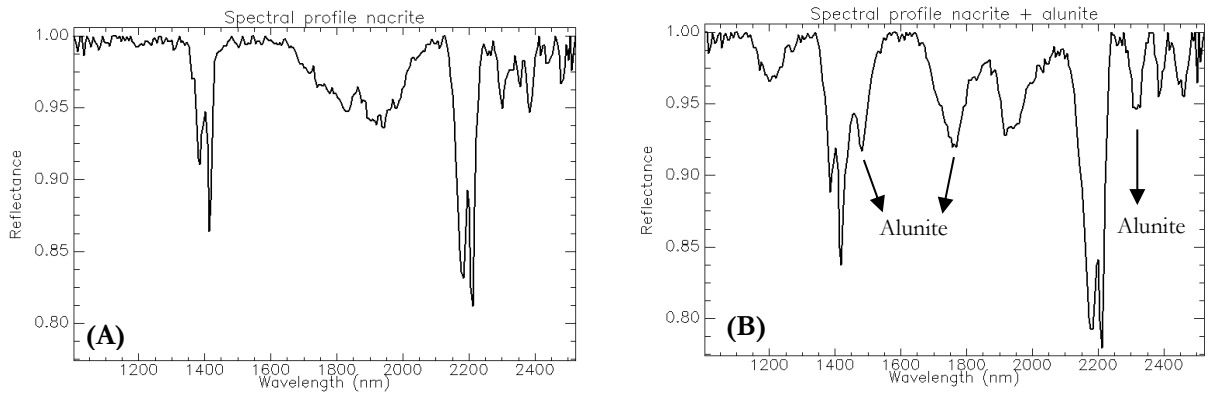

Figure 27. Continuum-removed spectrum from *sample260-sideA* having the deepest absorption feature at 2221 nm. In figure (A), the spectrum corresponds to a nacrite mineral. In figure (B), the spectrum corresponds to a mixture of nacrite with alunite.

Kaolin group sample

Results of the first wavelength map used for the general overview of the kaolin group samples (1200nm-2400nm) are illustrated with the *sample219,* this is shown in figure 28. Cyan pixels (wavelengths at 1413 nm) shows kaolinite minerals (figure 29 (A)). Magenta pixels (wavelengths around 2211 nm) correspond to dickite (figure 29 (B)). A few brown dots are encountered that are showing signatures from kaolin group minerals, however, the spectra are too noisy to identify the exact mineral species of the kaolin group minerals.

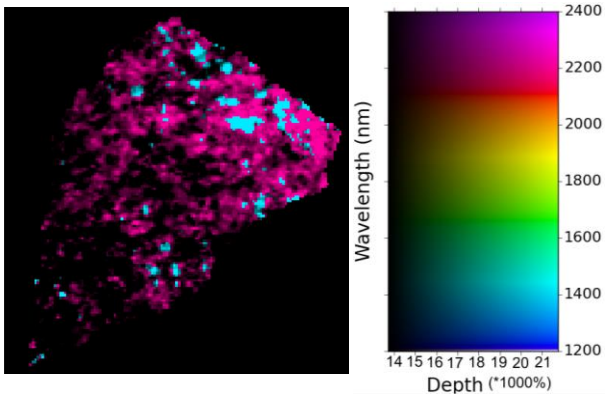

Figure 28. Wavelength map for the wavelength range between 1200 - 2400 nm of the kaolin group *sample219*. For the interpretation of the colours, the reader is referred to the text above.

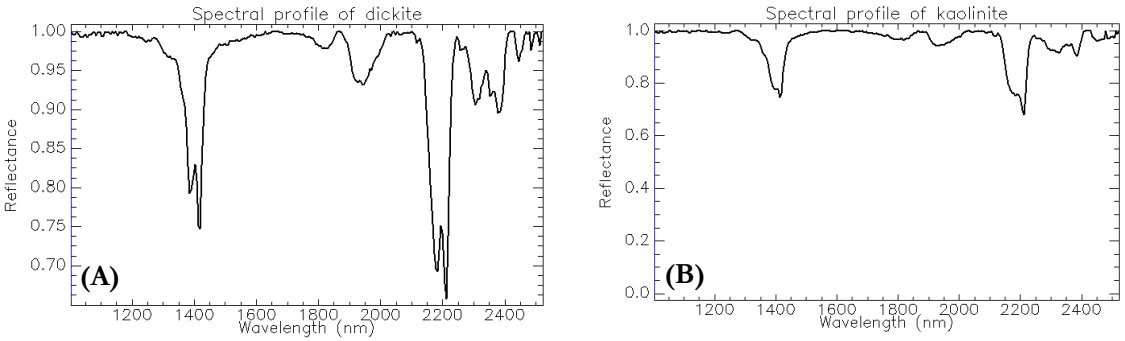

Figure 29.Continuum-removed spectrum from *sample219* having the deepest absorption feature at 2221 nm in figure (A), corresponding to a dickite spectrum. In figure (B), the spectrum corresponds to kaolinite with the deepest absorption at 1413 nm.

Results in *sample219* (figure 30) of the second range used (2100 – 2195 nm) in the wavelength maps show differences in the first absorption feature of the second doublet in spectra of kaolin group minerals. Orange pixels (wavelengths at 2177 nm) show minerals of kaolinite with not well develop absorption feature. Magenta colour (wavelengths around 2183 nm), which is the main component of the rock sample, corresponds to dickite.

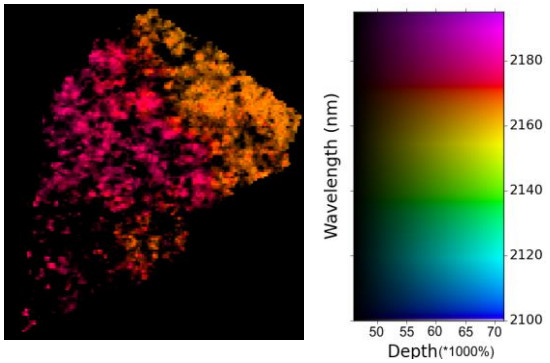

Figure 30. Wavelength map for the wavelength range between 2100 - 2195 nm of the kaolin group *sample219*. For the interpretation of the colours, the reader is referred to the text above.

The third wavelength range used for the wavelength maps of the kaolin group samples (1380 – 1409 nm) shows for *sample219* (figure 31) differences amongst the kaolin group minerals. Pixels in yellow (wavelengths around 1396 nm) show medium crystalline kaolinite. Light green pixels (wavelengths at 1390 nm) show a better crystalline kaolinite. Darker green pixels (wavelengths at 1390 nm) show kaolinite minerals and light blue colours (wavelengths 1385 nm) show dickite minerals.

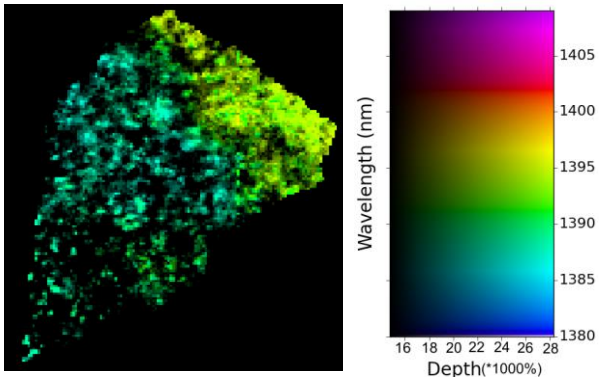

Figure 31.Wavelength map for the wavelength range between 1380 – 1409 nm of the *sample219*. For the interpretation of the colours, the reader is referred to the text above.

4.2.4. Endmember collection

From the 22 images that were acquired, 20 endmembers were selected. Table 2, shows the minerals selected as endmembers, the final 8 endmembers used for visualization of quantification results, how they were aggregated and the origin of formation (either by hypogene or supergene processes) based on literature (see subsection 2.1.3). Figure 32, figure 33, figure 34 and figure 35 show spectra of the selected endmembers.

Table 2. Endmember minerals selected using Wavelength maps. Endmembers used for visualization of the quantification results and origin of the formation of the minerals based on literature (see subsection 2.1.3).

Endmembers	Aggregation for visualization	Origin
Silicification	Silicification	Hypogene
Alunite long	Alunite long	Hypogene
Pyrophyllite Pyrophyllite + water	Pyrophyllite	Hypogene
Dickite	-	Hypogene
Nacrite	-	Hypogene
Kaolinite HX Kaolinite HX_W	Kaolinite HX	Hypogene
Illite	-	Hypogene
Montmorillonite	Montmorillonite	Hypogene
Kaolinite MX	-	Hypogene
Halloysite dehydrated	-	Hypogene
Halloysite hydrated	-	Supergene
Alunite medium	Alunite medium	
Kaolinite PX	Kaolinite PX	Supergene
Gypsum	-	Supergene
Jarosite overall	-	Supergene
Jarosite1936	-	Supergene
Alunite short-sideA Alunite short-sideB	Alunite short	Supergene

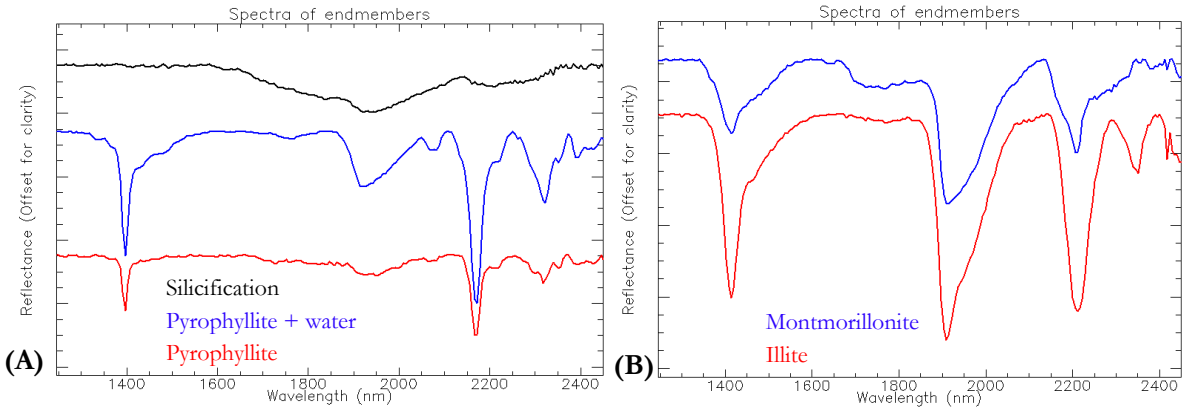

Figure 32. Continuum-removed spectra of selected endmembers: (A) silicification, pyrophyllite + water, and pyrophyllite; (B) Montmorillonite and illite.

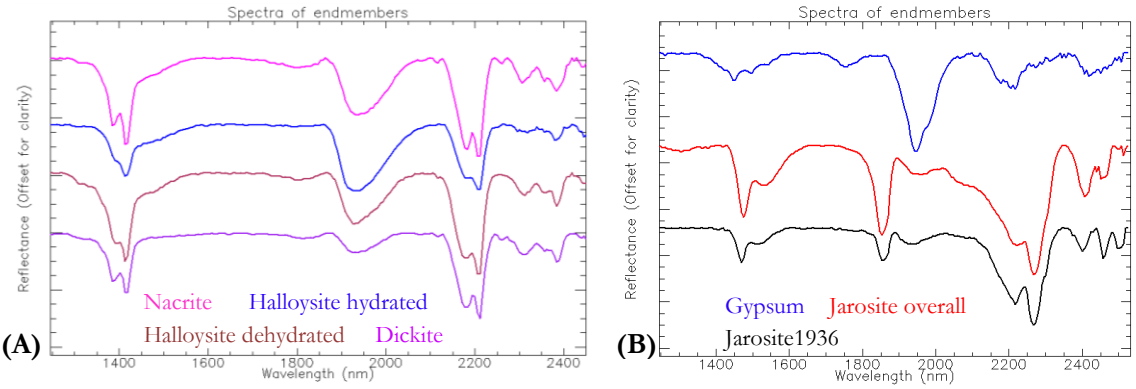

Figure 33. Continuum-removed spectra of selected endmembers: (A) Nacrite, Halloysite hydrated and dehydrated and dickite; (B) Gypsum, jarosite overall and jarosite 1936.

Due to variable water feature depth, endmembers of kaolinite and pyrophyllite can have two spectra (*kaolinite HX* and *kaolinite HX_W, pyrophyllite* and *pyrophyllite + water)*. In the case of jarosite, it has two endmembers: the more common one (*jarosite overall)* and one that has an additional feature at 1926 nm (*jarosite1936)*. The former corresponds to jarosite of GMEX spectral library (Pontual et al., 1997d) and the latter to the USGS spectral library (Jarosite SJ-1 (H3O,10-20%)) (Clark et al., 2007). Hence, both were kept.

As endmembers for alunite four spectra were chosen. Two endmembers, *alunite short-sideA,* and *alunite short-sideB,* for the alunite with the absorption features of the first diagnostic doublet at short wavelength 1430 nm and 1482 nm. The inclusion of the two alunite short endmembers in the collection is due to differences in the slope of the spectra between 1914 – 2082 nm. One endmember, *alunite long,* that has its diagnostic doublet at longer wavelengths (1441 nm and 1498 nm). The last endmember for the alunite minerals is *alunite medium* which has the absorption doublet at wavelengths in between the other three endmembers, this is 1436 nm and 1486 nm (see figure 34).

For the kaolinite endmembers, results of the visual determination of the crystallinity show that the chosen endmembers are highly crystalline kaolinite (*kaolinite HX),* medium crystalline kaolinite (*kaolinite MX),* and poorly crystalline kaolinite (*kaolinite PX)* (See figure 35).

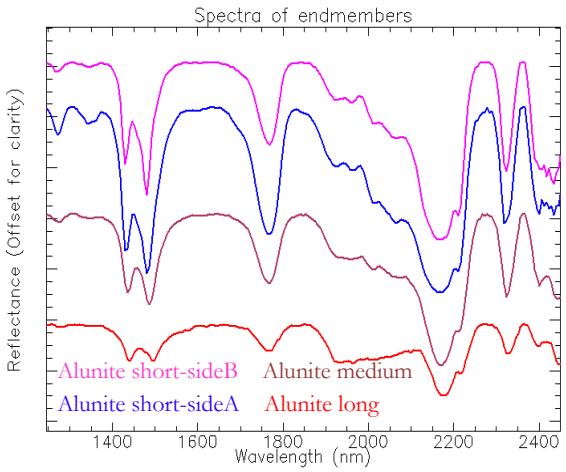

Figure 34. Continuum-removed spectra of selected endmembers of alunite minerals (For differences reader is referred to the text).

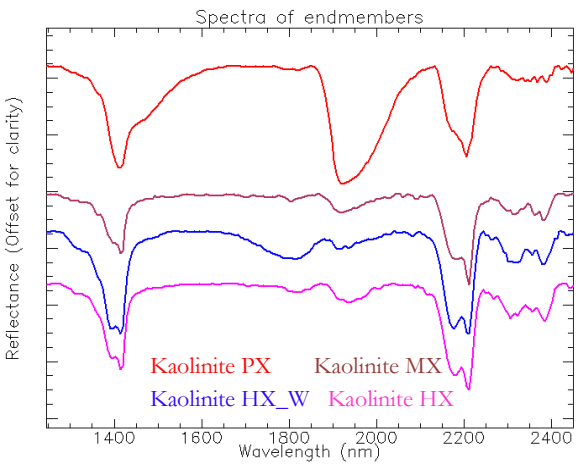

Figure 35. Continuum-removed spectra of selected endmembers of kaolinite minerals with varying crystallinity degrees.

4.2.5. Spectral Angle Mapper

Results of the Spectral Angle Mapper show the most dominant minerals in each pixel since the classification is based on the idea that one pixel represents one single material. For most of the samples, more than 95% of the image is classified. However, for other samples, such as *sample094, sample094-small,* and *sample243*, more than 20% are unclassified pixels and for *sample133* and *sample061,* more than 50% of the sample are not classified. Quantification of the results of the 22 samples can be found appendix 4.

Alunite sample

As an illustration, figure 36 shows the classified image of *sample260-sideA* from the selected alunite samples. Main minerals recognized were silicification, alunite, montmorillonite, pyrophyllite, halloysite, nacrite. Different types of alunite were assigned for the minerals in the vugs. Towards the center, when the pattern is fully developed, a transition is shown from alunite long, alunite medium, alunite short-sideB and alunite short-sideA. For other vugs and in the vein, the patterns are not complete, either alunite short-sideA or alunite short sideB is not present.

The majority of the unclassified pixels are shown in the central part of the vein. This is the result of an absorption feature around 1942 nm that can be attributed to water content in the alunites. Also, some pixels were classified as montmorillonite but the spectra are mainly noise and probably misclassified.

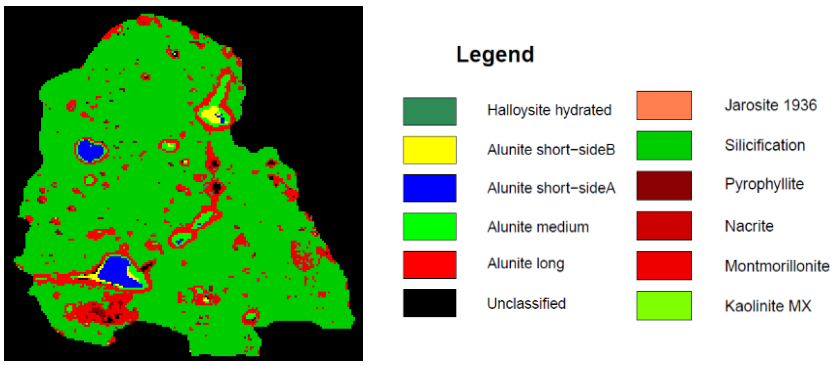

Figure 36. Classified image from *sample260-sideA* by using the Spectral Angle Mapper.

Percentages of the quantification of the SAM statistics for *sample260-sideA* are represented in the plot shown in figure 37 (A). Since the silicification corresponds to 81% of the sample, a zoom in the values is shown in figure 37 (B).

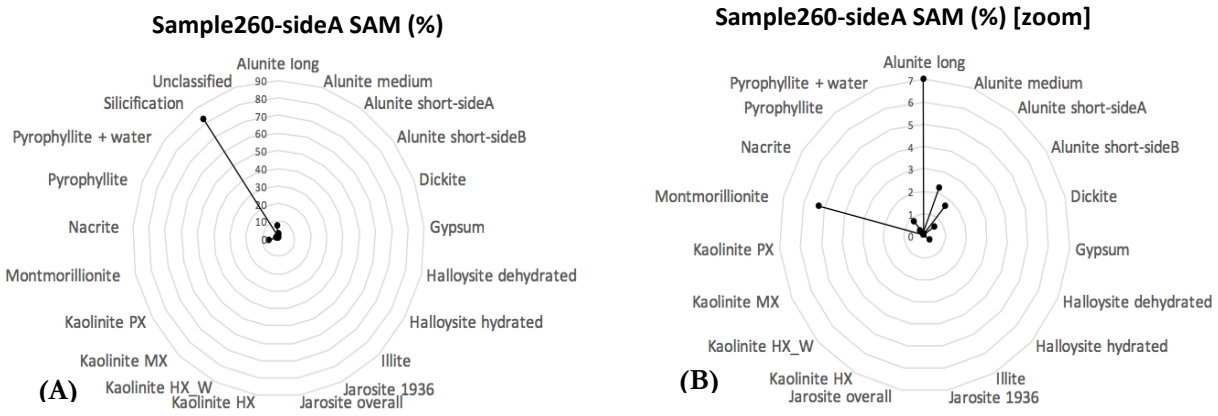

Figure 37. Abundance quantification of the most dominant minerals in *sample260-sideA* based on the SAM algorithm (A) abundances of all the minerals (B) Zoom to the center showing the less abundant minerals.

Kaolin group sample

Resultant classified image of the *sample219* from the kaolin group samples is shown in figure 38 (B). Dickite, pyrophyllite, kaolinite MX, montmorillonite, kaolinite HX, nacrite and halloysite dehydrated are the main minerals that were recognized. However, some pixels classified as pyrophyllite have a spectrum that corresponds to a kaolin group mineral. This misclassification is due to the similarities with the spectrum of the pyrophyllite endmember between the 1464 nm and 2054 nm (figure 38(B)).

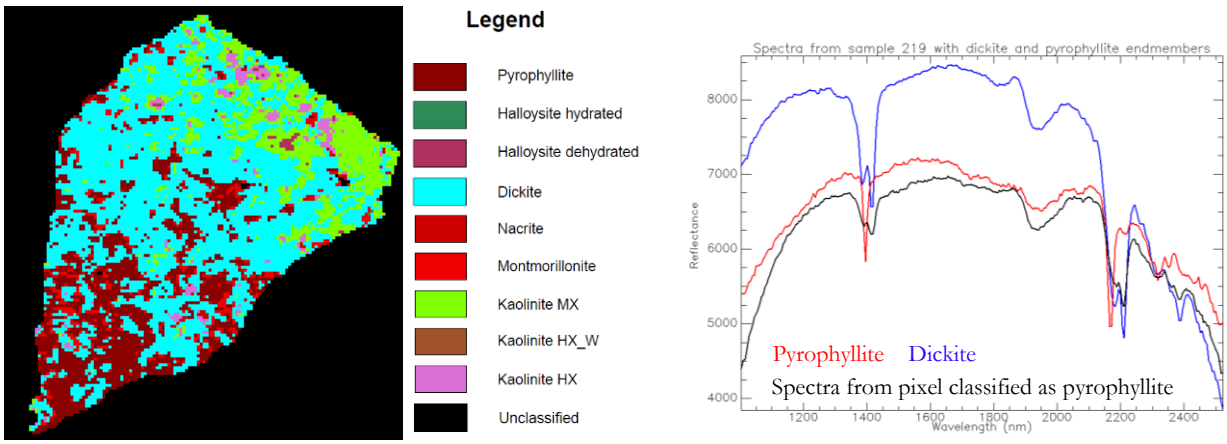

Figure 38. (A) Classified image from *sample219* by using the Spectral Angle Mapper. (B) Spectra from the image classified as pyrophyllite being compared with the endmember of pyrophyllite and dickite.

Quantification of the results is shown in the plot of figure 39. Dickite is the most abundant mineral, followed by a misclassified pyrophyllite, then medium crystalline kaolinite and montmorillonite.

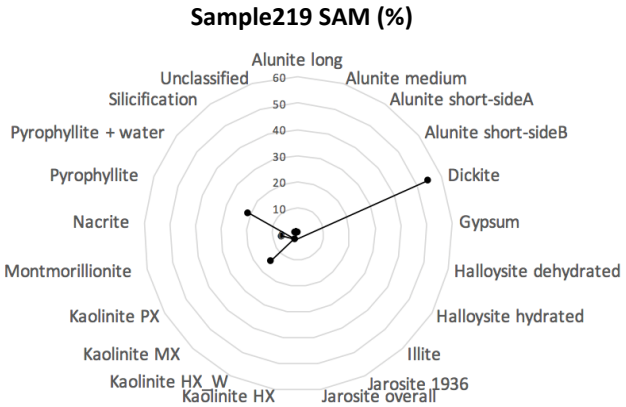

Figure 39. Abundance quantification of the most dominant minerals in *sample219* based on the SAM algorithm.

4.2.6. Spectral unmixing

Results of the Iterative Spectral Mixture Analysis (ISMA) algorithm show fractions of minerals present per pixel in realistic proportions. Because of this, not only the most dominant and abundant minerals per pixel are detected but also less abundant minerals. Examples of the results are presented with *sample260-sideA* and *sample219*. Results for the rest of the samples can be found in appendix 5 and appendix 6.

Alunite sample

Quantification in percentages of the ISMA results for *sample260-sideA* is shown in the plots of figure 40(A) which shows the general results, with 74.64 % of silicification; figure 40 (B) shows a zoom to the center allowing the representation of the rest of the minerals. The results of the ISMA normalized values are shown in figure 40 (C). The zoom excluding the silicification (88.86 %) is shown in figure 40 (D).

Looking at the normalized plots, excluding silicification, the two endmembers of alunite at short wavelengths are the most abundant (alunite short-sideB has 3.24 % and alunite short-sideA has 2.64 %). Followed by alunite at long wavelengths (2.09 %), alunite medium (1.32 %) and pyrophyllite (0.68 %). Less content of montmorillonite (0.47 %), jarosite (0.27 %) and gypsum 0.15 %) are also reported. However, the pixels that were found with fractions of gypsum were analyzed and they appear to be alunite spectra which were misclassified by ISMA. This is an eventuality that appears in other images as well.

Results of ISMA for *sample260-sideA* also show patterns in vugs of the alunite minerals, as can be seen in the colour composites of figure 41 (A). Towards the centre of the vugs alunite minerals transition start from alunite short-sideA in the edges (green colour), followed by alunite long (red colour), alunite short-sideB (blue colours), a mixture of the alunite shorts (cyan) and finally, in the centre of the main vugs alunite short-sideA (green). However, the filling pattern is not fully shown in other vugs. Along the vein, alunite long and alunite short-sideA are recognized. Alunite medium is only shown as part of the vein and the filling of the vugs when the colour composite is stretched, see figure 41 (B) (alunite long in red, alunite short-sideA in green and alunite medium in blue).

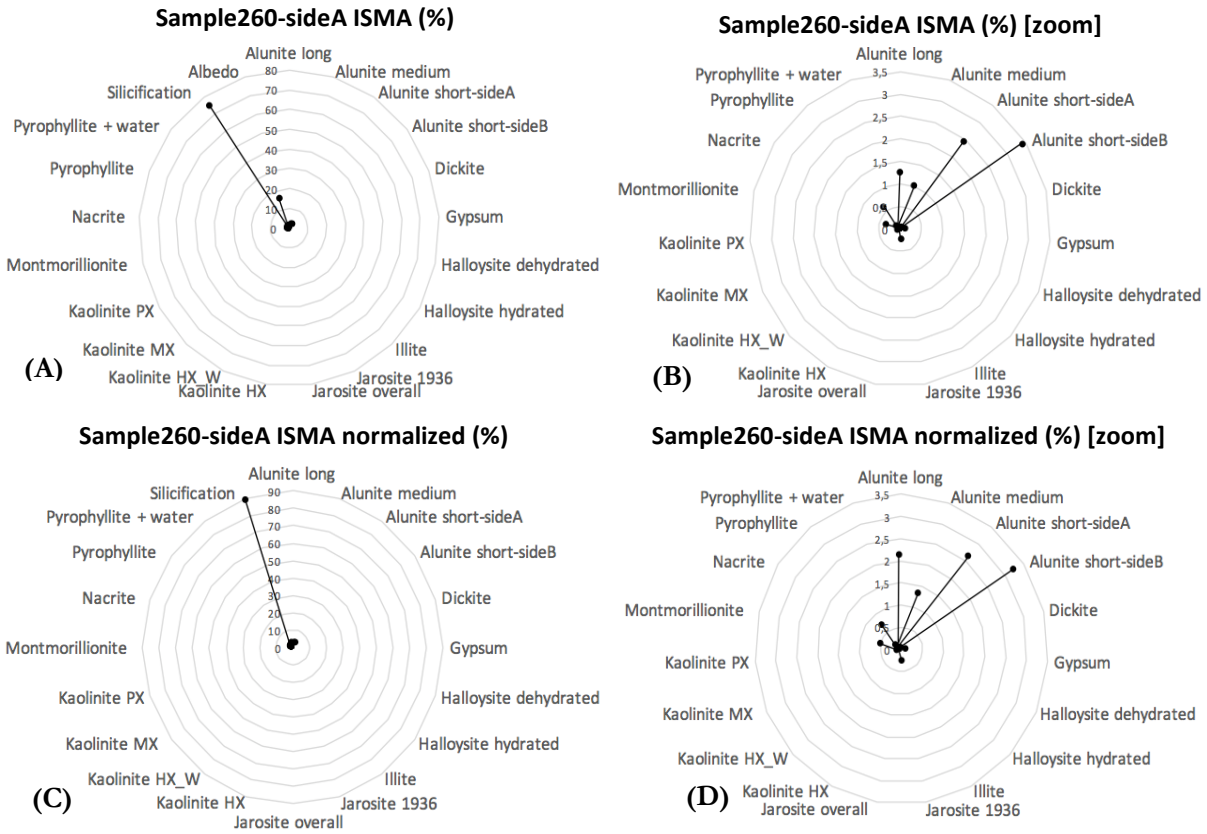

Figure 40. Quantification of the accumulated partial abundances of minerals in *sample260-sideA*. The values are the result of (A) the Iterative Spectral Mixture Analysis (ISMA) (B) Zoom to the less abundant minerals (excluding albedo and silicification) from ISMA (C) Normalized values from the ISMA (D) Zoom to the less abundant minerals from ISMA normalized values.

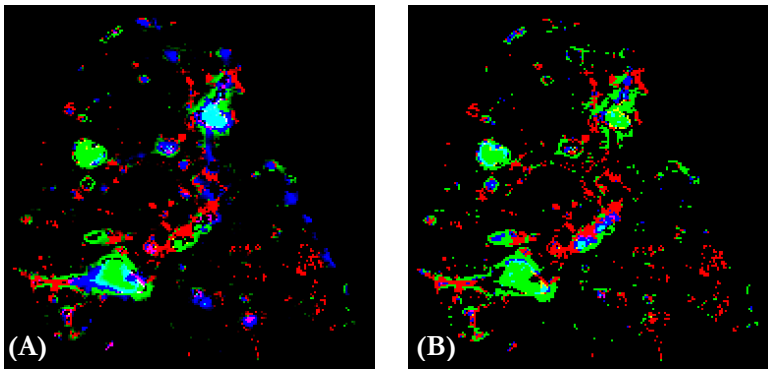

Figure 41. Colour composites of the *sample260-sideA,* showing overprinting patterns of alunite minerals (A) RGB: Alunite long, alunite short-sideA, alunite short-sideB; (B) RGB: Alunite long, alunite short-sideA, alunite medium (image has been stretched for visualization of alunite medium (red colour))

Kaolin group sample

Quantification of the ISMA results for the *sample219* is shown in figure 42 (A). The normalization of these values due to the albedo is shown in figure 42 (B). For this sample, no zoom is required since the complete distribution of the values is already visible. Based on the normalized values, the most abundant mineral is dickite (40.56 %). Pyrophyllite has 35.81 %, medium crystalline kaolinite has 6.85 %, nacrite has 4.56 %. Less abundant minerals are jarosite (0.86 %), highly crystalline kaolinite (0.87 %), montmorillonite (0.68 %) and silicification (0.53 %).

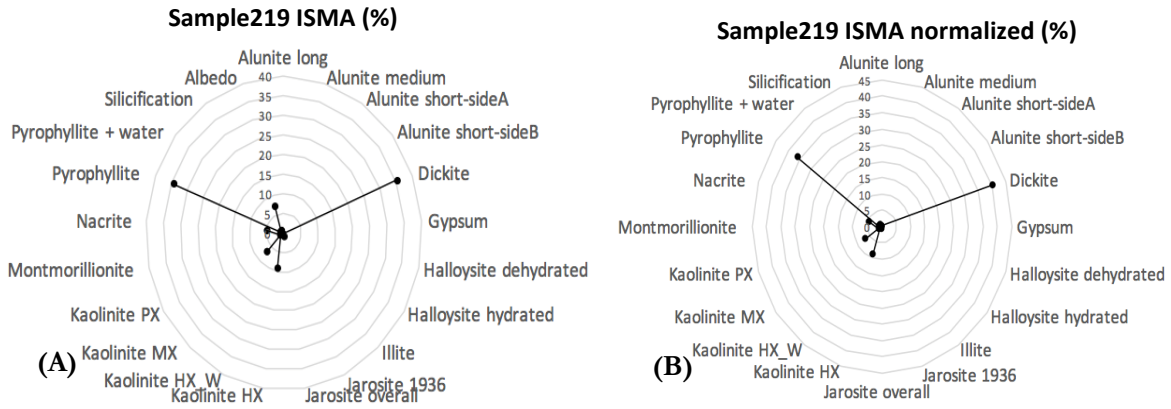

Figure 42. Quantification of the accumulated partial abundances of minerals in *sample219*. The values are the result of (A) the Iterative Spectral Mixture Analysis (ISMA) and (B) the normalization of the ISMA results.

A colour composite of the *sample219* showing the fraction abundances of dickite in red, high crystalline kaolinite in green and medium crystalline kaolinite in blue is shown in figure 43 (A). In figure 43 (B), a colour composite of the *sample219* showing in red the fraction abundance of dickite, in green pyrophyllite and in blue nacrite. Dickite corresponds to the main part of the rock. Kaolinite HX, kaolinite MX, and less nacrite are covering the upper right pixels and it is shown as a pattern, grading from kaolinite HX to kaolinite MX from the dickite to the edge of the sample. Pyrophyllite has been misclassified.

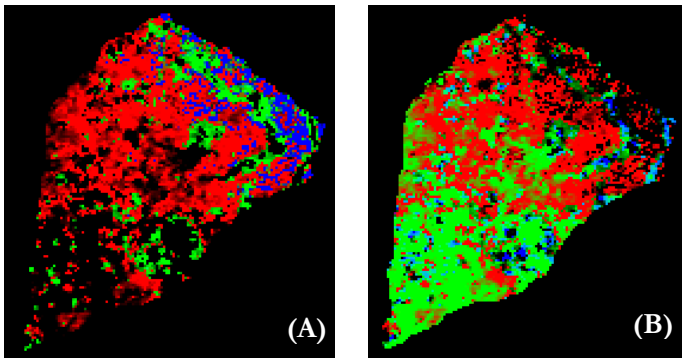

Figure 43. Colour composites of the *sample219*, showing overprinting patterns of kaolin group minerals (A) RGB: dickite, kaolinite HX, kaolinite MX; (B) RGB: dickite, pyrophyllite, nacrite.

As a representation of the mineral abundances, results from the normalization of the accumulation of fraction abundances from ISMA per sample have been presented in the alteration zones previously proposed by Arribas et al. (1995), see figure 44. Alteration zones are organized from the most extreme leaching to the least, from left to right and minerals are organized starting in hypogene (reddish colours) to supergene (bluish colours) from bottom to top. In this way, a pattern of the most dominant minerals is visible. Reddish colours (hypogene minerals) go higher in the most extreme altered zones progressively grading to lighter colours giving space to bluish colours (supergene minerals) that go down in the right bars.

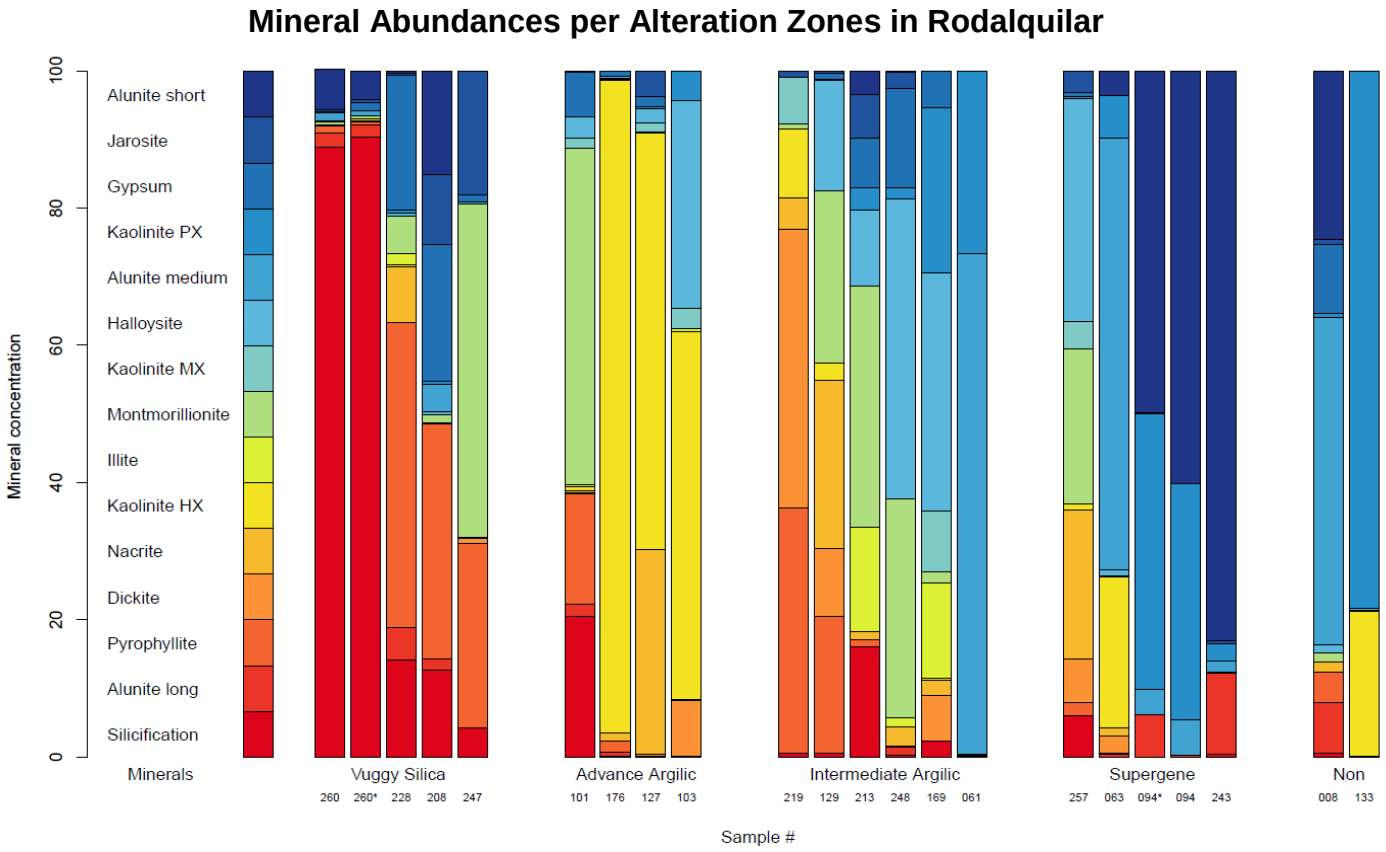

Figure 44. Mineral abundances based on the normalized results of the Iterative Spectral Mixture Analysis (ISMA), per alterations in the Rodalquilar. Samples are organized in each of the alteration zones proposed by Arribas (1995). A pattern is seen that allows to determined based on mineral quantities misclassified samples (*sample257, sample061* and *sample213)* from the alteration map.

For visualization purposes, the ISMA normalized fractions of the endmembers that are most characteristics in alteration zones were used to create summary plots for each of the samples. These endmembers are silicification, alunite long, pyrophyllite, highly crystalline kaolinite, and montmorillonite as hypogene minerals, alunite medium as a transition and alunite short and poorly crystalline kaolinite as supergene minerals. Plots of each of the samples are represented in the alteration map proposed by Arribas et. al (1995) as can be seen in figure 45 for the selected alunite samples, and in figure 46 for the kaolin group samples.

Looking at figure 45 and figure 46 the vuggy silica alteration zone is dominated by silicification, pyrophyllite, alunite short and long, and montmorillonite. In the advance argillic zone, the main minerals are montmorillonite, silicification, kaolinite HX, and pyrophyllite. The intermediate argillic zone is dominated by montmorillonite, alunite medium, and kaolinite PX and in the supergene zone predominates alunite short and medium, kaolinite PX and HX. Moreover, based on the original plots (see appendix 7) mineral associations of alunite short are mainly conformed by poorly crystalline kaolinite, gypsum and jarosite while for the rest of the alunites (alunite short, alunite medium alunite long) they are spatially associated with silicification, pyrophyllite, highly crystalline kaolinite, nacrite and dickite. However, alunite medium has been found associated with montmorillonite, kaolinite medium crystalline and poorly crystalline, with dickite and nacrite as well.

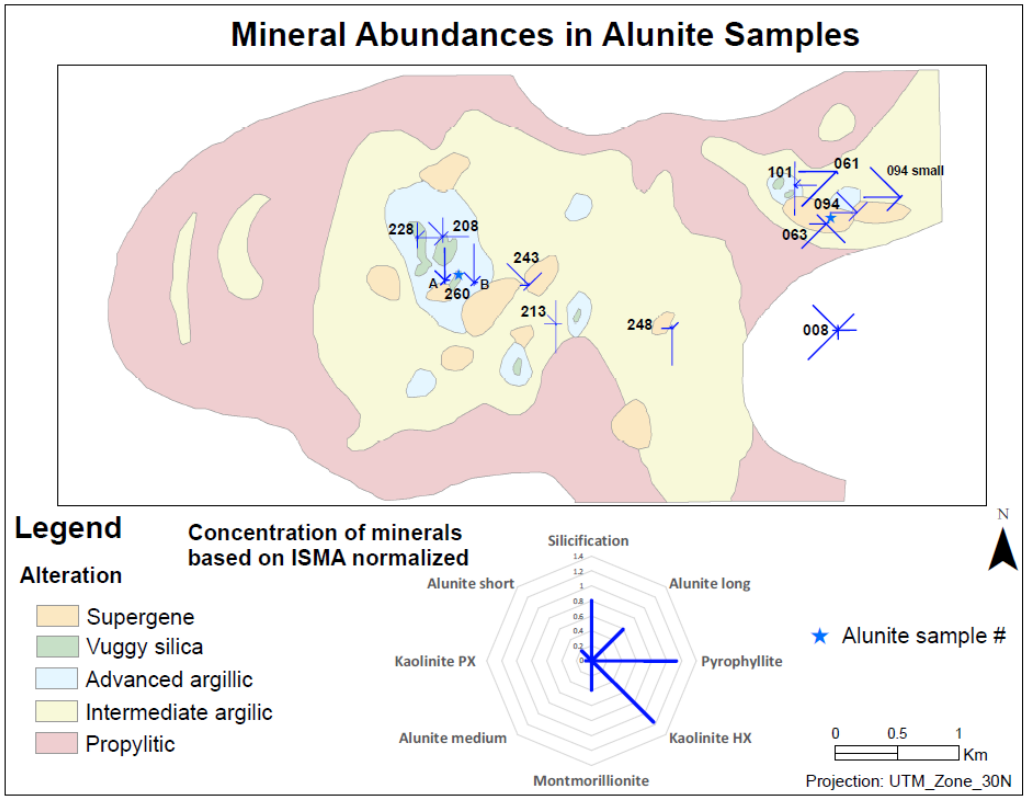

Figure 45. ISMA Normalized average composition of the 8 main endmembers minerals from alteration zones for the selected alunite samples.

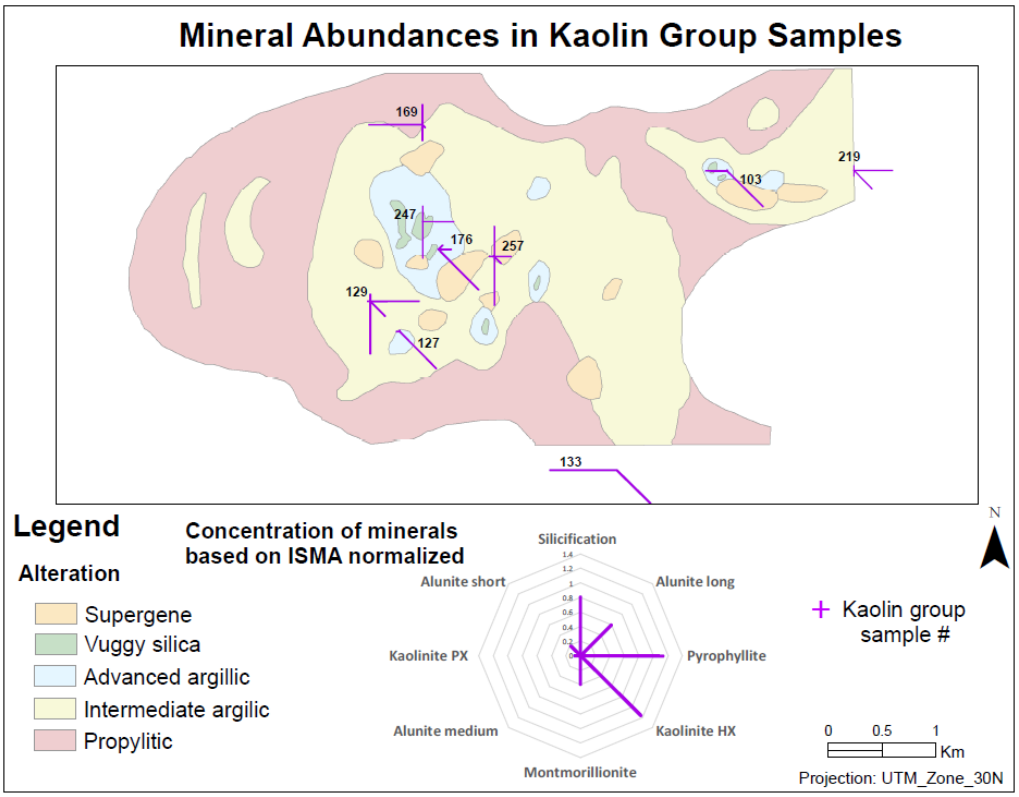

Figure 46. ISMA Normalized average composition of the 8 main endmembers minerals from alteration zones for the selected kaolin group samples.

4.3. Geochemical analysis

4.3.1. Inductively Coupled Plasma analysis

Results from the Inductively Coupled Plasma/Optical Emission Spectrometry for the most interesting elements are shown in Table 3.

Table 3. Chemical concentration of the most interesting elements in supergene and hypogene alunite samples.

(μg/g)	Supergene		Hypogene		
	Sample243 - A	Sample243 - B	Sample260 - A	Sample260 - B	Sample260 - C
Na	13	13	3402.33	3114.45	2982.09
K	$120*10^3$	$105*10^3$	$50*10^3$	$47*10^3$	$48*10^3$
Sr	97.33	89.60	533.79	696.55	737.18
Fe	$11*10^3$	$10*10^3$	$21*10^3$	$21*10^3$	$21*10^3$
Y	1.03	0.77	3.31	2.77	3.34
Zr	<0.26	<0.26	<0.26	<0.26	0.83
Na/K	<0.01	<0.01	0.07	0.07	0.06

Supergene sample (*sample243)* shows high values for the concentration of K and values below the detection limit (<13 μg/g) for the concentration of Na. Therefore, the Na/K ratio is very low. Regarding the hypogene sample (*sample260)*, the concentration of Na is higher and the concentration of K is lower than in the supergene sample but not low. Na/K ratios in the hypogene sample are characteristically high and can reach up to 0.4 (Arribas et al., 1995) Moreover, higher concentration of Sr, high concentrations are found in our hypogene sample and low values in the supergene sample.

The results of the concentration of Y and Zr, values are particularly small. Zr concentrations are mainly below detection limit (<0.26 μg/g). Y concentrations are high in the hypogene samples while small in the supergene samples.

4.3.2. Thermogravimetric analysis

The thermogravimetric analysis of the alunite samples *260* and *243* are shown in figure 47. In colour magenta are the curves for the *sample260* (hypogene sample) and in black the ones representing *sample243* (supergene samples). In the upper part of the graph are the TGA curves showing the accumulated weight losses that have occurred and at the bottom of the graph are the derivative of the weight loss curves (DTG).

Two weight loss processes occurred in these samples: dehydroxylation and desulphation. The dehydroxylation represents the loss of the hydroxyl from the alunite structure while the desulphation represents the loss of sulphate.

The results show that these processes occurred at different temperatures in the two samples. In the supergene sample, the hydroxyl loss was at 540 ºC while in the hypogene this loss was at 570 ºC. Moreover, the weight loss in the supergene sample was about 14% while 12% in the hypogene, indicating that the supergene sample had more hydroxyl groups that were less resistive to being released in the TGA. Regarding the desulphation, this process occurs at lower temperatures in *sample260* (hypogene) than in *sample243* (supergene). For the hypogene sample, the loss of sulphate occurs at 735 ºC while in the supergene sample at 760 ºC. As with hydroxylation, the weight loss in desulphation was higher in the supergene sample than in the hypogene sample, around 19% and 25%, respectively, indicating that the supergene sample had more sulphates that were more resistive to being released in the TGA.

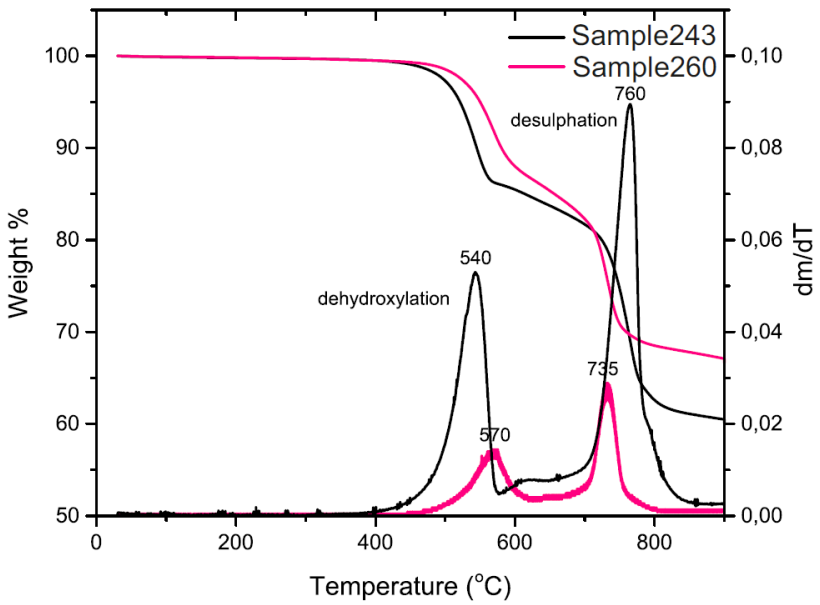

Figure 47. Thermogravimetric and differential thermogravimetric analysis of sample260 and sample243.

5. DISCUSSION

In this research, a SWIR laboratory imaging spectrometer has been used. This results in a full SWIR-range spectrum for each pixel. Even though a dark current and white reference correction were used for the images, remaining problems with the calibration of some detectors still lead to striping in the image or missing data. The applied pre-processing solved most of the issues and allowed for a proper representation and data processing. However, the process is time-consuming and sensitive to aggressive thresholds, which can lead to too much averaging and data loss.

For the analysis of the images, three algorithms were used (see appendix 8). First, the Wavelengths Mapping algorithm was applied which provides a handy and fast tool for the identification of minerals, because only a Wavelength of Minimum map and a selection of wavelength range are required as input settings. However, a disadvantage was encountered when using this algorithm, it only looks at the deepest absorption feature which makes impossible to differentiate minerals with similar absorption features wavelengths.

The SAM algorithm is fast and easy to apply and provides a classification with the most dominant minerals for each pixel of the image. Hence, information on secondary minerals is lost. As input requirements, a threshold for the maximum matching angles and an endmember collection are needed. Thus, the quality of the classification is extremely dependant on the selected threshold, the quality of the endmember collection and the purity of the spectral signature of the endmembers. To illustrate, the classified image of *sample061* in which the constant 0.1 radians threshold, used for the 22 images, was too aggressive because most of the pixel spectra were mixtures. Therefore, 95 % of the image was unclassified (see appendix 3).

The third algorithm used was the Iterative Spectral Mixture Analysis (ISMA). It gives the abundances in fractions per pixel. As the SAM, the ISMA requires an endmember collection, thresholds values for the number of endmembers retained per pixel, and for the number of iterations. However, for the ISMA when the endmembers have spectral similarities, such as the alunite endmembers in this research, the algorithm is susceptible to mismatching. This is the case of *sample260-sideA* (see section 4.2.6.) in which some pixels were detected having a high content of gypsum even though the spectra are of alunite minerals and no sign of gypsum could be detected. The problem may be caused by alunite pixels that were spectrally more extreme than the alunite endmembers. Therefore, gypsum was used to spectrally compensate for that.

Regarding the performance of the three algorithms, Wavelength Mapping is useful when mapping minerals is the aim and the user has spectral knowledge that allows the selection of the wavelength ranges considering the minerals present in the image. Otherwise, not all the minerals can be found. Another drawback is that several maps are needed to see all the minerals of a rock sample, hence a proper interpretation is time-consuming. In the case of the Spectral Angle Mapper (SAM), results are summarized in one image. That makes the SAM be useful when a general interpretation of the most dominant minerals per pixel needs to be done fast. Nevertheless, the purer the image pixels the better the results are. Concerning the Iterative Spectral Mixture Analysis (ISMA), mineral fractions are shown in different bands of one image allowing to observe the results faster than with the wavelength mapping but slower than with the SAM. However, an albedo endmember is added during the unmixing and this complicates the interpretation of the ISMA results. The results were normalized such that all endmember fractions add up to 100% without the albedo endmember. In addition to this, a common disadvantage of SAM and ISMA is the dependency on the endmember collection that can have major effects on the results. As an evidence of the influence of the endmembers in the SAM and ISMA algorithms, which considers the whole spectrum, results of *sample260-sideA* show zonation in alunite minerals that are filling the vugs in the results of the SAM and ISMA but not

in the Wavelength map used for this differentiation, in which the wavelength range is between 1460 – 1495 nm. This is due to a change in the spectral shape of the alunites spectra (which is tilted) from the periphery to the central parts of the vugs filling and not because of a shift in the position of the 1480 nm feature (controlled by the alunite composition). Hence, the wavelength maps do not show alunite variations in the vugs of *sample260-sideA*.

For this research, each of the algorithms, in general, worked well. All the ranges used for the Wavelength maps fulfilled their function or contributes in a different way. As it is the case of the second range of the wavelength maps used for the alunite samples (1460 – 1495 nm), which allows to differentiate between alunite and jarosite minerals that were found, instead of differentiating amongst alunite minerals with compositional changes. However, since the main purpose of the wavelength maps was to obtain an idea of the minerals present in the rock samples, the most useful range was the wide range, from 1200 – 2400 nm, allowing the recognition of most of the minerals. Regarding SAM and ISMA, overprinting patterns between different minerals such as, different alunites (*sample260),* alunites and kaolinite (*sample063),* alunite and jarosite (*sample213* and *sample208)* are easily visible. However, ISMA allows a better comprehension since less abundant minerals are also shown. For the quantification of the minerals with SAM and ISMA, both algorithms have similar results but ISMA results are more detailed (they contain the aggregation of the partial fractions of the minerals, including the less abundant).

The endmember collection in this research was built by handpicking the less mixed spectra from the Wavelengths maps after identifying the minerals that are present in the rock samples. This method facilitates further interpretation of the images since most of the minerals occurring in the sample will be seen before the rest of the analyses are carried out. However, consequences of handpicking the endmembers include that for some minerals, the different spectra selected have not the most extreme characteristics of the minerals. Therefore, inaccurate minerals fractions and misclassifications resulted from the ISMA and SAM. As is in the case of *sample260* explained before, where the closest match of some image spectrum was incorrectly done with gypsum instead of with one of the alunite endmembers. For these reasons, an automatic method for the endmembers extraction, in which the output is a set of spectra from the images that have the best match with any of the spectral libraries already created (Clark et al., 2007; Pontual et al., 1997d), might guarantee the selection of the most extreme spectra present in the images. However, even if it does not require the evaluation of the image in advance, an interpretation of the images and comparison of the endmembers to the existing spectral libraries (to identify the endmembers by name) must be done.

By using the wavelength maps, the spectral differences between hypogene and supergene alunite were evaluated. As it is known from the literature, supergene alunite in the Rodalquilar is always K rich, while hypogene can be either K rich or Na rich (Arribas et al., 1995). In this context, the fact that hypogene alunite can be either K rich or Na rich makes more difficult to spectrally assign an alunite to one of the two groups. Moreover, it is also known from the literature that K rich alunite is spectrally identified with diagnostic absorption features at short wavelengths, around 1430 nm, and 1478 nm, while Na alunites at long wavelengths, 1437 nm and 1493 nm (Clark et al., 2007). Looking at the ASD spectra and the results of the geochemical analysis the alunite with the shortest wavelength (*sample243;*1477 nm) has very low Na content and it is K rich, while *sample260* with slightly higher Na content than the supergene sample, it is still K rich and slightly moves the 1480 nm feature to longer wavelengths (1481nm; see figure 11 ASD spectra). No Na rich alunite samples have been geochemically analyzed yet. However, the results of the analysis in the images confirm that these differences in the wavelength positions seen with the ASD spectra are due to a small content of jarosite in the supergene sample (*sample243*) that is not being detected with the ASD point measurements.

Regarding the geochemical analyses that were done in the supergene and hypogene samples, they show that certainly there are chemical differences between the two alunite samples. ICP/OES result shows low concentrations of Na, Sr, Y and Zr, and high concentrations of K for the supergene sample, while in the hypogene sample concentrations of Na, Y and Sr are slightly higher and it is K rich as well. In contrast, high concentrations of Y are reported in the literature for supergene alunites and low concentrations in hypogene samples (Arribas et al., 1995) (see Table 1). This difference in the Y concentration is attributed to the fact that Y concentrations deplete with increasing alteration which is weaker in pyrophyllite altered rocks than in alunite minerals (Hikov, 2011). Content of pyrophyllite have been spectrally seen in the hypogene sample that was used for the geochemical analysis (*sample260)*, however, care was taken when preparing the sample for the analysis to avoid the contamination of the rest of the minerals of the rock in the alunite powder. Concerning Zr concentrations in our analysis, they are mainly below the detection limit (<0.26 μg/g) and more material would be required to get reliable and quantifiable results.

The TGA analysis identified differences in chemical structure between the hypogene and supergene alunite samples. It shows that for the thermal dehydroxylation of the hypogene sample higher temperatures are needed than for the supergene sample. This can be attributed to the fact that hypogene minerals, in general, have a more stable structure and are created at higher temperatures than supergene minerals (White & Hedenquist, 1995). Moreover, the weight loss is less in the hypogene samples which can also be attributed to the stable structure with less hydroxyl groups present. These differences in temperature of the maxima of hydroxylation and desulphation between the two samples are an indication of the differences in chemical accumulations of elements, hence in the bonds amongst molecules. These results, on a very limited number of samples (2), show that there is potential in differentiating supergene and hypogene alunite with geochemical analyses as a validation technique for infrared spectroscopy results in the Rodalquilar.

After evaluating the spectral and chemical results of the hypogene and supergene samples, the position in the wavelength range where alunite composition changes from K rich to Na rich might be more than an exact position, a gradual transition. This is supported by the fact that both spectral signatures have their diagnostic absorption feature (1480 nm) at the same wavelengths and the results of the geochemical analyses show a difference in the K and Na content of both samples, being the Na/K ratio slightly higher for the hypogene sample.

The crystallinity of the kaolinite provides another approach to the differentiation between hypogene from supergene patterns. For the different types of kaolinite that were found, a visual examination of the characteristics of the spectrum was carried out since that is the most important procedure when spectral signatures want to be used (Pontual et al., 1997c). This is because crystallinity parameters are highly affected by impurities in the spectra and they must be visually confirmed. However, a further validation of these results with techniques such as XRD would provide the best combination for kaolinite crystallinity determinations. In general, for this research, the visual analysis for the determination of the kaolinite crystallinity worked well. However, spectra of the kaolin group minerals have similar characteristics that increase the chance of misidentification.

On one hand, to rapidly visualize partial abundance values in alunite and kaolin group samples only the most relevant minerals were plotted, see figure 45 for alunite samples and figure 46 for kaolin group samples. However, in cases such as the kaolin group *sample219* it appears to be pyrophyllite the main mineral but in fact, it is dickite, as can be found in appendix 7. Hence, it is always better to refer to the original plots. The plots with the most relevant minerals are shown on top of the alteration map taken from the literature (Arribas et al., 1995) and as it is known from literature gold accumulations in the Rodalquilar are in the

eastern limit of the inner caldera, Lomilla caldera (see figure 1(B)) and are associated with silicification and hypogene alunite minerals. In this context, results from the research agree and plots with the quantification results of the samples near the eastern edge of Lomilla caldera show higher content of silicification and alunite minerals (see figure 45). On the other hand, figure 44 shows the results in a different way: this bar graph uses all the minerals per sample, hypogene minerals at the bottom and supergene minerals at the top; and the samples are grouped based on the location of them in the alteration map proposed by Arribas (1995). This graph allows seeing a pattern where mineral quantities of different rock samples can be used to assign rocks to their corresponding alteration zone. By taking this into account, it is possible to see how some of the samples in figure 44 (*sample257, sample061 and sample213)* do not fit into the pattern shown by the bars due to different mineral quantities. To illustrate, the amount of nacrite and montmorillonite in *sample257* evidence that the sample do not correspond to the supergene alteration zone and that the intermediate argillic will be more suitable.

This research used data from the epithermal system in the Rodalquilar caldera complex. Rock samples are from the vuggy silica, advance argillic and intermediate argillic alteration zones based on the alteration zones proposed by Arribas et. al (1995). Because samples were selected based on preliminary ASD spectral results of alunite and kaolin group content, no sample from the propylitic zone was included in the selected samples for the research. For further studies, not only spectral parameters but also geographic location of the samples should be considered. The sericitic zone in the Rodalquilar system is not sampled as it is only known to the surface from drilling.

The methodology carried out in this research can be also executed in a different alteration system where the exposure of the systems makes possible the collection of either rock samples or drill cores to facilitate the later acquisition of the images. Moreover, knowledge about the minerals associated with the important ore accumulations (such as gold) must be known from literature to be able to focus the method in these minerals. Besides, the presence of similar minerals overprinting each other will allow differentiating between the hypogene and supergene version of the minerals making the targeting of prospective areas feasible.

As a final point, even a dataset of ASD FieldSpec Spectrometer point measurements was already available and completed in the first step of this research. The advantages of using high spatial resolution images over point measurements is not only that the overprinting patterns are recognized in the images (such as in *sample213* and *sample260)* but also that they allow an estimation of all the minerals present in the samples and how much of each are in there, while with the point measurements the recognition and quantification depends on the point that is being measured excluding minerals from the rest of the sample. To illustrate, ISMA results from the image of *sample260-sideA* shows not only alunite and silicification but also pyrophyllite and mixtures of pyrophyllite with alunite, while ASD measurements only show spectra of alunite minerals.

6. CONCLUSIONS AND RECOMMENDATIONS

This spectral study of high spatial resolution hyperspectral images of rock samples from the Rodalquilar epithermal system, and validation with geochemical analyses lead to the following conclusions:

- Our geochemical results of the two samples that were suitable for geochemical analysis and chosen based on texture (one hypogene and one supergene sample) show that there are differences in the chemical structure between the samples (figure 47) and that the chemical composition of both is K rich (table 3). Moreover, both samples show with our SPECIM images the diagnostic absorption feature of the alunite minerals at 1481 nm (the samples that truly have the position of the 1480 diagnostic absorption feature of alunite minerals at longer wavelengths are not suitable for geochemical analysis). Additionally, both supergene and hypogene alunite in the study area can be K rich. With these results and looking at the first objective, firstly, we could not spectrally differentiate hypogene and supergene alunite minerals; secondly, we confirm that the position of the alunite feature at shorter wavelengths certainly corresponds to K rich alunite; and finally, there is in fact potential in using TGA for differentiation of the two stages of alunite minerals (hypogene and supergene) in the Rodalquilar which should be tested on a larger dataset.

- In our results, wavelength position of the 1480 diagnostic absorption feature of the alunite minerals in the Rodalquilar vary from shorter (1477 nm) to longer wavelengths (1481 nm). However, some of the variations that we see in our results from the ASD spectra (figure 16) are caused by mixtures of alunite with small amounts of pyrophyllite and jarosite (shifts to shorter wavelengths) and illite and halloysite (shifts to longer wavelengths). These mixtures are not identified with our ASD spectra but can be seen with our results from the SPECIM images. In this way, there is in fact potential to differentiate varying types of alunite minerals in the Rodalquilar by using spectroscopy.

- In this research, spectra of kaolinite minerals with different crystallinities (highly crystalline, medium and poorly crystalline (see figure 35)) were visually identified, as well as spectra of the rest of the kaolin group minerals (halloysite, dickite, nacrite; see figure 33(A)) and were used in the endmember library. These results allow for unmixing and classification into minerals of different stages (achieving the second objective of this research) which has proved helpful when differentiating the hypogene and supergene influences on rock samples.

- In our images, late stage veinlets of alunite and jarosite mixtures cutting throughout rocks show alunite with the diagnostic absorption feature at short wavelengths. These textures helped to identify late stage alunite overprinting and associated minerals (jarosite). In this way, and tackling the third specific objective we concluded that overprinting patterns are useful and can be used in the future for identifying minerals of different stages.

- Results of our quantification of mineral abundances were firstly represented in spider graphs that we created with the hypogene minerals on the right side and the supergene minerals on the left side. These spider graphs were then plotted on the spatial domain (existing alteration map by Arribas et al. (1995)) allowing a quick overview of the alteration assemblages (figure 45 and figure 46). With these results, specific objective 4 was reached. In the future, this technique can be applied for a larger number of samples helping to re-evaluate the boundaries of the alteration zoning.

- Furthermore, for our quantification of the minerals composition we also developed a bar graph that quantitatively separated the hypogene from the supergene minerals (hypogene minerals at the bottom and supergene minerals at the top; see figure 44). To group the samples, the alteration map by Arribas et al. (1995) was used to assign them to the different alteration zones. In this way, a sequence in the concentrations is seen. However, we notice that some of the samples might be misclassified in the alteration map and do not fit into the pattern that we see with our bar graph (e.g.: *sample257)*. In the future two things are needed, firstly a larger number of samples to complete this bar graph and, secondly, a decision tree that quantifies the mineral proportions. If results of mineral quantities of more samples are added, the pattern in our bar graph will become more apparent and possible wrong classifications, because of errors in the existing map, can be detected allowing to define thresholds that then can be used to classify future samples to an alteration zone and then redraw the alteration map.

- From the results of the three algorithms used in this research, the Wavelength Maps gives a fast overview of the minerals patterns in the rocks. The SAM gives a hard classification of the most abundant minerals, and the ISMA unmixed the spectra and gives also the partial fraction quantities of the less abundant minerals. Occasionally, unmixing has led to incorrect quantifications of minerals (e.g. gypsum) but the advantages outweigh the disadvantages of using an unmixing algorithm. In this context, for the quantification of the minerals required to make the final graphs of this research (figure 44, figure 45 and figure 46), it is highly recommended to use an unmixing algorithm, as ISMA. Otherwise, the quantities of the minerals that only occurred in subpixel fractions are misrepresented.

- The use of high spatial resolution hyperspectral images has several advantages over using ASD point measurements: A. quantification of minor mineral constitutes is more reliable since they can be undetected with the ASD spectra; B. recognition of potential sources for determination of shifts in wavelength positions caused by mineral mixtures can be detected since the pixel size of the images is approaching the grain size; C. spatial patterns of minerals through the entire rock are possible to be seen in the images.

The previous conclusions of the research lead to the following recommendations:

- To establish the spectral transition between K rich alunite and Na rich alunite a study linking spectroscopy with geochemistry focusing on just supergene and hypogene alunite is needed. Special attention must be taken with the collection of rock samples to ensure the presence of representative and purer samples.

- An automatic algorithm applied for the extraction of the endmembers will offer an advantage of collecting the purest and more different spectra of the minerals giving the option to reduce the omissions of minerals spectra with extreme behaviors.

LIST OF REFERENCE

Armstrong, D. C. (1995). Acid Sulphate Alteration in a Magmatic-Hydrothermal Environment, Barton Peninsula, King George Island, Antarctica. *Mineralogical Magazine*, *59*(396), 429–441. http://doi.org/10.1180/minmag.1995.059.396.05

Arribas, A., Cunningham, C. G., Mckee, E. H., Rytuba, J. J., Richard, T., Michael, W., & Masahiro, A. (1995). Compilation of sample preparation and analytical methods and results of chemical, isotopic, and fluid analyses, Rodalquilar gold-alunite deposits, Spain. *U.S. Geological Survey. Open-File Report*, *95–221*, 33.

Arribas, A., Cunningham, C., Rytuba, J., Rye, R., Kelly, W., Podwysocki, M., Tosdal, R. (1995). Geology, Geochronology, Fluid Inclusions, and Isotope Geochemistry of the Rodalquilar Gold Alunite Deposit, Spain. *Economic Geology*, *90*, 795–822.

Bakker, W. (2012). HyyPy3 Software. (https://www.itc.nl/personal/bakker/hyppy.html) (accessed October 2016)

Bakker, W. (2016). *HypPy User Manual.* (https://www.itc.nl/personal/bakker/hyppy.html) (accessed October 2016)

Bedini, E., van der Meer, F., & van Ruitenbeek, F. (2009). Use of HyMap imaging spectrometer data to map mineralogy in the Rodalquilar caldera, southeast Spain. *International Journal of Remote Sensing*, *30*(2), 327–348. http://doi.org/10.1080/01431160802282854

Brindley, G. W., Kao, C., Harrison, J. L., Lipsicas, M., & Raythatha, R. (1986). Relation between Structural Disorder and Other Characteristics of Kaolinites and Dickites. *Clays and Clay Minerals*, *34*(3), 239–249. http://doi.org/10.1346/CCMN.1986.0340303

Calvin, W. M., & Pace, E. L. (2016). Mapping alteration in geothermal drill core using a field portable spectroradiometer. *Geothermics*, *61*, 12–23. http://doi.org/10.1016/j.geothermics.2016.01.005

Chororoka, K. (2012). Geochemical and spectral characterzation of hydrothermal alteration facies at the epithermal gold mineralization at Rodalquilar, Spain.

Clark, R. N., King, T. V. V., Klejwa, M., Swayze, G. A., & Vergo, N. (1990). High spectral resolution reflectance spectrsocopy of minerals. *Journal of Geophysical Research*, *95*(B8).

Clark, R. N., Wise, R., Livo, K. E., Hoefen, T. M., Kokaly, R. F., & Sutley, S. J. (2007). USGS Digital Spectral Library. Retrieved August 16, 2016, from http://speclab.cr.usgs.gov/spectral.lib06/ds231/datatable.html

Corbett, G. (2012). Structural Controls to , and Exploration for , Epithermal Au-Ag Deposits Classification of Epithermal Deposits. *Structual Geology and Resources*, (figure 1), 43–47.

Cruz, M. D. R. (1989). Genesis and evolution of the kaolin-group minerals during the diagenesis and the beginning of metamorphism. *Geologia.Ujaen.Es*, 41–52. Retrieved from http://geologia.ujaen.es/sem2007/english/separatas/SEMINARIOS_SEM_3_41.pdf

Cunningham, C. ., Arribas Jr., A., Rytuba, J. J., & Arribas, A. (1990). Mineralized and unmineralized calderas in Spain; Part I, evolution of the Los Frailes Caldera. *Mineralium Deposita*, *25*(1), 21–28. http://doi.org/10.1007/BF00205247

Dill, H. G., Bosse, H.-R., Henning, K.-H., Fricke, a., & Ahrendt, H. (1997). Mineralogical and chemical variations in hypogene and supergene kaolin deposits in a mobile fold belt the Central Andes of northwestern Peru. *Mineralium Deposita*, *32*(2), 149–163. http://doi.org/10.1007/s001260050081

Ercan, H., Ece, O., Schroeder, P., & Karacik, Z. (2016). Differentiating styles of alteration within kaolin-alunite hydrothermal deposits of Canakkale, NW Turkey. *Clays and Clay Minerals*, *64*(3), 245–274. http://doi.org/10.1346/CCMN.2016.0640305

EXELIS. (2013). ENVI Classic Tutorial : Advanced Hyperspectral Analysis. *Visual Information Solutions*.

Fagbohun, B. J. (2015). Combining Dominant Spectral Features in Airbone SWIR and TIR Imagery For Mineralogical Mapping. MSc Thesis, University of Twente, Faculty of Geo-Information and Earth Observation (ITC).

Frost, R. L., & Wain, D. (2008). A thermogravimetric and infrared emission spectroscopic study of alunite. *Journal of Thermal Analysis and Calorimetry*, *91*(1), 267–274. http://doi.org/10.1007/s10973-006-7979-2

Garcia, L. A. G. (2013). Crystallinity variations of smectite-illite and kaolin hydrothermal alteration minerals by using SWIR spectroscopy. A study of the Rodalquilar Au-deposit, SE Spain., *60*, 84.

Gifkins, C., Herrman, W., & Large, R. (2005). *Altered Volcanic Rocks - A guide to description and interpretation*. New York: Centre Ore Depos Res, University Tasmania, Hobart.

Gonzalez P, O. A. (2009). Capitulo V. Generalidades. Características principales de los depósitos epitermales en el noroeste de México, un análisis y comparación. University of Sonora. Mexico.

Hauff, P. L., Kruse, F. A., & Thiry, M. (1990). Characterization of interstratified kaolinite/smectite clays using infrared reflectance spectroscopy (1.2 - 2.5). *Chemical Geology*, *84*(1–4), 267–270. http://doi.org/10.1016/0009-2541(90)90234-X

Hedenquist, J. W., Arribas R, A., & Gonzalez-Urien, E. (2000). Exploration for Epithermal Gold Deposits. *Reviews in Economic Geology*, *13*(February), 245–277. http://doi.org/07410123

Hou Xiandeng, J. B. T. (2000). Inductively Coupled Plasma–Optical Emission Spectrometry. *Spectroscopy Letters*, *42*(1), 58–61. http://doi.org/10.1080/00387010802375065

Hunt, G. R., & Ashley, R. (1979). Altered rock spectra in the visible and near infrared. *Economic Geology*, *74*(7).

Iordache, M.-D., Bioucas-Dias, J., & Plaza, A. (2011). Unmixing sparse hyperspectral mixtures. *IEEE Transactions on Geoscience and Remote Sensing*, *49*((6)), 2014–2039.

Kyne, R., Hollings, P., Jansen, N. H., & Cooke, D. R. (2013). Supergene and hypogene halloysite in a porphyry-epithermal environment at Cerro La Mina, Chiapas, Mexico. *Economic Geology*, *108*(5), 1147–1161. http://doi.org/10.2113/econgeo.108.5.1147

Lagat, J. (2007). Hydrothermal alteration mineralogy in geothermal fields with case examples from Olkaria domes geothermal field, Kenya. *Short Course II on Surface Exploration for Geothermal*, 1–24. Retrieved from http://www.os.is/gogn/unu-gtp-sc/UNU-GTP-SC-05-10.pdf

Life, P., & Sciences, A. (2004). 3rd Edition Concepts, Instrumentation and Techniques in Inductively Coupled Plasma Optical Emission Spectrometry. Charles B. Boss and Kenneth J. Fredeen.

Lopez-Ruiz, J., & Rodriguez-Badiola, E. (1980). La región volcánica neógena del SE de España.pdf. *Estudios Geologicos*.

Morishita, Y., & Nakano, T. (2008). Role of basement in epithermal deposits: The Kushikino and Hishikari gold deposits, southwestern Japan. *Ore Geology Reviews*, *34*(4), 597–609. http://doi.org/10.1016/j.oregeorev.2008.09.009

Oluwadebi, A. G. (2015). The Significance of Crystallinity in Hydrothermal Alteration Mapping : A Case Study of Alem Tena Area of Main Ethiopia Rift , Ethiopia, *3*(4), 12–17.

Panteleyev, A. (2005). Epithermal Au-Ag-Cu : high sulphidation. *British Columbia Geological Survey*, 1–4.

Pirajno, F. (2015). A classification of mineral systems, overviews of plate tectonic margins and examples of ore deposits associated with convergent margins. *Gondwana Research*, *33*, 44–62. http://doi.org/10.1016/j.gr.2015.08.013

Plancon, A., Giese, R. F., & Snyder, R. (1988). The Hinckley Index for Kaolinites. *Clay Minerals*, *1*(23), 249–260. http://doi.org/10.1017/CBO9781107415324.004

Pontual, S., Merry, N., & Gamson, P. (1997a). Epithermal Alteration Systems. *AusSpec International Pty.*, *Vol 4*.

Pontual, S., Merry, N., & Gamson, P. (1997b). Geologically-based Spectral Analysis Guides for Mineral Exploration. Near Surface Weathering Environments. *AusSpec International Pty.*, *Vol 5*, 44.

Pontual, S., Merry, N., & Gamson, P. (1997c). Regolith logging. *AusSpec International Pty.*, *8*, 46.

Pontual, S., Merry, N., & Gamson, P. (1997d). Spectral Interpretation Field Manual. *AusSpec International Pty.*, *1*, 92.

Prost, G. L. (2013). Remote Sensing for Geoscientists. Image Analysis and Integration. (CRC Press). Boca raton: CRC Press. Taylor and Francis Group.

Prost, R., Dameme, A., Huard, E., Driard, J., & Leydecker, J. P. (1989). Infrared study of structural OH in kaolinite, dickite, nacrite, and poorly crystalline kaolinite at 5 to 600 K. *Clays and Clay Minerals*, *37*(5), 464–468. http://doi.org/10.1346/CCMN.1989.0370511

Rakovan, J. (2003). Hypogene and Supergene. *Rock & Minerals*, *78*, 419.

Rogge, D. M., Rivard, B., Jinkai, Z., & Jilu, F. (2006). Iterative spectral unmixing for optimizing per-pixel endmember sets. *IEEE Transactions on Geoscience and Remote Sensing*, *44*(12), 3725–3735. http://doi.org/10.1109/TGRS.2006.881123

Rosenberg, M. D., Bignall, G., & Rae, A. J. (2009). The geological framework of the Wairakei-Tauhara Geothermal System, New Zealand. *Geothermics*, *38*(1), 72–84. http://doi.org/10.1016/j.geothermics.2009.01.001

Rytuba, J. J., Arribas, A., Cunningham, C. G., McKee, E. H., Podwysocki, M. H., Smith, J. G., … Arribas, A. (1990). Mineralized and unmineralized calderas in Spain; Part II, evolution of the Rodalquilar caldera complex and associated gold-alunite deposits. *Mineralium Deposita*, *25*(1), 29–35. http://doi.org/10.1007/BF00205247

Segalst, T. V. (1997). Ore materials : Primary and secondary mineralofy of ore deposits. *Short Course: Environmental Geochemistry of Ore Deposits and Mining Activities. Univeristy of Oslo.*, (May), 1–8.

Thompson, A. J. B., & Thompson, A. J. H. (1996). *Atlas of Alteration. A field and petrographic guide to hydrothermal alteration minerals*. Geological Association of Canada, Mineral Deposits Division.

Tobergte, D. R., & Curtis, S. (2013). ISMA How to Use. *Journal of Chemical Information and Modeling*, *53*(9), 1689–1699. http://doi.org/10.1017/CBO9781107415324.004

van der Meer, F. (2004). Analysis of spectral absorption features in hyperspectral imagery. *International Journal of Applied Earth Observation and Geoinformation*, *5*(1), 55–68. http://doi.org/10.1016/j.jag.2003.09.001

Van Ruitenbeek, F. J. A., Bakker, W. H., Van Der Werff, H. M. A., Zegers, T. E., Oosthoek, J. H. P., Omer, Z. A., … Van Der Meer, F. D. (2014). Mapping the wavelength position of deepest absorption features to explore mineral diversity in hyperspectral images. *Planetary and Space Science*, *101*, 108–117. http://doi.org/10.1016/j.pss.2014.06.009

Van Ruitenbeek, F. J. A., Cudahy, T. J., van der Meer, F. D., & Hale, M. (2012). Characterization of the hydrothermal systems associated with Archean VMS-mineralization at Panorama, Western Australia, using hyperspectral, geochemical and geothermometric data. *Ore Geology Reviews*, *45*, 33–46. http://doi.org/10.1016/j.oregeorev.2011.07.001

Wasserman, M. D., Rye, R. O., Bethke, P. M., & Arribas, A. J. (1992). Methods for separation and total stable isotope analysis of alunite, 20. Retrieved from http://pubs.usgs.gov/of/1992/0009/report.pdf

White, N. C., & Hedenquist, J. (1995). Epithermal Gold Deposits. Styles, characteristics and exploration. *SEG Newsletter*, *23*, 1,9-13. http://doi.org/10.1080/00207540410001683261

Yang, K., Huntington, J. F., Boardman, J. W., & Mason, P. (1999). Mapping hydrothermal alteration in the Comstock mining district, Nevada, using simulated satellite-borne hyperspectral data. *Australian Journal of Earth Sciences*, *46*(6), 915–922. http://doi.org/10.1046/j.1440-0952.1999.00754.x

Yang, K., Huntington, J. F., Browne, P. R. L., & Ma, C. (2000). An infrared spectral reflectance study of hydrothermal alteration minerals from the Te Mihi sector of the Wairakei geothermal system, New Zealand. *Geothermics*, *29*(3), 377–392. http://doi.org/10.1016/S0375-6505(00)00004-3

APPENDICES

Appendix 1. Non-imaging spectroscopy

The complete spectral library with The Spectral Assistant interpretation from The Spectral Geologist Software is attached to the digital version of this document.

Appendix 2. Wavelength maps summary

It shows the ranges used in the Wavelength Mapping algorithm and the generic name of each of them in the data attached to the digital version of this document.

Wavelength range	Generic files name
1200 - 2400nm	Wavem_map1.n
1450 - 1550nm	WavemS_map2.n
1460 - 1495nm	WavemS1_map3.n
2100 - 2400nm	WavemL_map4.n
2100 - 2250nm	WavemL1_map5.n
1880 - 2050nm	WavemW_map6.n
1840 - 1875nm	WavemJ_map7.n
2090 - 2150nm	WavemZ_map8.n
2100 - 2195nm	WavemC_map9.n
1380 - 1409nm	WavemS2_map10.n
1717 - 1815nm	WavemS3_map11.n

Appendix 3. Sample selection

The two tables show a summary of the selected alunite samples and kaolin group samples, respectively, with the name of the ASD spectra in the entire spectral library, and The Spectral Assistant (TSA) interpretation.

Selected Alunite samples	Spectrum file	TSG interpretation	
		TSA_S Mineral1	TSA_S Mineral2
Sample008	Rod00020	Pyrophyllite	Kaolinite
Sample008	Rod00022	Na_Alunite	K_Alunite
Sample061	Rod00163	Dickite	K_Alunite
Sample061	Rod00164	K_Alunite	NULL
Sample061	Rod00165	Kaolinite	Na_Alunite
Sample063	Rod00169	Na_Alunite	K_Alunite
Sample063	Rod00170	Na_Alunite	K_Alunite
Sample063	Rod00171	Halloysite	Na_Alunite
Sample094	Rod00262	Na_Alunite	K_Alunite
Sample094	Rod00263	Na_Alunite	K_Alunite
Sample094	Rod00264	Na_Alunite	K_Alunite
Sample101	Rod00283	Halloysite	Na_Alunite
Sample101	Rod00284	Halloysite	Na_Alunite
Sample101	Rod00285	Halloysite	Na_Alunite
Sample208	Rod00605	K_Alunite	Na_Alunite
Sample208	Rod00606	K_Alunite	Na_Alunite
Sample208	Rod00607	K_Alunite	Na_Alunite
Sample213	Rod00620	Jarosite	K_Alunite
Sample213	Rod00621	Jarosite	K_Alunite
Sample213	Rod00622	Jarosite	K_Alunite
Sample228	Rod00665	Pyrophyllite	K_Alunite
Sample228	Rod00666	Pyrophyllite	K_Alunite
Sample228	Rod00667	Pyrophyllite	K_Alunite
Sample243	Rod00710	K_Alunite	NULL
Sample243	Rod00711	K_Alunite	NULL
Sample243	Rod00712	K_Alunite	NULL
Sample248	Rod00725	Na_Alunite	Illite
Sample248	Rod00726	Na_Alunite	Illite
Sample248	Rod00727	Illite	Na_Alunite
Sample260	Rod00761	K_Alunite	NULL
Sample260	Rod00762	K_Alunite	Na_Alunite
Sample260	Rod00763	K_Alunite	Na_Alunite

Selected Kaolin Group samples	Spectrum file	TSG interpretation	
		TSA_S Mineral1	TSA_S Mineral2
Sample103	Rod00289	Kaolinite	Halloysite
Sample103	Rod00290	Kaolinite	Gypsum
Sample103	Rod00291	Kaolinite	Halloysite
Sample127	Rod00361	Dickite	Nacrite
Sample127	Rod00362	Dickite	Jarosite
Sample127	Rod00363	Jarosite	Halloysite
Sample129	Rod00367	Dickite	Gypsum
Sample129	Rod00368	Dickite	Gypsum
Sample129	Rod00369	Dickite	Halloysite
Sample133	Rod00379	Kaolinite	Halloysite
Sample133	Rod00380	Kaolinite	Halloysite
Sample133	Rod00381	Kaolinite	Halloysite
Sample169	Rod00488	Kaolinite	Halloysite
Sample169	Rod00489	Kaolinite	Halloysite
Sample169	Rod00490	Kaolinite	Halloysite
Sample176	Rod00509	Kaolinite	Pyrophyllite
Sample176	Rod00510	Kaolinite	Pyrophyllite
Sample176	Rod00511	Kaolinite	Pyrophyllite
Sample219	Rod00638	Dickite	Halloysite
Sample219	Rod00639	Kaolinite	Nacrite
Sample219	Rod00640	Kaolinite	Nacrite
Sample247	Rod00722	Dickite	Nacrite
Sample247	Rod00723	Dickite	Nacrite
Sample247	Rod00724	Dickite	Jarosite
Sample257	Rod00752	Kaolinite	Nacrite
Sample257	Rod00753	Dickite	Halloysite
Sample257	Rod00754	Dickite	Halloysite

Appendix 4. Spectral Angle Mapper (SAM) results

The next table shows a summary of the percentages of the mineral abundances from the Spectral Angle Mapper algorithm per sample.

Sample # (% SAM)	260 sideA	260 sideB	247	228	208	176	103	101	127	129	213	61	169	248	219	63	94	94 small	243	257	8	133
Silicification	81.33	84.95	0.00	0.10	0.06	0.00	0.00	0.04	0.00	0.00	0.00	0.00	0.00	0.00	0.00	0.00	0.00	5.06	0.09	0.00	0.00	0.00
Alunite long	6.94	5.54	0.00	4.78	11.66	0.00	0.00	0.86	0.02	0.00	0.38	0.19	0.00	1.66	0.00	1.29	0.00	0.00	3.02	0.01	26.34	0.00
Pyrophyllite	0.77	0.45	31.96	0.63	46.15	0.00	0.00	14.20	0.00	5.76	0.11	0.00	0.00	0.01	20.16	0.00	0.00	0.00	0.00	0.00	0.00	0.00
Pyrophyllite + water	0.00	0.00	0.00	25.81	0.00	0.00	0.00	0.00	0.00	0.00	0.00	0.00	0.00	0.00	0.00	0.00	0.00	0.00	0.00	0.00	0.00	0.00
Dickite	0.00	0.01	0.00	1.37	0.00	0.00	0.09	0.12	0.02	12.71	0.00	0.00	0.00	0.00	55.07	0.00	0.00	0.00	0.00	0.89	0.00	0.00
Nacrite	0.27	0.46	0.04	5.26	9.92	0.92	0.17	0.08	25.33	11.07	3.57	0.00	0.49	0.68	0.53	0.94	0.00	0.00	0.76	15.96	1.93	0.00
Kaolinite HX	0.00	0.00	0.00	0.00	0.00	0.50	0.30	0.14	4.08	1.61	0.00	0.00	0.00	0.00	2.68	0.00	0.00	0.00	0.00	0.10	0.00	0.00
Kaolinite HX_W	0.00	0.03	0.00	0.06	0.00	93.27	23.08	0.28	38.94	0.10	0.00	0.10	0.00	0.00	0.01	15.77	0.00	0.00	0.00	0.02	0.00	12.40
Illite	0.00	0.00	0.00	2.77	0.04	0.00	0.00	0.18	0.07	0.00	8.90	0.00	36.98	3.73	0.00	0.00	0.00	0.00	0.00	0.01	0.02	0.03
Montmorillonite	5.24	3.59	50.15	14.60	0.64	0.00	0.02	72.17	0.00	37.33	56.43	0.00	0.18	24.07	5.94	0.03	0.00	0.00	0.00	26.73	0.26	0.00
Kaolinite MX	0.02	0.33	0.01	2.17	0.10	0.00	4.78	0.51	1.05	2.82	0.00	0.00	0.00	0.00	15.01	0.08	0.00	0.00	0.00	6.06	0.03	0.01
Halloysite dehydrated	0.00	0.17	0.00	3.28	0.00	5.09	71.33	0.47	24.38	2.44	0.06	0.00	15.56	0.03	0.42	3.71	0.00	0.00	0.00	3.19	0.25	1.98
Halloysite hydrated	0.38	0.70	0.80	38.46	2.26	0.00	0.00	10.52	0.07	26.07	23.78	0.00	41.72	63.74	0.03	0.14	0.00	0.00	0.00	42.66	1.37	0.01
Alunite medium	2.23	1.79	0.00	0.00	6.27	0.00	0.00	0.00	0.00	0.00	0.30	0.00	0.00	0.00	0.00	69.09	49.27	70.51	23.47	0.00	66.34	0.00
Kaolinite PX	0.00	0.00	0.00	0.05	0.04	0.00	0.12	0.01	0.00	0.01	0.93	4.62	5.07	0.00	0.00	1.42	0.04	0.16	0.00	0.00	0.89	7.03
Gypsum	0.00	0.01	0.00	0.02	2.58	0.00	0.00	0.20	0.00	0.00	0.01	0.00	0.00	0.32	0.00	0.00	0.00	0.00	0.09	0.00	0.02	0.00
Jarosite overall	0.00	0.00	0.00	0.00	0.89	0.00	0.00	0.00	0.00	0.00	0.00	0.00	0.00	0.00	0.00	0.00	0.00	0.00	0.00	0.00	0.00	0.00
Jarosite 1936	0.01	0.00	0.32	0.00	2.01	0.00	0.00	0.00	0.63	0.00	0.60	0.00	0.00	0.00	0.00	0.00	0.00	0.00	0.00	0.00	0.00	0.00
Alunite short-sideA	1.64	0.00	0.00	0.00	0.00	0.00	0.00	0.00	0.00	0.00	0.02	0.00	0.00	0.00	0.00	0.00	4.42	0.56	33.58	0.00	0.00	0.00
Alunite short-sideB	0.63	0.76	0.00	0.00	2.42	0.00	0.00	0.00	0.00	0.00	0.02	0.00	0.00	0.00	0.00	0.00	0.00	0.00	0.04	0.00	0.40	0.00
Unclassified	0.55	1.21	16.72	0.65	14.96	0.22	0.10	0.21	5.41	0.08	4.90	95.09	0.00	5.76	0.15	7.53	46.28	23.70	38.95	4.38	2.17	78.53

Appendix 5. Iterative Spectral Mixture Analysis (ISMA) results

The table below shows a summary of the percentages of the accumulated mineral fraction abundances from the Iterative Spectral Mixture Analysis per sample.

Sample # (% ISMA)	260 sideA	260 sideB	247	228	208	176	103	101	127	129	213	61	169	248	219	63	94	94 small	243	257	8	133
Silicification	74.64	74.54	6.52	16.52	10.76	0.02	0.79	16.69	0.00	0.69	21.17	0.00	3.08	0.44	0.62	0.02	0.00	0.03	0.58	7.35	0.69	0.04
Alunite long	1.24	0.91	0.01	3.05	1.59	0.41	0.00	1.59	0.01	0.00	0.02	0.06	0.00	1.23	0.00	0.46	0.23	6.17	12.44	0.03	8.02	0.00
Pyrophyllite	0.60	0.38	26.35	7.71	15.45	0.00	0.01	10.20	0.00	18.99	1.08	0.00	0.05	0.09	33.44	0.07	0.00	0.00	0.00	1.96	5.38	0.00
Pyrophyllite + water	0.02	0.01	0.00	33.34	0.00	1.65	0.00	0.00	0.00	0.00	0.00	0.00	0.00	0.00	0.00	0.00	0.00	0.00	0.00	0.00	0.00	0.00
Dickite	0.03	0.03	0.91	0.01	0.01	0.00	9.20	0.16	0.33	9.23	0.00	0.00	7.56	0.00	35.93	3.00	0.00	0.00	0.00	6.57	0.01	0.03
Nacrite	0.10	0.05	0.14	7.41	0.04	1.23	0.17	0.26	24.78	24.49	1.00	0.00	2.45	2.50	4.51	1.27	0.01	0.00	0.00	20.21	1.37	0.00
Kaolinite HX	0.00	0.00	0.00	0.00	0.00	1.37	10.95	0.18	8.88	1.99	0.00	0.00	0.28	0.00	9.44	1.62	0.00	0.00	0.00	0.53	0.00	0.35
Kaolinite HX_W	0.07	0.11	0.00	0.29	0.00	84.65	52.76	0.40	51.03	0.40	0.00	0.26	0.01	0.00	0.91	22.70	0.05	0.00	0.01	0.34	0.00	22.15
Illite	0.00	0.00	0.00	1.21	0.00	0.17	0.37	0.17	0.03	0.02	14.69	0.13	14.36	1.43	0.00	0.00	0.00	0.03	0.02	0.12	0.00	0.00
Montmorillonite	0.32	0.15	46.02	4.43	1.21	0.00	0.01	37.43	0.01	24.54	31.00	0.00	1.65	31.52	0.66	0.06	0.00	0.00	0.00	19.73	1.49	0.00
Kaolinite MX	0.02	0.04	0.02	0.00	0.00	0.12	3.22	1.15	0.55	0.00	0.01	0.00	9.86	0.00	6.65	0.00	0.00	0.00	0.00	3.86	0.00	0.09
Halloysite dehydrated	0.00	0.00	0.00	0.00	0.00	0.16	30.57	0.10	1.56	1.02	0.00	0.00	1.40	0.00	0.00	1.01	0.00	0.00	0.00	2.49	0.01	0.28
Halloysite hydrated	0.00	0.00	0.22	0.33	0.57	0.00	0.02	3.10	0.12	17.82	11.13	0.00	44.22	55.78	0.00	0.00	0.00	0.00	0.00	33.07	1.40	0.00
Alunite medium	1.00	0.46	0.00	0.06	4.56	0.00	0.00	0.00	0.00	0.00	0.01	100.99	0.00	0.00	0.00	75.60	5.57	4.12	1.69	0.00	49.31	0.00
Kaolinite PX	0.01	0.00	0.00	0.34	0.43	0.00	4.91	0.04	0.20	0.15	3.13	29.90	26.85	1.78	0.00	7.06	43.68	50.34	2.85	0.36	0.58	70.39
Gypsum	0.13	0.48	0.99	25.93	30.28	0.82	0.02	7.02	1.17	1.27	10.53	0.00	9.76	29.40	0.00	0.01	0.04	0.08	0.03	0.64	16.37	0.00
Jarosite overall	0.00	0.02	0.00	0.00	6.79	0.00	0.00	0.00	2.53	0.00	1.84	0.00	0.00	0.00	0.00	0.00	0.00	0.00	0.04	0.00	0.00	0.00
Jarosite 1936	0.26	0.33	21.91	0.25	4.85	0.00	0.00	0.09	1.19	0.49	4.74	0.00	0.00	2.77	1.12	0.00	0.00	0.00	0.38	3.52	0.73	0.00
Alunite short-sideA	2.43	0.30	0.00	0.04	1.12	0.00	0.00	0.00	0.00	0.00	1.58	0.00	0.00	0.01	0.00	4.44	75.95	62.46	98.16	0.00	0.68	0.02
Alunite short-sideB	3.40	3.32	0.02	0.43	20.38	0.00	0.00	0.19	0.00	0.00	2.03	0.00	0.00	0.33	0.00	0.15	0.47	0.00	4.13	0.04	32.43	0.00
Albedo	15.74	18.88	-3.12	-1.35	1.97	9.37	-12.28	21.21	7.61	-1.09	-3.97	-31.33	-21.53	-27.26	6.70	-17.47	-26.02	-23.24	-20.31	-0.84	-18.46	6.65

Appendix 6. Normalization of the Iterative Spectral Mixture Analysis (ISMA) results

The next table shows a summary of the normalized percentages of the accumulated mineral fraction abundances from the Iterative Spectral Mixture Analysis per sample, after the values of the albedo endmember were removed.

Sample # (% ISMA_N)	260 sideA	260 sideB	247	228	208	176	103	101	127	129	213	61	169	248	219	63	94	94 small	243	257	8	133
Silicification	88.86	90.42	4.21	14.07	12.61	0.03	0.05	20.42	0.00	0.53	16.01	0.00	2.31	0.27	0.53	0.02	0.00	0.02	0.34	6.01	0.54	0.02
Alunite long	2.09	1.70	0.01	4.79	1.66	0.60	0.00	1.82	0.05	0.00	0.02	0.06	0.00	1.20	0.00	0.42	0.25	6.08	11.94	0.03	7.33	0.00
Pyrophyllite	0.68	0.49	26.91	7.79	34.30	0.00	0.01	16.06	0.00	19.93	1.12	0.00	0.05	0.09	35.82	0.07	0.00	0.00	0.00	1.95	4.52	0.00
Pyrophyllite + water	0.02	0.01	0.00	36.67	0.00	1.70	0.00	0.00	0.00	0.00	0.00	0.00	0.00	0.00	0.00	0.00	0.00	0.00	0.00	0.00	0.00	0.00
Dickite	0.03	0.05	0.69	0.01	0.01	0.00	8.17	0.18	0.33	9.95	0.00	0.00	6.70	0.00	40.59	2.49	0.00	0.00	0.00	6.35	0.01	0.02
Nacrite	0.11	0.11	0.17	8.08	0.06	1.18	0.17	0.27	29.84	24.42	1.16	0.00	2.24	2.79	4.56	1.22	0.01	0.00	0.00	21.61	1.41	0.00
Kaolinite HX	0.00	0.00	0.00	0.00	0.00	1.24	9.60	0.22	9.47	2.15	0.00	0.00	0.23	0.00	9.23	1.42	0.00	0.00	0.00	0.53	0.00	0.32
Kaolinite HX_W	0.07	0.27	0.00	0.26	0.00	93.84	44.07	0.49	51.31	0.47	0.00	0.22	0.01	0.00	0.87	20.65	0.05	0.00	0.00	0.34	0.00	20.85
Illite	0.00	0.00	0.00	1.66	0.00	0.22	0.33	0.21	0.09	0.02	15.17	0.12	13.90	1.39	0.00	0.00	0.00	0.03	0.02	0.12	0.00	0.00
Montmorillonite	0.47	0.42	48.58	5.49	1.20	0.00	0.01	49.00	0.01	25.01	35.15	0.00	1.54	31.92	0.68	0.05	0.00	0.00	0.00	22.48	1.32	0.00
Kaolinite MX	0.03	0.04	0.03	0.00	0.00	0.15	2.99	1.47	1.30	0.00	0.01	0.00	8.95	0.00	6.85	0.00	0.00	0.00	0.00	4.07	0.00	0.08
Halloysite dehydrated	0.00	0.00	0.00	0.00	0.00	0.18	30.32	0.12	1.86	1.07	0.00	0.00	1.35	0.00	0.00	0.91	0.00	0.00	0.00	2.51	0.01	0.30
Halloysite hydrated	0.00	0.00	0.28	0.39	0.46	0.00	0.01	3.07	0.20	15.05	11.13	0.00	33.30	43.66	0.00	0.00	0.00	0.00	0.00	29.93	1.14	0.00
Alunite medium	1.32	0.72	0.00	0.05	3.98	0.00	0.00	0.00	0.00	0.00	0.01	72.93	0.00	0.00	0.00	62.88	5.10	3.71	1.73	0.00	47.75	0.00
Kaolinite PX	0.01	0.00	0.00	0.40	0.47	0.00	4.26	0.04	0.25	0.14	3.20	26.67	24.03	1.70	0.00	6.27	34.43	40.24	2.42	0.34	0.57	78.37
Gypsum	0.15	1.15	1.07	19.74	19.98	0.84	0.01	6.38	1.61	0.87	7.23	0.00	5.41	14.37	0.00	0.01	0.03	0.05	0.02	0.55	10.14	0.00
Jarosite overall	0.00	0.04	0.00	0.00	5.77	0.00	0.00	0.00	2.51	0.00	1.81	0.00	0.00	0.00	0.00	0.00	0.00	0.00	0.04	0.00	0.00	0.00
Jarosite 1936	0.27	0.41	18.02	0.21	4.33	0.00	0.00	0.10	1.18	0.37	4.60	0.00	0.00	2.37	0.86	0.00	0.00	0.00	0.37	3.14	0.63	0.00
Alunite short-sideA	2.64	0.40	0.00	0.04	0.84	0.00	0.00	0.00	0.00	0.00	1.78	0.00	0.00	0.00	0.00	3.50	59.83	49.87	80.11	0.00	0.67	0.02
Alunite short-sideB	3.24	3.73	0.01	0.36	14.34	0.00	0.00	0.15	0.00	0.00	1.60	0.00	0.00	0.23	0.00	0.09	0.30	0.00	3.00	0.04	23.97	0.00

Appendix 7. Quantification of the samples

Results of the quantification of the samples from the Iterative Spectral Mixture Analysis (ISMA), the normalization of the Iterative Spectral Mixture Analysis (ISMA) results and the Spectral Angle Mapper are shown in the plots below. They are presented per alteration zone based on the classification made by Arribas et al. (1995):

Supergene alteration

- Sample 063

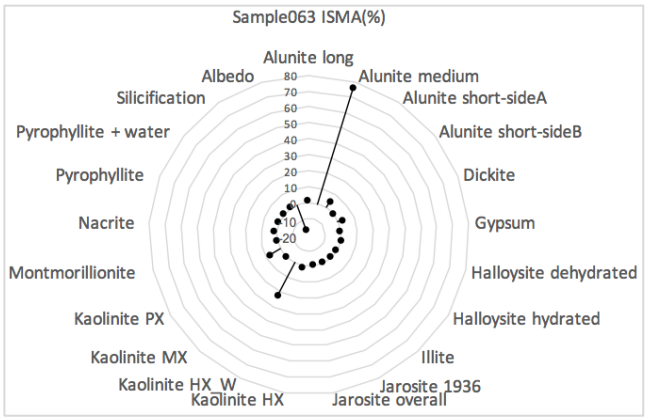

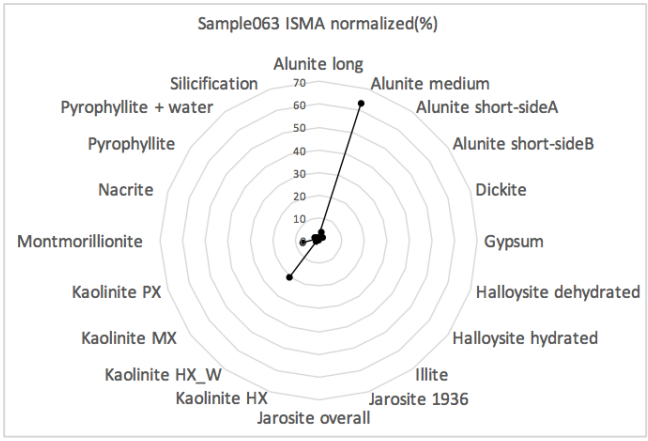

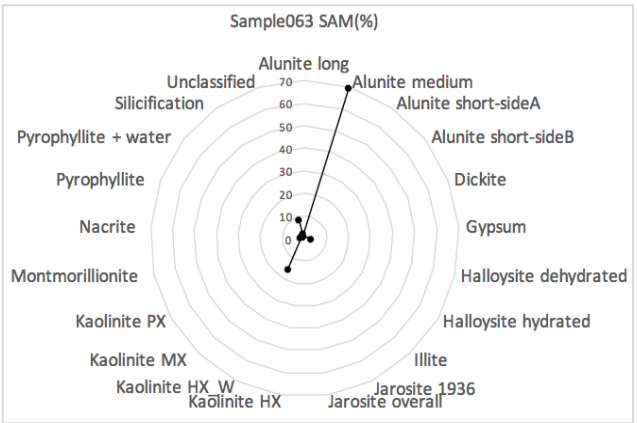

- Sample 094

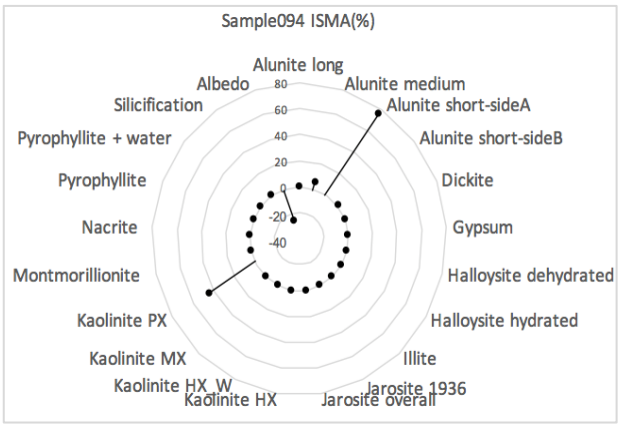
Sample094 ISMA(%)
Alunite long
Alunite medium
Alunite short-sideA
Alunite short-sideB
Dickite
Gypsum
Halloysite dehydrated
Halloysite hydrated
Illite
Jarosite 1936
Jarosite overall
Kaolinite HX
Kaolinite HX_W
Kaolinite MX
Kaolinite PX
Montmorillionite
Nacrite
Pyrophyllite
Pyrophyllite + water
Silicification
Albedo
80
60
40
20
0
-20
-40

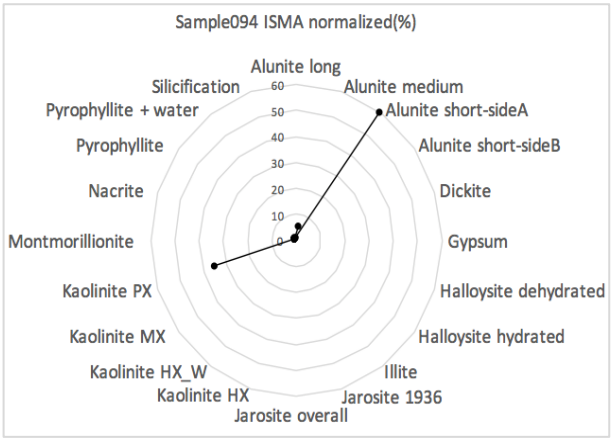
Sample094 ISMA normalized(%)
Alunite long
Alunite medium
Alunite short-sideA
Alunite short-sideB
Dickite
Gypsum
Halloysite dehydrated
Halloysite hydrated
Illite
Jarosite 1936
Jarosite overall
Kaolinite HX
Kaolinite HX_W
Kaolinite MX
Kaolinite PX
Montmorillionite
Nacrite
Pyrophyllite
Pyrophyllite + water
Silicification
60
50
40
30
20
10
0

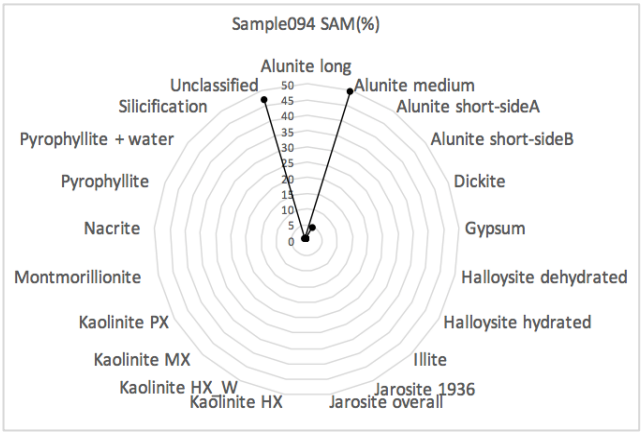
Sample094 SAM(%)
Alunite long
Alunite medium
Alunite short-sideA
Alunite short-sideB
Dickite
Gypsum
Halloysite dehydrated
Halloysite hydrated
Illite
Jarosite 1936
Jarosite overall
Kaolinite HX
Kaolinite HX_W
Kaolinite MX
Kaolinite PX
Montmorillionite
Nacrite
Pyrophyllite
Pyrophyllite + water
Silicification
Unclassified
50
45
40
35
30
25
20
15
10
5
0

- Sample 094 small

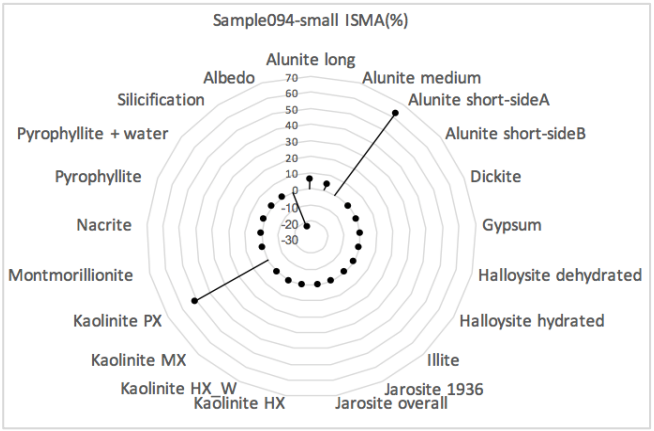

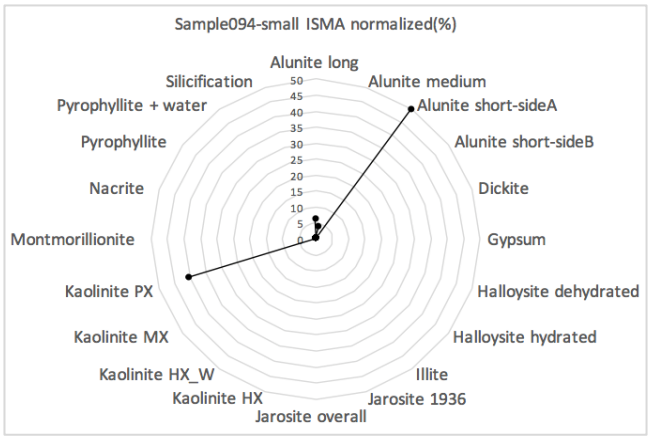

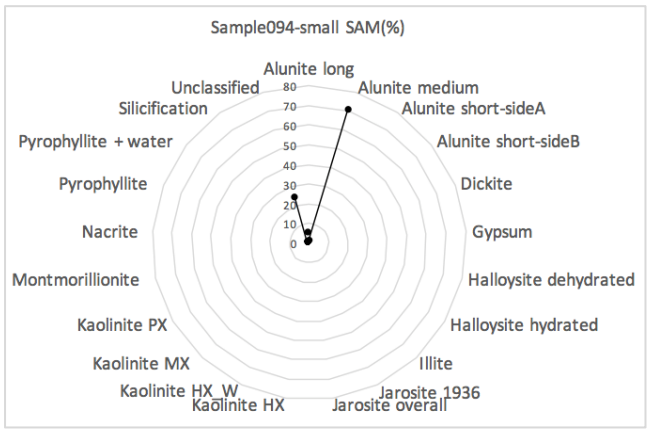

Edge with intermediate argillic:

- Sample 243

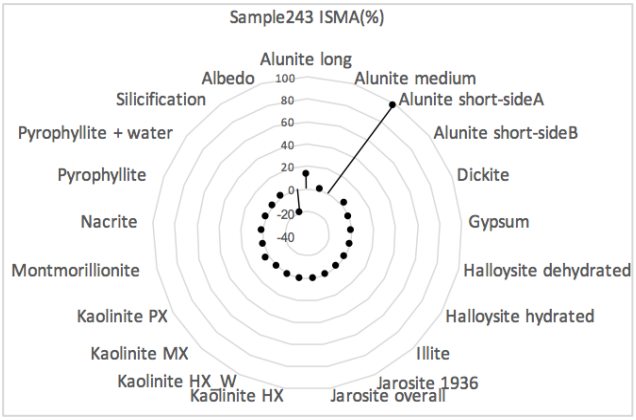

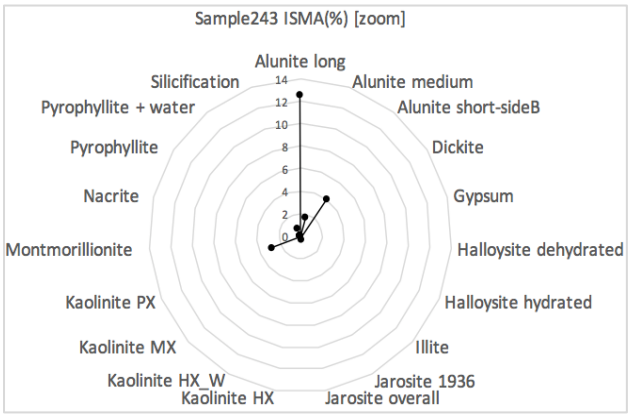

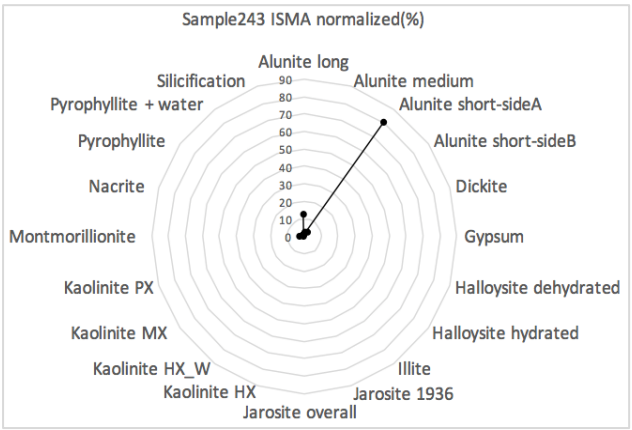

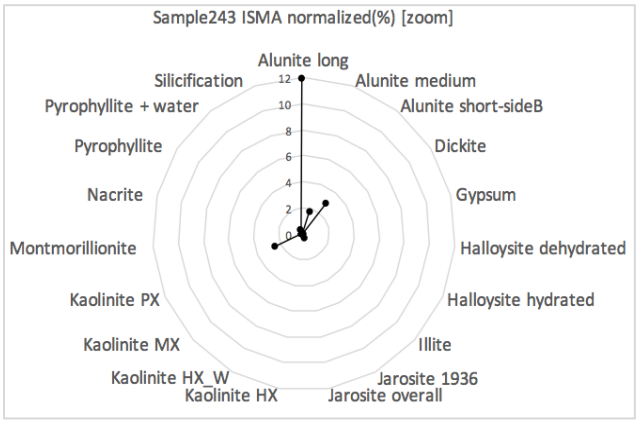

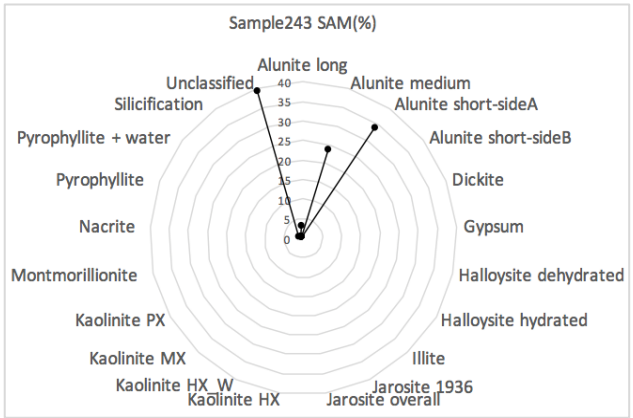

- Sample 257

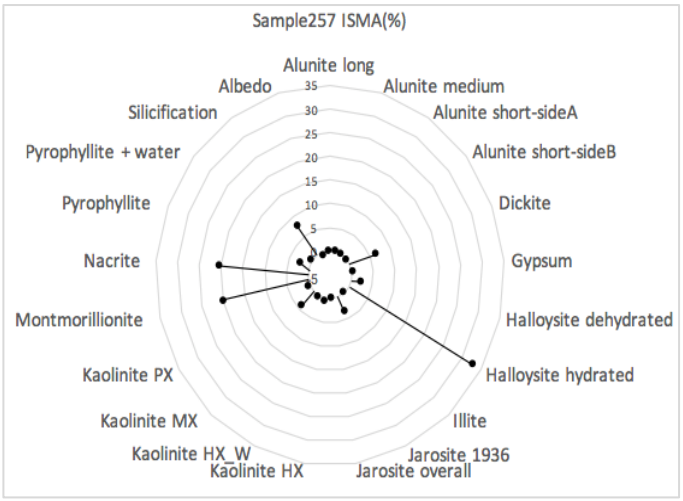
Sample257 ISMA(%)
Alunite long
Alunite medium
Alunite short-sideA
Alunite short-sideB
Dickite
Gypsum
Halloysite dehydrated
Halloysite hydrated
Illite
Jarosite 1936
Jarosite overall
Kaolinite HX
Kaolinite HX_W
Kaolinite MX
Kaolinite PX
Montmorillionite
Nacrite
Pyrophyllite
Pyrophyllite + water
Silicification
Albedo
35
30
25
20
15
10
5

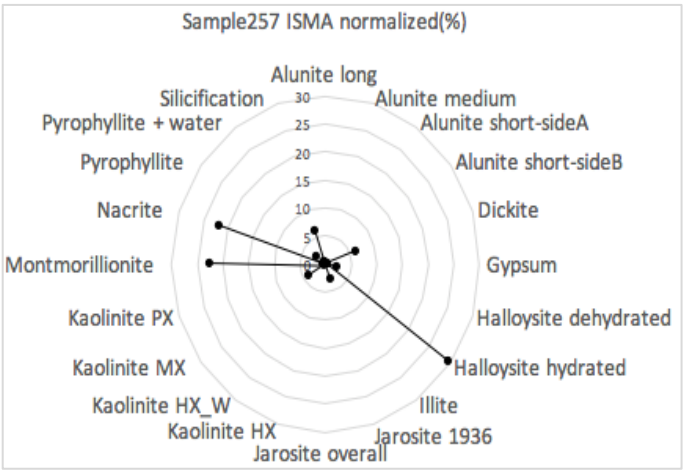
Sample257 ISMA normalized(%)
Alunite long
Alunite medium
Alunite short-sideA
Alunite short-sideB
Dickite
Gypsum
Halloysite dehydrated
Halloysite hydrated
Illite
Jarosite 1936
Jarosite overall
Kaolinite HX
Kaolinite HX_W
Kaolinite MX
Kaolinite PX
Montmorillionite
Nacrite
Pyrophyllite
Pyrophyllite + water
Silicification
30
25
20
15
10
5

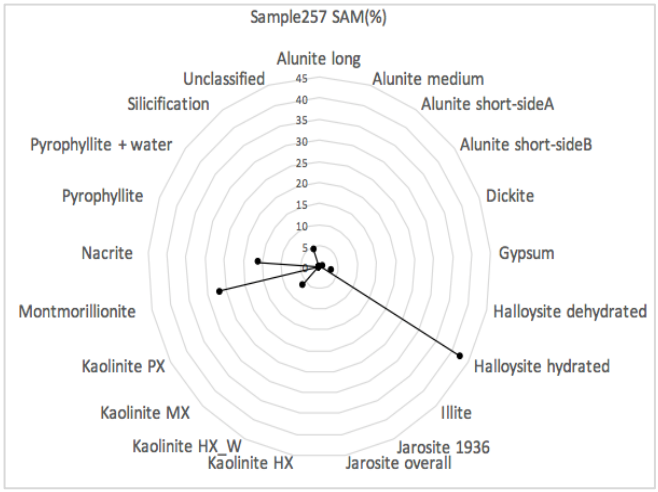
Sample257 SAM(%)
Alunite long
Alunite medium
Alunite short-sideA
Alunite short-sideB
Dickite
Gypsum
Halloysite dehydrated
Halloysite hydrated
Illite
Jarosite 1936
Jarosite overall
Kaolinite HX
Kaolinite HX_W
Kaolinite MX
Kaolinite PX
Montmorillionite
Nacrite
Pyrophyllite
Pyrophyllite + water
Silicification
Unclassified
45
40
35
30
25
20
15
10
5

Vuggy Silica

- Sample 260 sideA

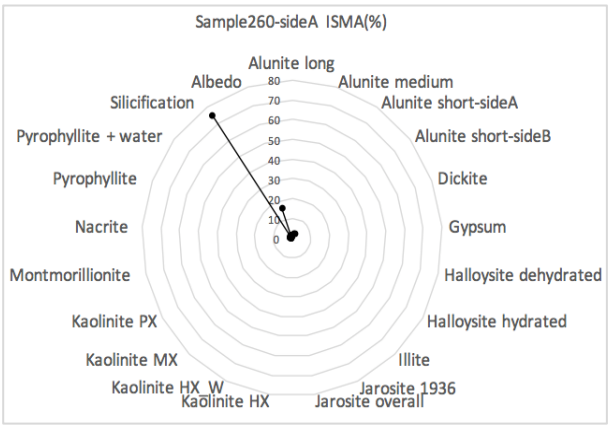

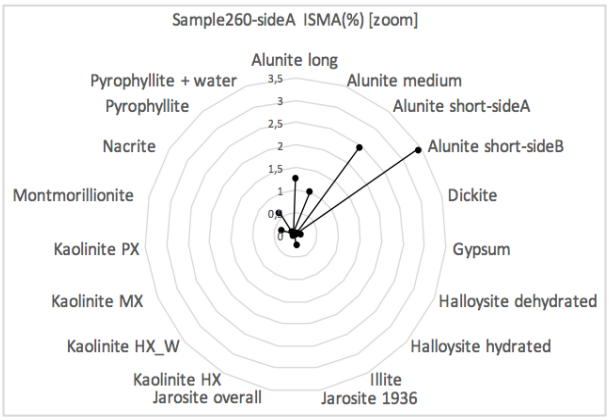

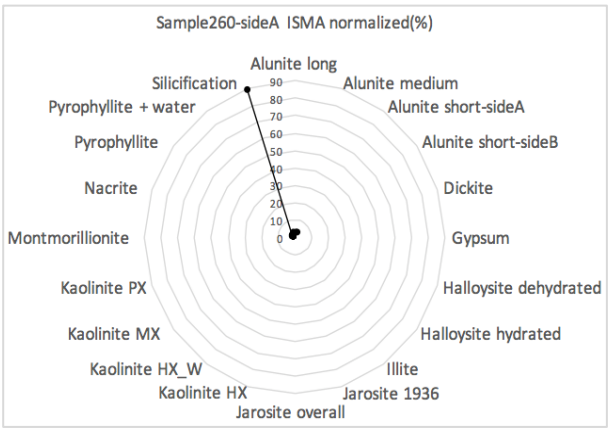

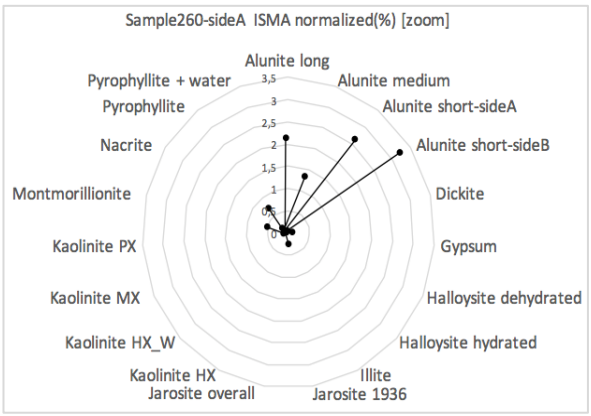

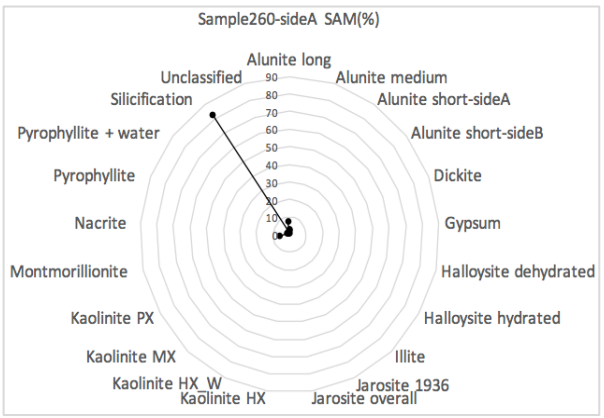

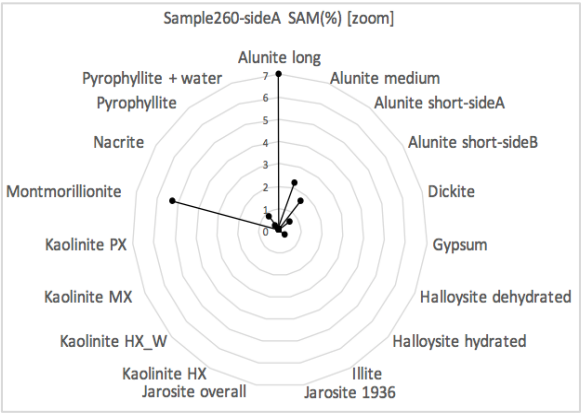

- Sample 260 side B

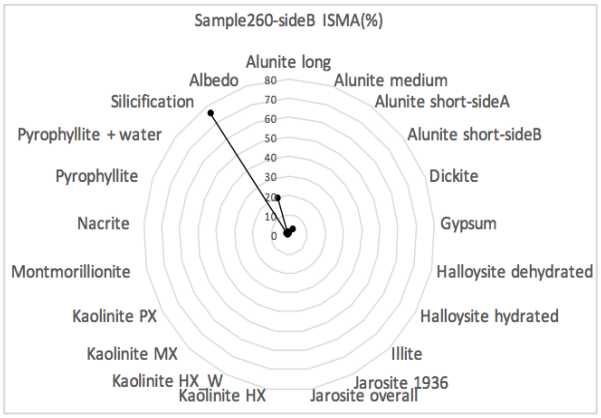

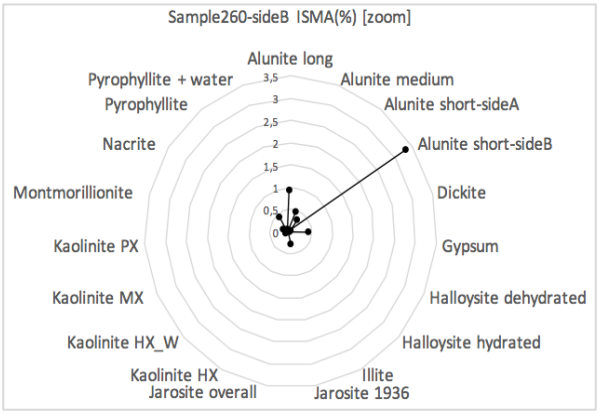

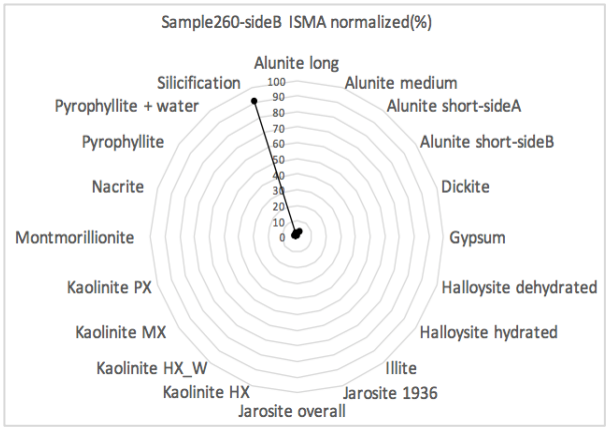

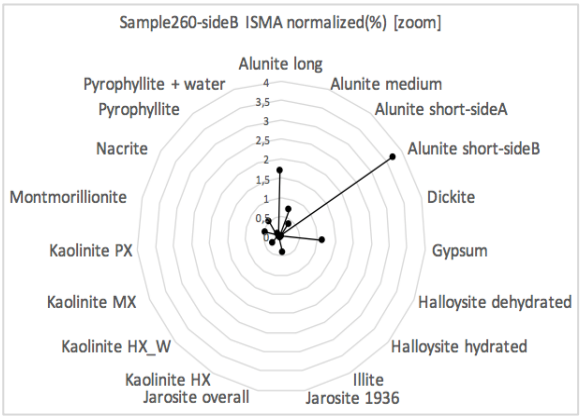

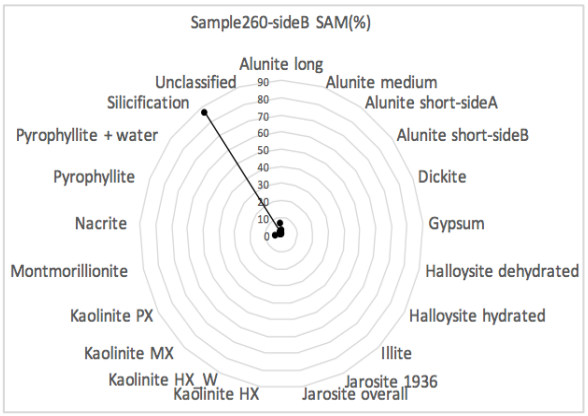

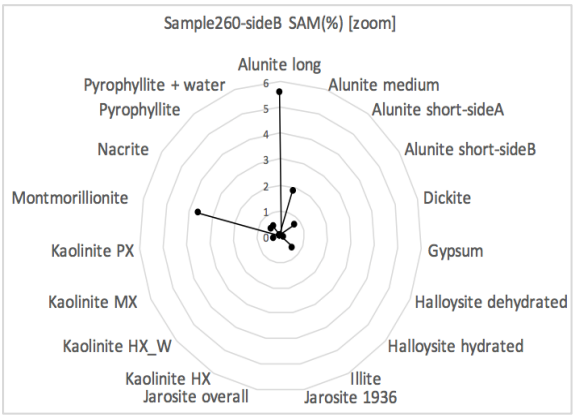

- Sample 247

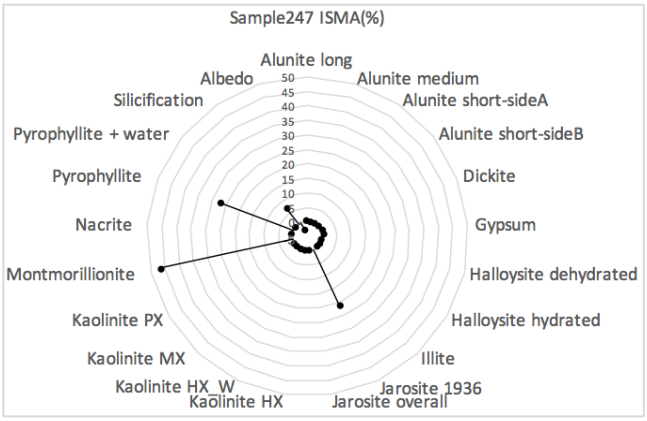
Sample247 ISMA(%)
Alunite long
Alunite medium
Alunite short-sideA
Alunite short-sideB
Dickite
Gypsum
Halloysite dehydrated
Halloysite hydrated
Illite
Jarosite 1936
Jarosite overall
Kaolinite HX
Kaolinite HX_W
Kaolinite MX
Kaolinite PX
Montmorillionite
Nacrite
Pyrophyllite
Pyrophyllite + water
Silicification
Albedo
50
45
40
35
30
25
20
15
10
5

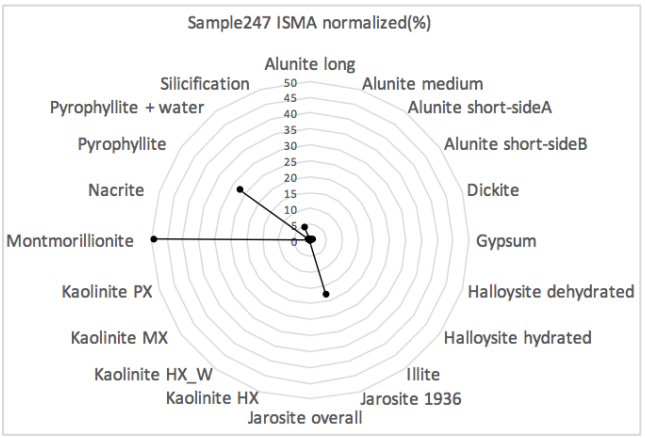
Sample247 ISMA normalized(%)
Alunite long
Alunite medium
Alunite short-sideA
Alunite short-sideB
Dickite
Gypsum
Halloysite dehydrated
Halloysite hydrated
Illite
Jarosite 1936
Jarosite overall
Kaolinite HX
Kaolinite HX_W
Kaolinite MX
Kaolinite PX
Montmorillionite
Nacrite
Pyrophyllite
Pyrophyllite + water
Silicification
50
45
40
35
30
25
20
15
10
5
0

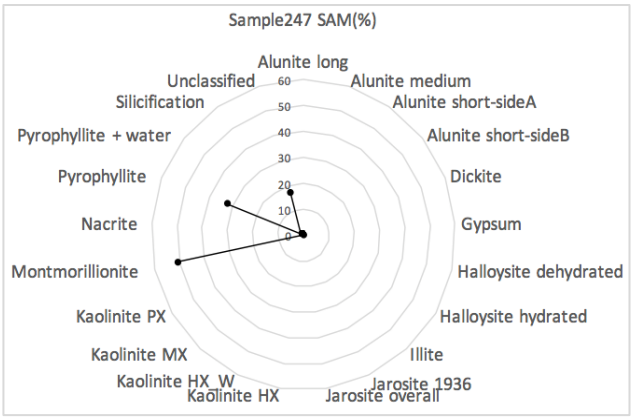
Sample247 SAM(%)
Alunite long
Alunite medium
Alunite short-sideA
Alunite short-sideB
Dickite
Gypsum
Halloysite dehydrated
Halloysite hydrated
Illite
Jarosite 1936
Jarosite overall
Kaolinite HX
Kaolinite HX_W
Kaolinite MX
Kaolinite PX
Montmorillionite
Nacrite
Pyrophyllite
Pyrophyllite + water
Silicification
Unclassified
60
50
40
30
20
10
0

Edge with advanced argillic:

- Sample 228

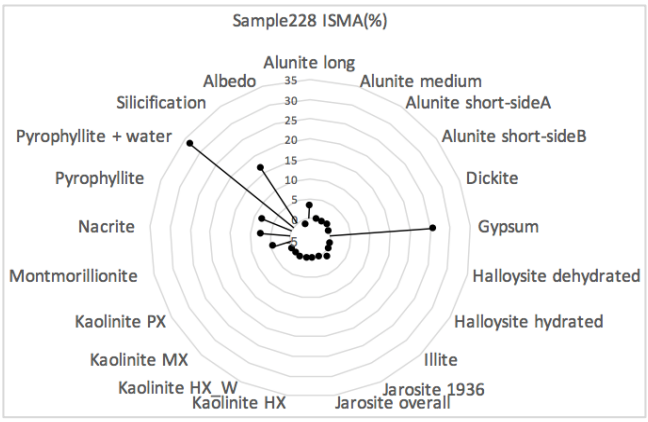

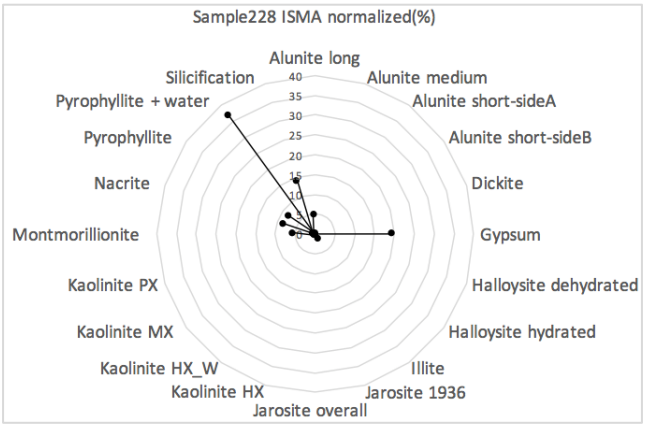

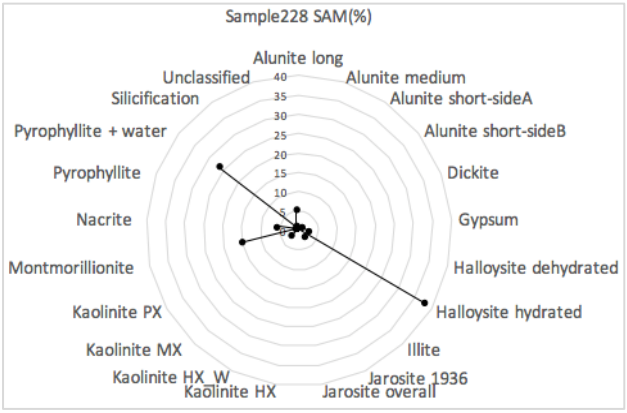

- Sample 208

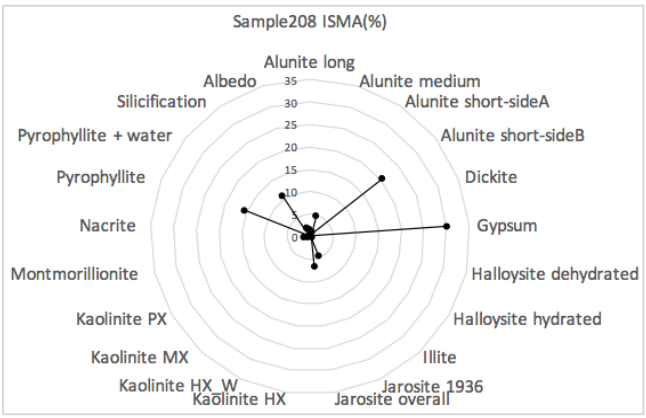
Sample208 ISMA(%)
Alunite long
Alunite medium
Alunite short-sideA
Alunite short-sideB
Dickite
Gypsum
Halloysite dehydrated
Halloysite hydrated
Illite
Jarosite 1936
Jarosite overall
Kaolinite HX
Kaolinite HX_W
Kaolinite MX
Kaolinite PX
Montmorillionite
Nacrite
Pyrophyllite
Pyrophyllite + water
Silicification
Albedo
35
30
25
20
15
10
5
0

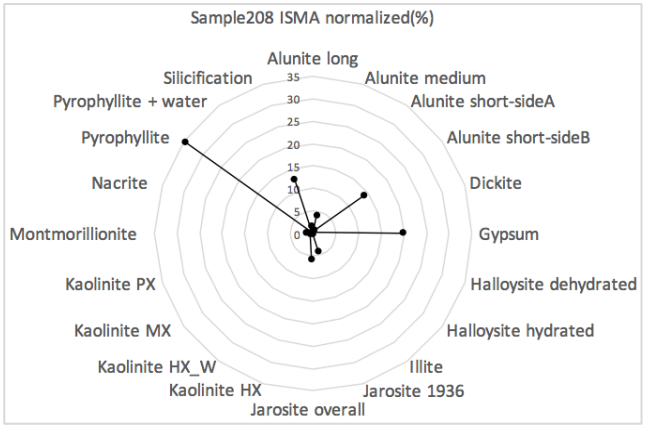
Sample208 ISMA normalized(%)
Alunite long
Alunite medium
Alunite short-sideA
Alunite short-sideB
Dickite
Gypsum
Halloysite dehydrated
Halloysite hydrated
Illite
Jarosite 1936
Jarosite overall
Kaolinite HX
Kaolinite HX_W
Kaolinite MX
Kaolinite PX
Montmorillionite
Nacrite
Pyrophyllite
Pyrophyllite + water
Silicification
35
30
25
20
15
10
5
0

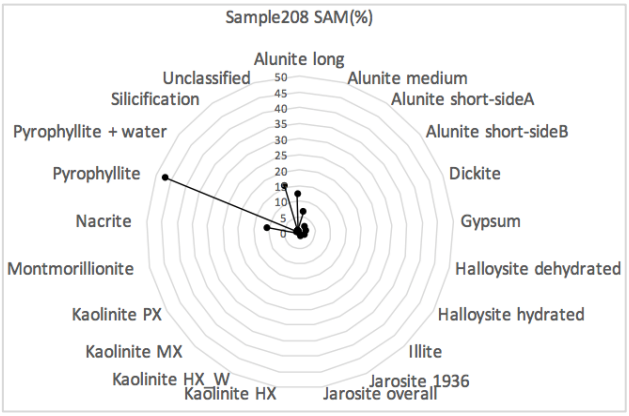
Sample208 SAM(%)
Alunite long
Alunite medium
Alunite short-sideA
Alunite short-sideB
Dickite
Gypsum
Halloysite dehydrated
Halloysite hydrated
Illite
Jarosite 1936
Jarosite overall
Kaolinite HX
Kaolinite HX_W
Kaolinite MX
Kaolinite PX
Montmorillionite
Nacrite
Pyrophyllite
Pyrophyllite + water
Silicification
Unclassified
50
45
40
35
30
25
20
15
10
5
0

Advanced Argillic

Edge with vuggy silica

- Sample 176

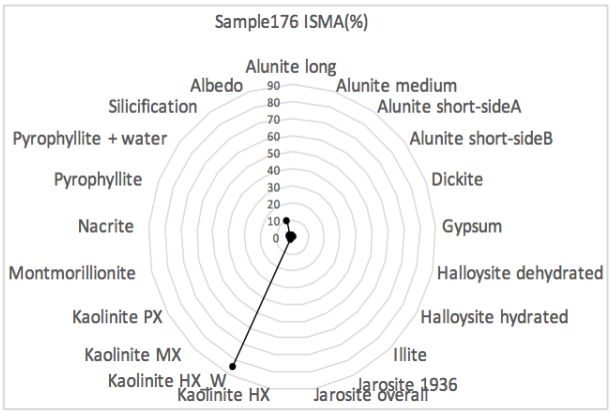

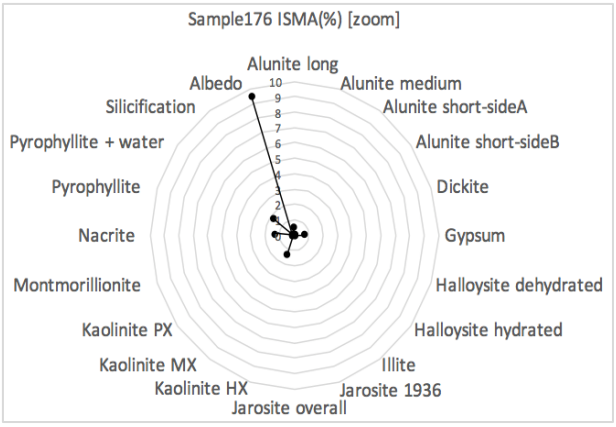

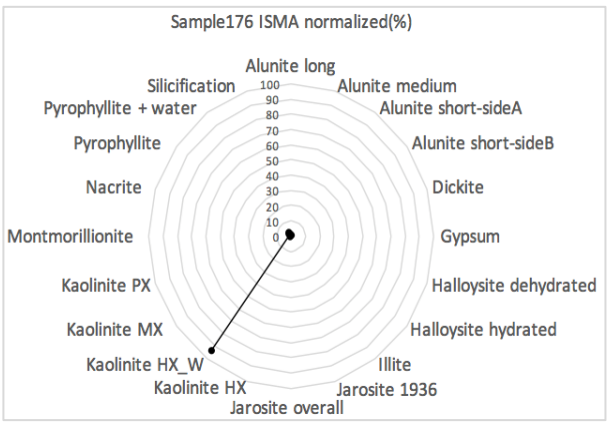

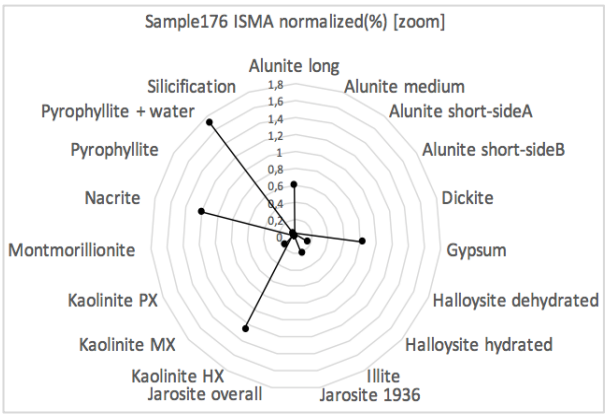

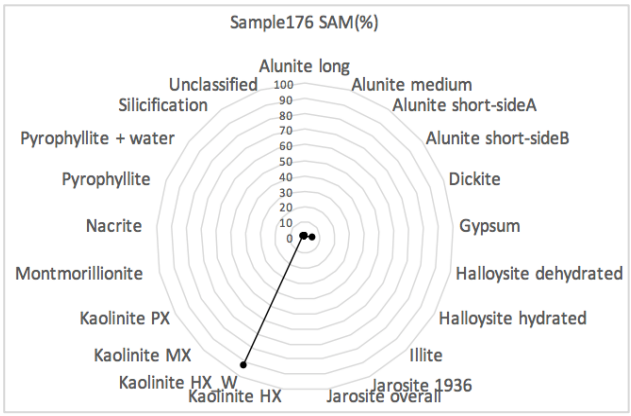

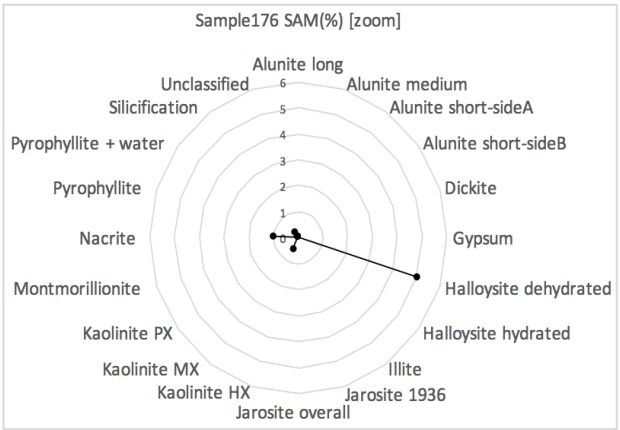

- Sample 103

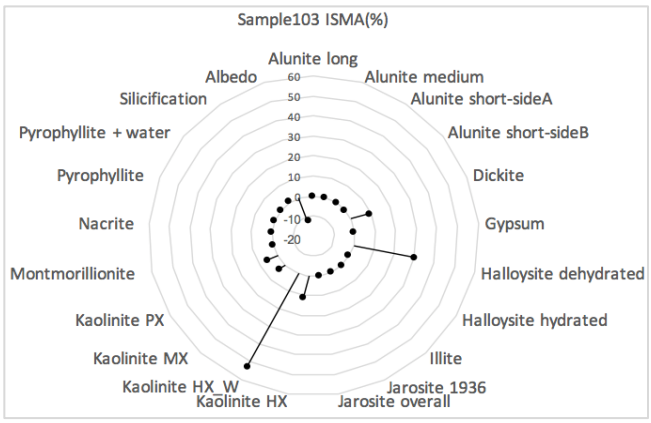
Sample103 ISMA(%)
Alunite long
Alunite medium
Alunite short-sideA
Alunite short-sideB
Dickite
Gypsum
Halloysite dehydrated
Halloysite hydrated
Illite
Jarosite 1936
Jarosite overall
Kaolinite HX
Kaolinite HX_W
Kaolinite MX
Kaolinite PX
Montmorillionite
Nacrite
Pyrophyllite
Pyrophyllite + water
Silicification
Albedo
60
50
40
30
20
10
0
-10
-20

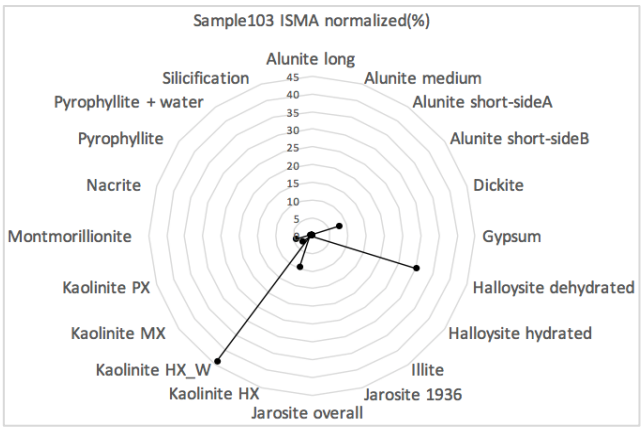
Sample103 ISMA normalized(%)
Alunite long
Alunite medium
Alunite short-sideA
Alunite short-sideB
Dickite
Gypsum
Halloysite dehydrated
Halloysite hydrated
Illite
Jarosite 1936
Jarosite overall
Kaolinite HX
Kaolinite HX_W
Kaolinite MX
Kaolinite PX
Montmorillionite
Nacrite
Pyrophyllite
Pyrophyllite + water
Silicification
45
40
35
30
25
20
15
10
5

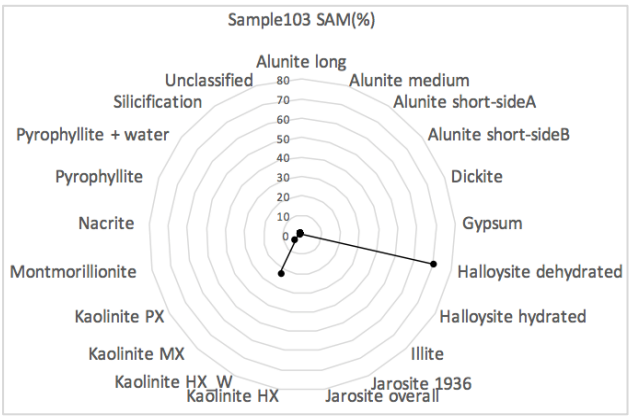
Sample103 SAM(%)
Alunite long
Alunite medium
Alunite short-sideA
Alunite short-sideB
Dickite
Gypsum
Halloysite dehydrated
Halloysite hydrated
Illite
Jarosite 1936
Jarosite overall
Kaolinite HX
Kaolinite HX_W
Kaolinite MX
Kaolinite PX
Montmorillionite
Nacrite
Pyrophyllite
Pyrophyllite + water
Silicification
Unclassified
80
70
60
50
40
30
20
10
0

- Sample 101

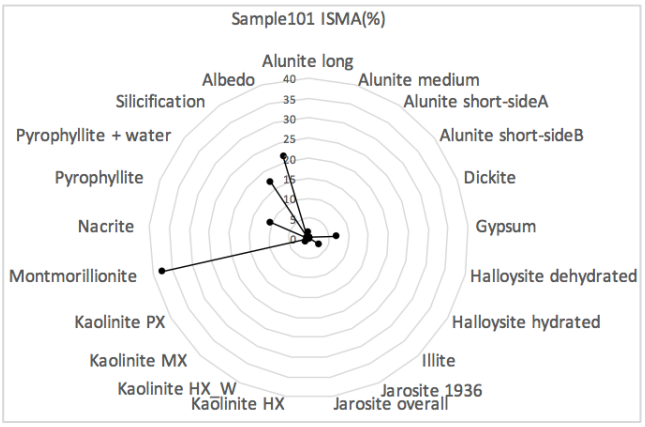
Sample101 ISMA(%)
Alunite long
Alunite medium
Alunite short-sideA
Alunite short-sideB
Dickite
Gypsum
Halloysite dehydrated
Halloysite hydrated
Illite
Jarosite 1936
Jarosite overall
Kaolinite HX
Kaolinite HX_W
Kaolinite MX
Kaolinite PX
Montmorillionite
Nacrite
Pyrophyllite
Pyrophyllite + water
Silicification
Albedo
40
35
30
25
20
15
10
5
0

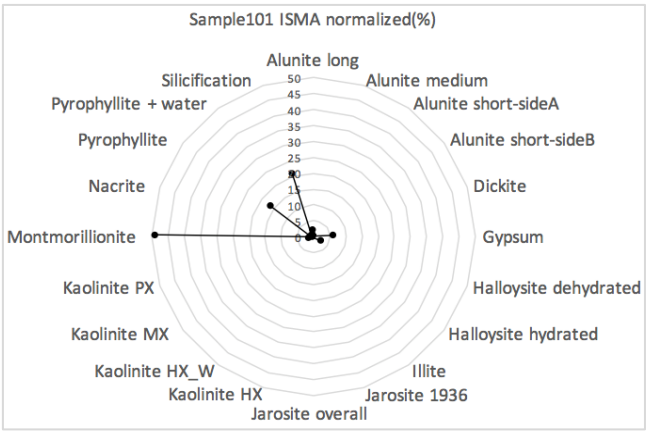
Sample101 ISMA normalized(%)
Alunite long
Alunite medium
Alunite short-sideA
Alunite short-sideB
Dickite
Gypsum
Halloysite dehydrated
Halloysite hydrated
Illite
Jarosite 1936
Jarosite overall
Kaolinite HX
Kaolinite HX_W
Kaolinite MX
Kaolinite PX
Montmorillionite
Nacrite
Pyrophyllite
Pyrophyllite + water
Silicification
50
45
40
35
30
25
20
15
10
5
0

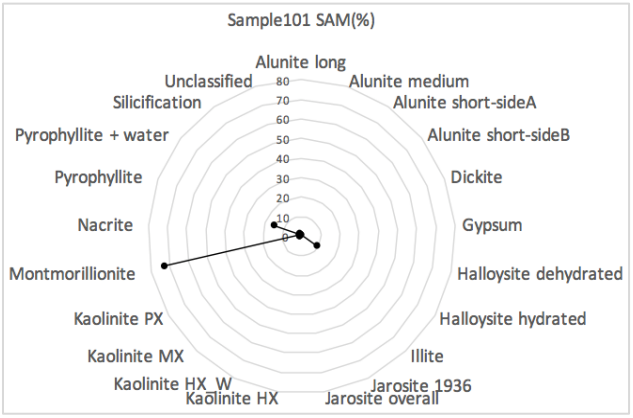
Sample101 SAM(%)
Alunite long
Alunite medium
Alunite short-sideA
Alunite short-sideB
Dickite
Gypsum
Halloysite dehydrated
Halloysite hydrated
Illite
Jarosite 1936
Jarosite overall
Kaolinite HX
Kaolinite HX_W
Kaolinite MX
Kaolinite PX
Montmorillionite
Nacrite
Pyrophyllite
Pyrophyllite + water
Silicification
Unclassified
80
70
60
50
40
30
20
10
0

Edge with intermediate argillic

- Sample 127

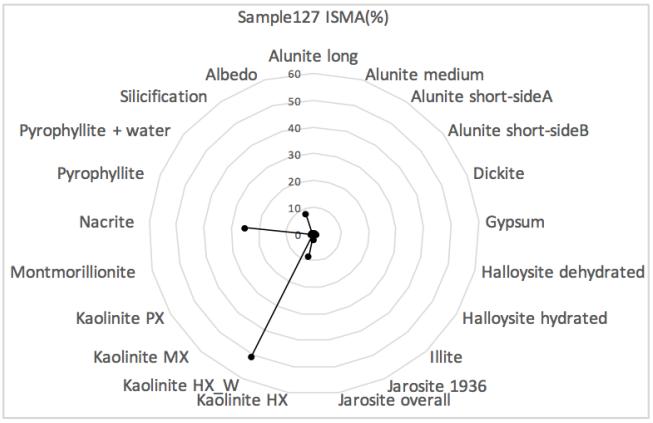

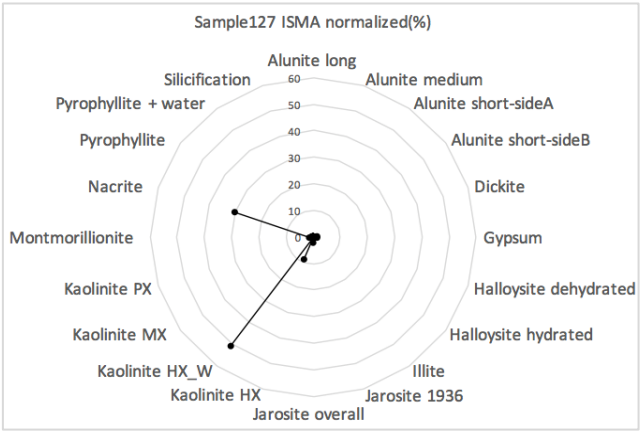

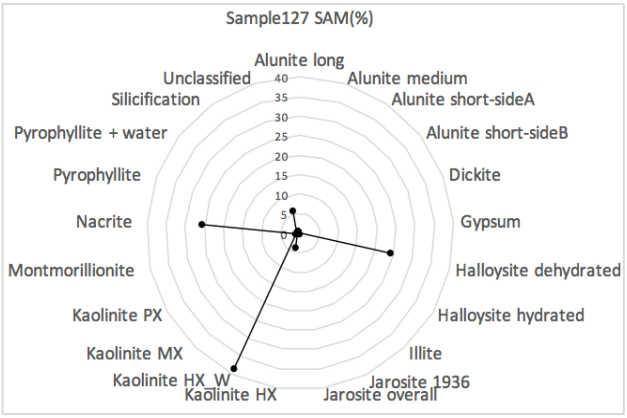

Intermediate argillic

- Sample 129

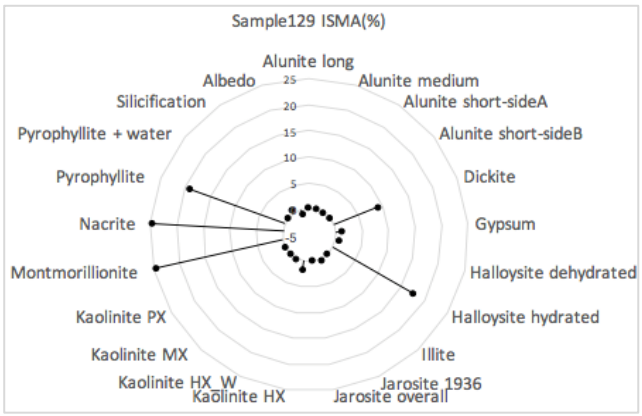

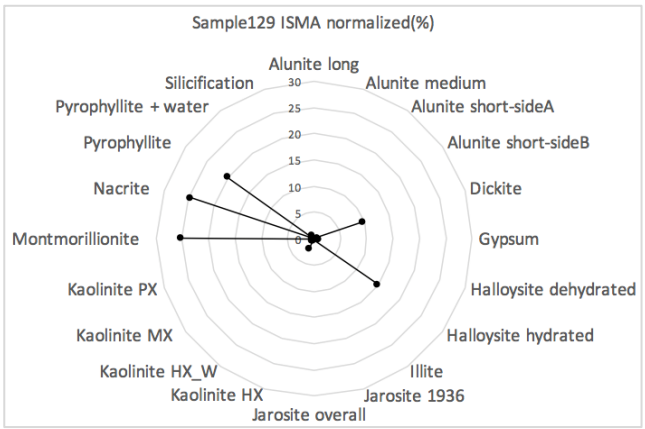

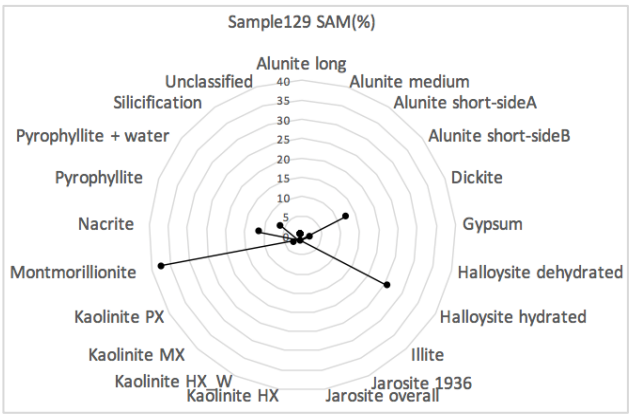

- Sample 213

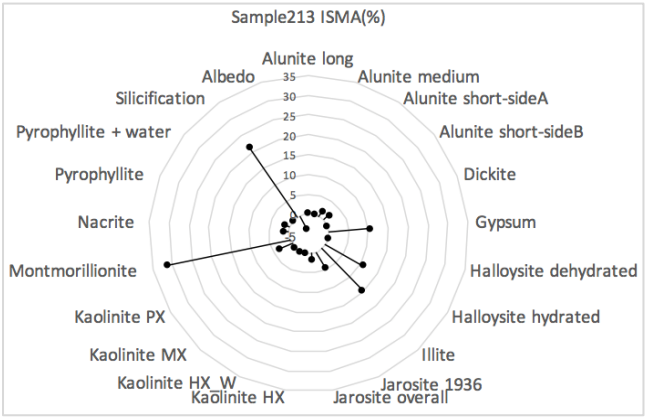
Sample213 ISMA(%)
Alunite long
Alunite medium
Alunite short-sideA
Alunite short-sideB
Dickite
Gypsum
Halloysite dehydrated
Halloysite hydrated
Illite
Jarosite 1936
Jarosite overall
Kaolinite HX
Kaolinite HX_W
Kaolinite MX
Kaolinite PX
Montmorillionite
Nacrite
Pyrophyllite
Pyrophyllite + water
Silicification
Albedo
35
30
25
20
15
10
5

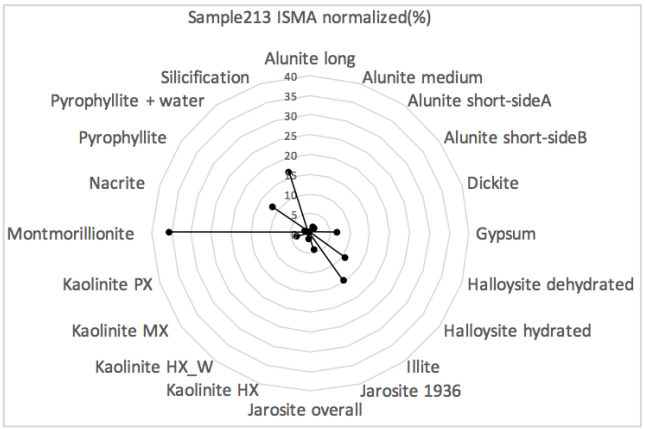
Sample213 ISMA normalized(%)
Alunite long
Alunite medium
Alunite short-sideA
Alunite short-sideB
Dickite
Gypsum
Halloysite dehydrated
Halloysite hydrated
Illite
Jarosite 1936
Jarosite overall
Kaolinite HX
Kaolinite HX_W
Kaolinite MX
Kaolinite PX
Montmorillionite
Nacrite
Pyrophyllite
Pyrophyllite + water
Silicification
40
35
30
25
20
15
10
5

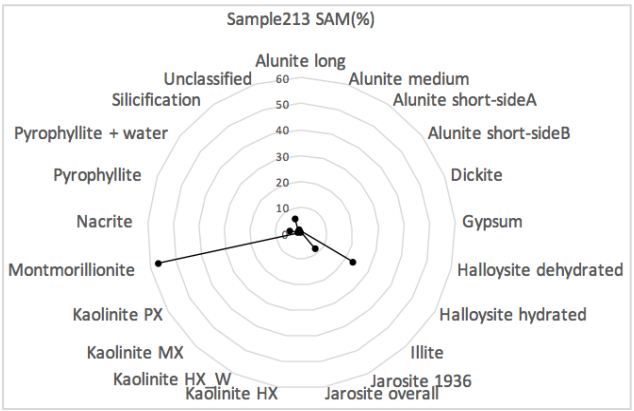
Sample213 SAM(%)
Alunite long
Alunite medium
Alunite short-sideA
Alunite short-sideB
Dickite
Gypsum
Halloysite dehydrated
Halloysite hydrated
Illite
Jarosite 1936
Jarosite overall
Kaolinite HX
Kaolinite HX_W
Kaolinite MX
Kaolinite PX
Montmorillionite
Nacrite
Pyrophyllite
Pyrophyllite + water
Silicification
Unclassified
60
50
40
30
20
10

- Sample 061

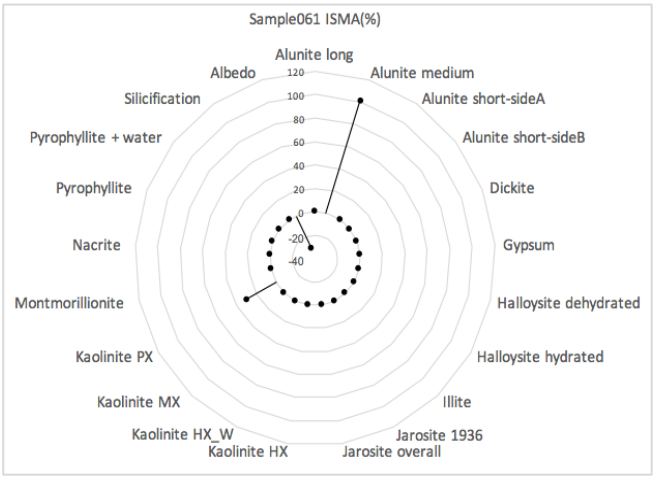
Sample061 ISMA(%)
Alunite long
Alunite medium
Alunite short-sideA
Alunite short-sideB
Dickite
Gypsum
Halloysite dehydrated
Halloysite hydrated
Illite
Jarosite 1936
Jarosite overall
Kaolinite HX
Kaolinite HX_W
Kaolinite MX
Kaolinite PX
Montmorillionite
Nacrite
Pyrophyllite
Pyrophyllite + water
Silicification
Albedo
120
100
80
60
40
20
0
-20
-40

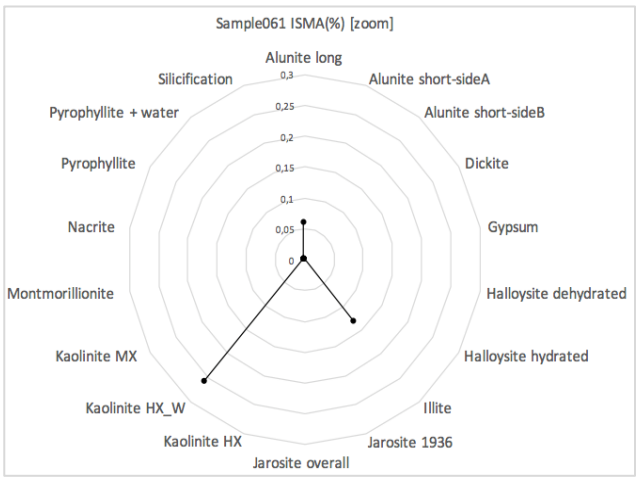
Sample061 ISMA(%) [zoom]
Alunite long
Alunite short-sideA
Alunite short-sideB
Dickite
Gypsum
Halloysite dehydrated
Halloysite hydrated
Illite
Jarosite 1936
Jarosite overall
Kaolinite HX
Kaolinite HX_W
Kaolinite MX
Montmorillionite
Nacrite
Pyrophyllite
Pyrophyllite + water
Silicification
0,3
0,25
0,2
0,15
0,1
0,05
0

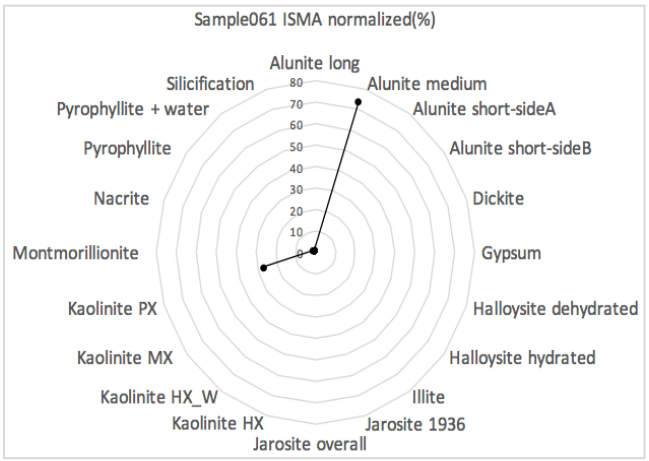
Sample061 ISMA normalized(%)
Alunite long
Alunite medium
Alunite short-sideA
Alunite short-sideB
Dickite
Gypsum
Halloysite dehydrated
Halloysite hydrated
Illite
Jarosite 1936
Jarosite overall
Kaolinite HX
Kaolinite HX_W
Kaolinite MX
Kaolinite PX
Montmorillionite
Nacrite
Pyrophyllite
Pyrophyllite + water
Silicification
80
70
60
50
40
30
20
10
0

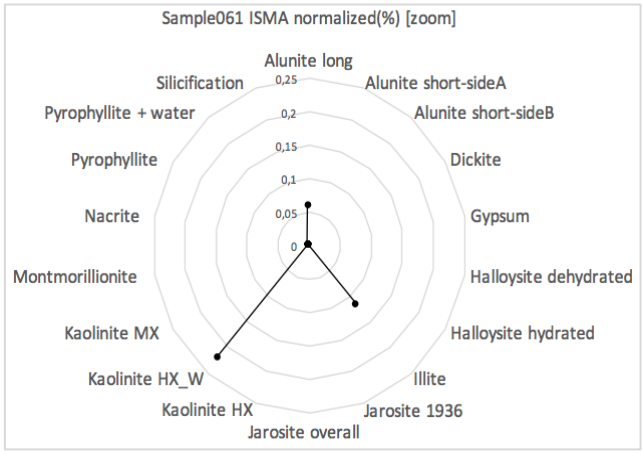
Sample061 ISMA normalized(%) [zoom]
Alunite long
Alunite short-sideA
Alunite short-sideB
Dickite
Gypsum
Halloysite dehydrated
Halloysite hydrated
Illite
Jarosite 1936
Jarosite overall
Kaolinite HX
Kaolinite HX_W
Kaolinite MX
Montmorillionite
Nacrite
Pyrophyllite
Pyrophyllite + water
Silicification
0,25
0,2
0,15
0,1
0,05
0

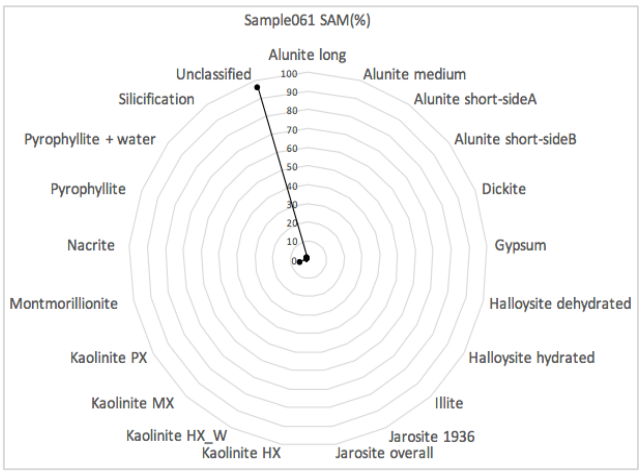
Sample061 SAM(%)
Alunite long
Alunite medium
Alunite short-sideA
Alunite short-sideB
Dickite
Gypsum
Halloysite dehydrated
Halloysite hydrated
Illite
Jarosite 1936
Jarosite overall
Kaolinite HX
Kaolinite HX_W
Kaolinite MX
Kaolinite PX
Montmorillionite
Nacrite
Pyrophyllite
Pyrophyllite + water
Silicification
Unclassified
100
90
80
70
60
50
40
30
20
10
0

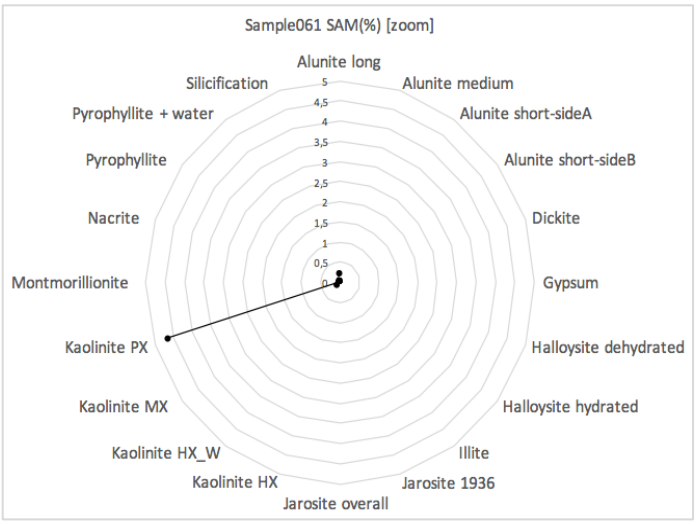
Sample061 SAM(%) [zoom]
Alunite long
Alunite medium
Alunite short-sideA
Alunite short-sideB
Dickite
Gypsum
Halloysite dehydrated
Halloysite hydrated
Illite
Jarosite 1936
Jarosite overall
Kaolinite HX
Kaolinite HX_W
Kaolinite MX
Kaolinite PX
Montmorillionite
Nacrite
Pyrophyllite
Pyrophyllite + water
Silicification
5
4,5
4
3,5
3
2,5
2
1,5
1
0,5
0

Edge with propylitic

- Sample 169

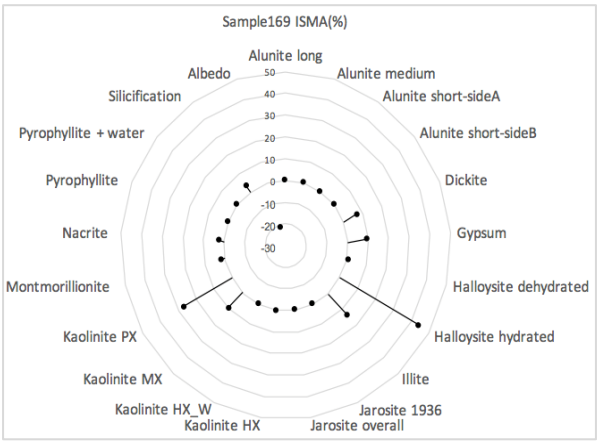

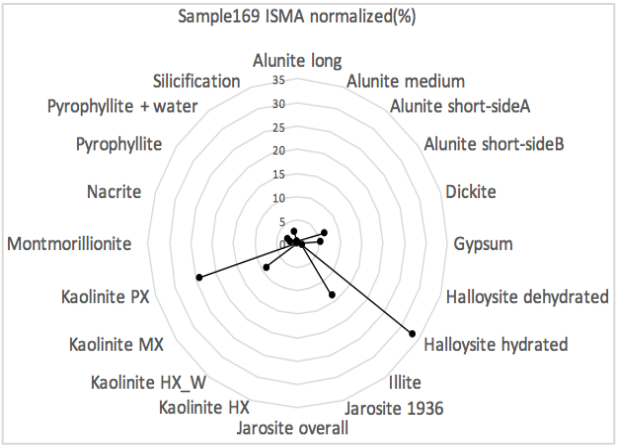

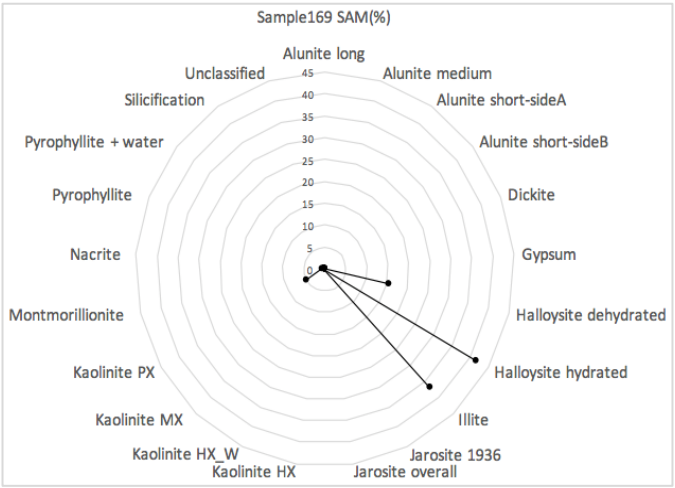

Edge with supergene

- Sample 248

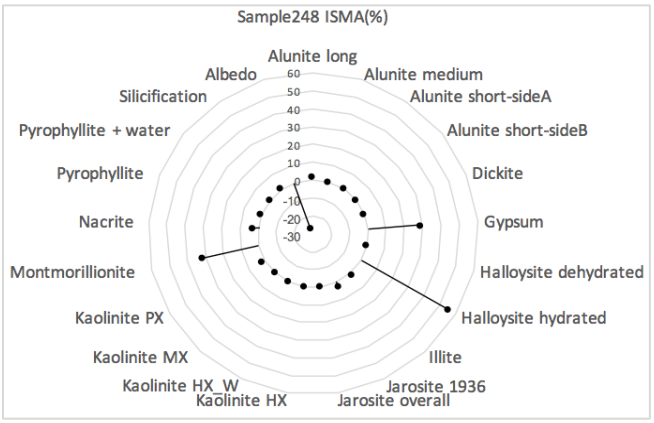

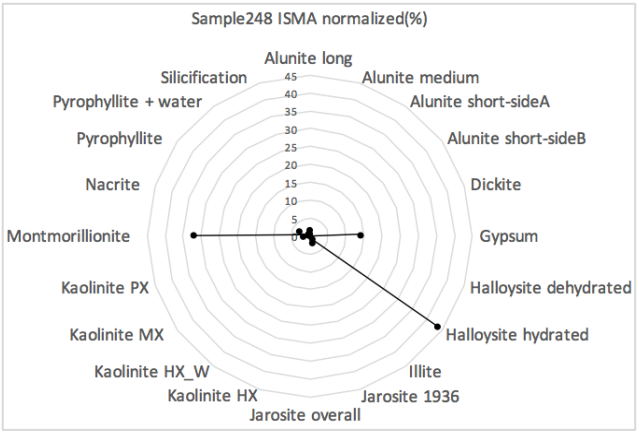

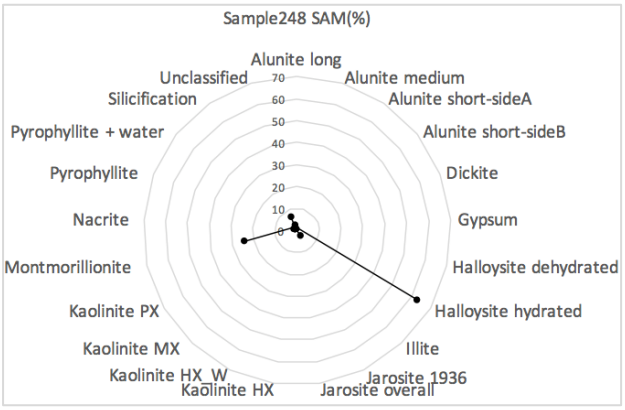

Edge with outside the map

- Sample 219

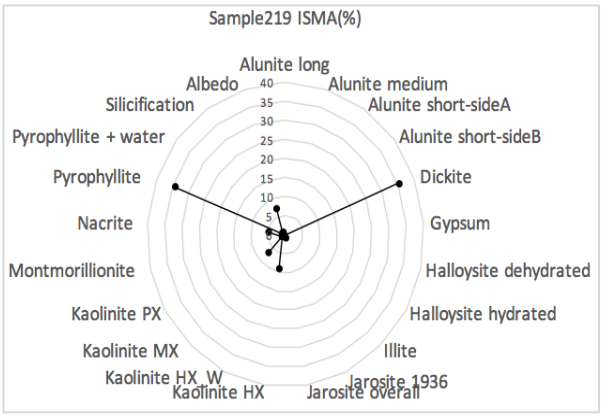

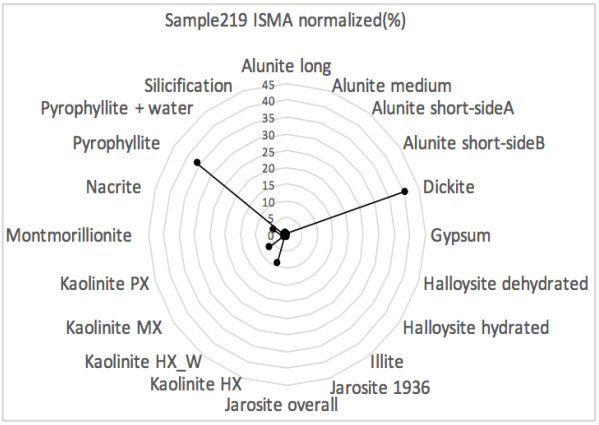

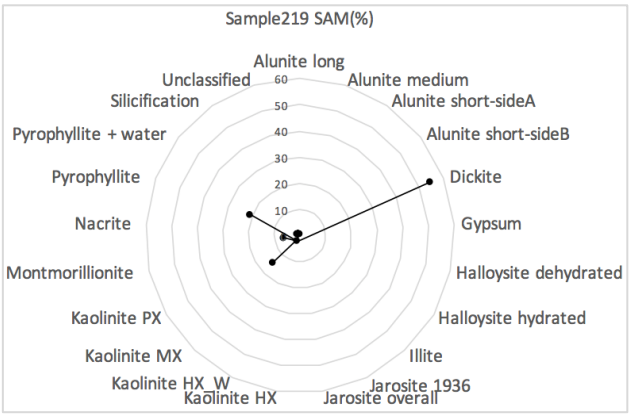

Outside the map

- Sample 008

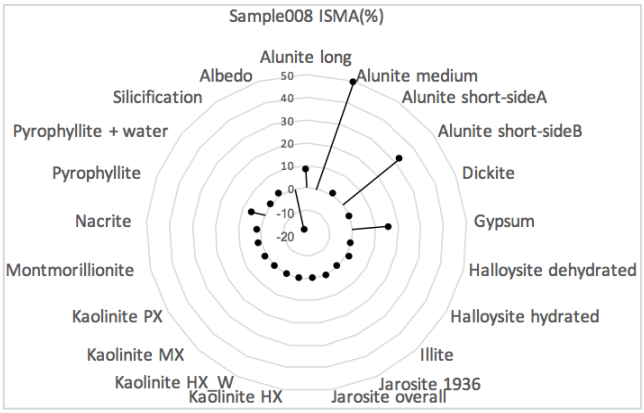

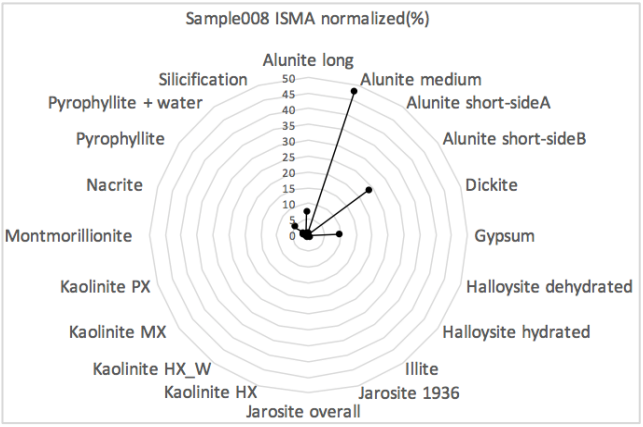

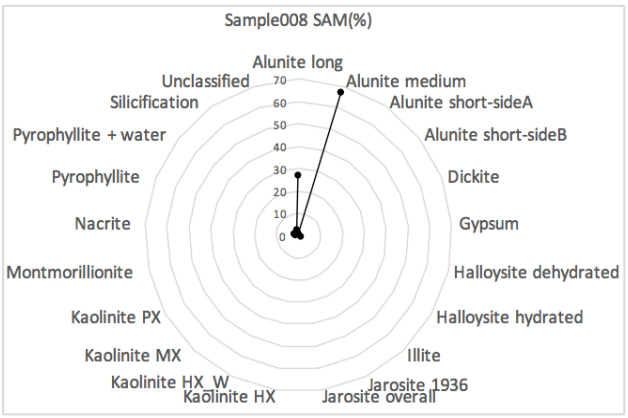

- Sample 133

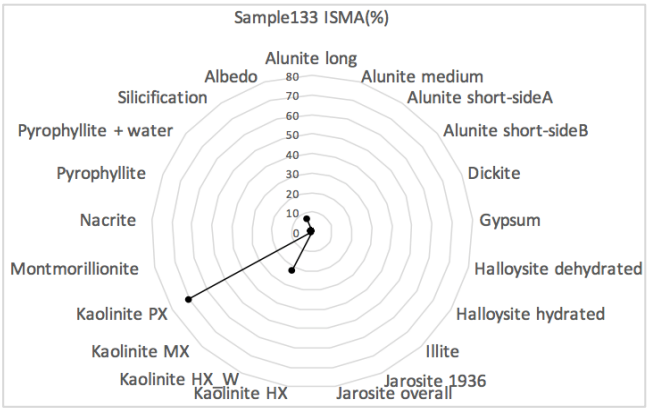
Sample133 ISMA(%)
Alunite long
Alunite medium
Alunite short-sideA
Alunite short-sideB
Dickite
Gypsum
Halloysite dehydrated
Halloysite hydrated
Illite
Jarosite 1936
Jarosite overall
Kaolinite HX
Kaolinite HX_W
Kaolinite MX
Kaolinite PX
Montmorillionite
Nacrite
Pyrophyllite
Pyrophyllite + water
Silicification
Albedo
0
10
20
30
40
50
60
70
80

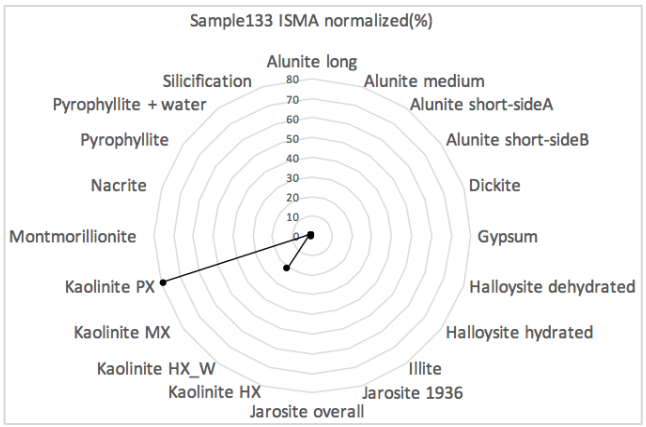
Sample133 ISMA normalized(%)
Alunite long
Alunite medium
Alunite short-sideA
Alunite short-sideB
Dickite
Gypsum
Halloysite dehydrated
Halloysite hydrated
Illite
Jarosite 1936
Jarosite overall
Kaolinite HX
Kaolinite HX_W
Kaolinite MX
Kaolinite PX
Montmorillionite
Nacrite
Pyrophyllite
Pyrophyllite + water
Silicification
0
10
20
30
40
50
60
70
80

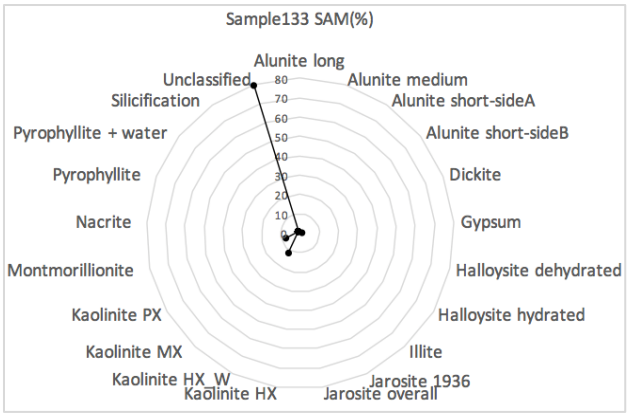
Sample133 SAM(%)
Alunite long
Alunite medium
Alunite short-sideA
Alunite short-sideB
Dickite
Gypsum
Halloysite dehydrated
Halloysite hydrated
Illite
Jarosite 1936
Jarosite overall
Kaolinite HX
Kaolinite HX_W
Kaolinite MX
Kaolinite PX
Montmorillionite
Nacrite
Pyrophyllite
Pyrophyllite + water
Silicification
Unclassified
0
10
20
30
40
50
60
70
80

Appendix 8. Methodology

Flowchart of the methodology followed to carry out the research is shown below. It starts with the non-imaging spectroscopy part were several ASD point measurements were taken to complete the existent dataset. From this dataset, the samples were selected based on spectral parameters. Then, the images were acquired with the SPECIM SWIR hyperspectral camera. The images had to be pre-processed to correct the noisy bands and data errors. With the corrected images the Wavelength Mapping algorithm was used to get a general view of the minerals that are part of the rock samples. Then a visual analysis of the spectra of the alunite minerals and kaolinite minerals found was done to evaluate spectral differences amongst alunite minerals and crystallinity variations of kaolinite minerals. The endmembers were handpicked from the wavelengths maps. With this endmember collection, the SAM was run to classify the images based on the most dominant minerals per pixel; and then the ISMA was also run to unmix the spectra and get the partial fraction abundances of the minerals per pixel. Results of the SAM and ISMA were quantified and represented in spider graphs and a bar graph. Finally, for validation purposes two geochemical analysis were done: ICP-OES and TGA.